

# $J/\psi$ PRODUCTION IN PROTON-PROTON COLLISIONS AT ALICE

**Ravjeet Kour**

*Thesis submitted for the degree of*

*Doctor of Philosophy*



Particle Physics Group,  
School of Physics and Astronomy,  
The University of Birmingham.

May, 2011.

# Abstract

A Large Ion Collider Experiment (ALICE) studies the strong interaction part (Quantum Chromo Dynamics) of the Standard Model at the CERN Large Hadron Collider. ALICE has been designed as a general-purpose heavy-ion detector in order to explore phenomena of strong interacting matter and the quark-gluon plasma (QGP) at extreme values of energy density and temperature in nucleus-nucleus collisions.

Results are presented here on the study of  $J/\psi$  production in pp collisions at ALICE. In particular, a measurement of  $J/\psi$  cross-section at  $\sqrt{s} = 7$  TeV energy has been performed, together with a study of a possible algorithm to separate primary  $J/\psi$  from those coming from decays of  $B$  hadrons. The validity of this algorithm in ALICE has been demonstrated using Monte-Carlo samples. The  $J/\psi$  particles have been searched exclusively in the decay channel  $J/\psi \rightarrow e^+e^-$ . The study focused on what would be achievable in a period of early running, with integrated luminosity of  $L = 1.25 \text{ nb}^{-1}$ , at a proton-proton centre of mass collision energy of  $\sqrt{s} = 7$  TeV.

# Author's contribution

All the work presented in this thesis, related to the analysis of  $J/\psi$  production in pp collisions at  $\sqrt{s} = 7$  TeV, performed on real and simulated data, is my own. The software designed in order to carry out the study was written by myself; I have developed the analysis and optimised the signal selection and background rejection; and I have performed the cross section measurement and the study of the primary versus secondary  $J/\psi$  separation.

However, the analysis makes use of the ALICE analysis software framework (AliRoot), available to all within the collaboration. In addition, the majority of the simulated data sample was produced centrally during the so-called Data Challenge production 2010 ; and the real data were taken by the ALICE collaboration during 2010 and are distributed over the LHC computing grid.

Ravjeet Kour

# Acknowledgements

I would like to take this opportunity to acknowledge all my friends, colleagues and family who have supported and encouraged me during the time of my PhD. I truly have been looking for this moment to come, so that I can give thanks to so many people with whom I have been through all this time.

**Birmingham ALICE group:** My acknowledgement begins by giving a big thanks to my supervisors Dr. Cristina Lazzeroni and Dr. Roman Lietava for all the help and support they have given me throughout my PhD. I would not have been at this point without them. Both of them were extremely benevolent with their time throughout the course of my PhD. I would like to thank Cristina for always giving me valuable advice be it in professional or personal matters. I think she has the solution for every problem. I also would like to thank Roman from my heart who has helped me many times to carry out the research and make this a complete thesis.

I would like to thank the other people in the group in Birmingham: Dr. David Evans, Dr Orlando Villalobos Baillie, Dr. Gron Jones, Dr. Peter Jones, Dr. Lee Barnby, Dr. Pedja Jovanovic (hope he is enjoying his retirement life), Mr. Anton Jusko, Dr. Marian Krivda, Prof. John Kinson, and Dr. Frank Votruba. Thanks Lee for helping me on the Grid problems. I would like to thank all the present and post ALICE students in particular J.D. Tapia Takaki, Sparsh Navin, Zoe Matthews, Arvinder Palaha, Plamen Petrov and Patrick Scott.

Special thanks to Orlando and David for proof reading my thesis and making it finish on time.

**Birmingham Particle Physics group:** I would like to pay my thanks to Prof.

Peter Watkins and Prof. Paul Newman for offering me a place in the Birmingham group. Prof. Paul Newman helped me in applying for the scholarship, I think without his advice it would have been difficult to receive the scholarship. A very special thanks to Ms. Norma Simpson for being so kind and patient in dealing with me in the admission process. Thanks for giving me the letters I needed for my visa purposes. I really wish her good luck for her retirement life. I should not forget Dr. Lawrie Lowe, for being so helpful in giving the computing support throughout my PhD. Also last not but not least I should thank Prof. Raymund Jones who gave me the teaching duties for the last three years. It was really helpful as my scholarship was over by October 2010. Thanks for the teaching experience in this University.

I would like to thank the UK Overseas Research Student Award Scheme (OR-SAS), the University of Birmingham who completely funded my PhD studies.

**ALICE collaboration and colleagues:** I feel good in myself that I have worked for ALICE collaboration within the CERN's Large Hadron Collider project. I would like to give a big thanks to Dr. Giuseppe Bruno who at first point, directed me towards the analysis which I have presented in this thesis. Thanks Giuseppe for inviting me to Italy in his university to undertake my analysis. Also big thanks for the lovely dinner which I had at your place. Special thanks to your wife who prepared the delicious dinner. It was a great experience. Also thanks to Carmelo Digiglio for discussing the  $J/\psi$  analysis. I would also like to thank Dr. Renu Bala for helping me to understand some features of Alien. Thanks to Dr. Marek Bombara for proof reading my mid-term report. Thanks for solving some of the software issues.

Also a person who truly deserves a very special thank giving is Prof. Anju Bhasin. She inspired me to pursue my PhD after my Masters. She has always been so kind for so many years. She is not just my teacher but also a good friend who has always given me true advice in my personal and career front matters. She really helped me during admission and scholarship application. Thanks to her for proof

reading my thesis.

**People I cannot forget to thank:** There are so many people I feel I have to thank them for this journey. Coming from India and adjusting into this life in UK was a tough thing, but with all my friends around this was a made easy.

I would like to thank Miss Vinothini Sangaralingam for being a very good friend of mine all the time. Although I have not learnt south Indian food from her, but have definitely enjoyed so many times the same. Thanks Vino for taking my teaching in the need of emergency. Also thanks to Sathish for bringing the medicine so late in the night when I had a fever. Thanks to Dr. Smriti Mahajan for being warm and friendly and pouring good advice all the time.

I would like to thank my office mates: Sparsh Navin, Zoe Matthews, Arvinder Palaha, Plamen Petrov and Patrick Scott. I wish I could have gone on LTA to spend more time with you all. A big thanks to Arvinder and his parents for letting me stay at their place. It really means a lot to me. Thanks Zoe for the sweet marriage present. I should thank Angela Romano who substituted me a couple of times in my teaching duties. Thanks for the lovely greeting that you gave to me.

I would like to thank my house mates: Dr. Yuvraj and Rashmi for the nice company. Thanks Yuvraj for the nice cup of tea that you always make for us. I cannot forget the shoe scandal for my entire life. Thanks Reshmi for good food that I had so many times.

Thanks to all my colleagues from teaching with whom I have worked for the last three years.

Thanks to all my friends in Bharat Parivaar, I thoroughly enjoyed all the events I have participated in. It never gave me a feeling that I was out of India for such a

long time.

**Special thanksgiving to the people that really matter in my life:** On a very personal basis, I would like to thank my family who have been a big support during my PhD. A big thanks to my father who always had a big faith in me. Thanks Dad. I cannot forget to give thanks to my eldest brother Mr. Manjeet Singh and his wife Mrs. Kirndeeep Kaur who have supported me in every aspect during my stay in UK. Thanks to my other two brothers and their wives Mr. Bhopinder Singh, Mr Loveleen Singh, Mrs Kamalpreet Kaur, Mrs Arminder Kaur for all the love and moral support that they have provided me. Thanks to my younger sister Miss Ravdeep for the moral support. I would like to thank my two sister-in-laws Dr. Gurpreet Kaur and Dr. Amandeep Kaur and brother-in-law Dr. Surinderjeet Singh for the moral support.

Special thanks to my husband Dr. Parminder Singh Sandhu for supporting and encouraging me all the time. Thanks for proof reading although not being from a physics background.

Last but not least, thanks to my parents Mr. Kirpal Singh, Mrs. Savtanter Kaur and to my father-in-law Mr. Puran Singh Sandhu. This thesis is being dedicated to you three.

Ravjeet Kour

# Chapter 1

## Introduction

It is believed that our universe originated in a Big Bang from a state of almost infinite energy density and temperature. During the first few microseconds of its life the energy density in our universe was so high that hadrons (colour singlet bound states of quarks, antiquarks and gluons), such as the nucleons inside a nucleus, could not form. Instead, quarks, antiquarks and gluons were deconfined and permeated the entire universe in a thermalized state known as a Quark-Gluon Plasma (QGP). Only when the energy density of the universe dropped below the critical value, about  $1 \text{ GeV}/\text{fm}^3$ , equivalent to temperature  $170 \text{ MeV}$ , did the colour degree of freedom become confined into colour singlet objects of approximately  $1 \text{ fm}$  diameter: the first hadrons formed.

Understanding the properties of elementary particles at high temperature and density is one of the major goals of particle physics. Through a study of the properties of elementary particles, formed from such extreme conditions, we hope to learn about the equation of state that controlled the evolution of the early universe and perhaps the structure of compact stars. The ALICE (A Large Ion Collider Exper-

iment) [1] experiment is devoted to the study of hot and dense matter created in ultra relativistic heavy ion collisions.

## 1.1 Quantum Chromodynamics

### 1.1.1 Introduction

Quantum Chromodynamics [2] QCD is the theory of the strong force, one of the four forces of nature. It describes the interactions of quarks, via their colour quantum numbers. QCD calculations indicate that the potential between two heavy quarks is of the form shown in equation 1.1 ( more details in chapter 2)

$$V(r) = \frac{-\alpha(r)}{r} + \sigma r. \tag{1.1}$$

where  $r$  is the distance between the quarks,  $\alpha$  is the coupling constant of coulomb like term and  $\sigma$  is the string constant.

For small  $r$ , the first term dominates and the system behaves similarly to the electrodynamic case. At larger  $r$ , the potential energy of two quarks increases with separation until enough energy is present to form a new quark-antiquark pair, which occurs if the quarks are separated. As a result, quarks are never observed individually but always as part of a 3 quark state (baryon) or a quark-antiquark state (meson). This property is known as confinement.

As  $r$  becomes small, however, this behaviour deviates from the simple models for QED and QCD. In quantum field theory, an electron can emit a virtual photon which can become a electron-positron pair. Therefore, an electron will spontaneously become surrounded by a cloud of virtual  $e^+e^-$  pairs. The charge on the original electron will polarise this cloud, attracting the positrons. A probe far away will see the actual charge, whereas a close probe sees a larger charge due to the effect of the cloud. A similar, but opposite, effect occurs in the strong interaction. A probe close to the colour charge will see a lower colour charge than a probe far away. In the limit of zero separation, the charge appears to be zero. This is known as asymptotic freedom.

### 1.1.2 Asymptotic freedom and confinement

The theory of asymptotic freedom states that the interaction between quarks reduces as the distance between them reduces, and tends to zero as the distance between them reduces to zero. Conversely, the interaction between them increases as they are separated by larger distances.

Colour confinement is the physics phenomenon that colour charged particles (such as quarks) cannot be isolated, and therefore cannot be directly observed. Quarks, by default, clump together to form two types of hadrons ( the mesons and the baryons, composed of quark and antiquark and three quarks respectively). The constituent quarks in a group cannot be separated from their parent hadron, and this is why quarks can never be studied or observed in any more direct way than at a hadron level.

The reasons for quark confinement are somewhat complicated; there is no analytic proof that quantum chromodynamics should be confining, but intuitively confinement is due to the force-carrying gluons having colour charge. One can compare the electromagnetic interaction with the strong interaction. As any two electrically-charged particles separate, the electric fields between them diminish quickly, allowing (for example) electrons to become unbound from nuclei. However, as two quarks separate, the gluon fields form narrow tubes (or strings) of colour charge, which tend to bring the quarks together as though they were some kind of rubber band. This is quite different in behaviour from electrical charges. Because of this behaviour, the colour force experienced by the quarks in the direction that holds them together, remains constant, regardless of their distance from each other.

## **1.2 Heavy Ion collisions**

If a nucleus is compressed enough, it would experience a change of state. The standard combination of quarks inside particles would break down as a completely different state and matter - a plasma of free quarks and gluons would be created, which is known as a Quark Gluon Plasma.

### **1.2.1 Quark Gluon Plasma**

Nuclear matter at normal energy densities is composed of protons and neutrons. If the energy density is increased the protons, nucleons, and other particles overlap

and get squeezed so tightly that their constituents (quarks and gluons) are free to roam the system without being confined inside hadrons. At this density, there is deconfinement and the system becomes a quark-gluon plasma. Thus, relativistic heavy ion collisions provide a possible way for creating QGP in the laboratory. The QGP existed during the time of Big-Bang and is formed at energy densities of the order  $1 \text{ GeV}/\text{fm}^3$ . It has also been suggested that matter at such a density may exist inside the cores of neutron stars [3].

## 1.2.2 Space Time Evolution in Relativistic Heavy Ion Collisions

The space - time evolution of a head on Collision at high energy is shown in figure 1.1. In the first moments of a reaction, hard scattering processes on the parton level may occur. These rates can be studied using structure functions and perturbative QCD cross-sections.

After a short time, usually taken to be  $\sim 1 \text{ fm}/c$ , partons materialise out of the highly excited QCD field. Thermal equilibrium may now be approached via individual parton-parton or string-string interactions. A calculation of the mean free path of quarks in QCD matter gives a value of  $\lambda = 0.5 \text{ fm}$  at an energy density  $E = 2 \text{ GeV}/\text{fm}^3$  [4], indicating that equilibrium may indeed be reached in collisions of heavy nuclei where the transverse radii, and hence initial dimensions, are clearly larger than  $\lambda$ .

As the system expands, mainly along the longitudinal direction as it is co-related

to the original ion motion, its energy density and temperature decreases until it reaches a critical temperature  $T_c$  after 30 fm/c. Potentially, the matter now spends a relative long time in the mixed phase. It has to rearrange the many degrees of freedom (partons) of QGP into the smaller number available in the hadronic phase, with a large associated release of latent heat. In the last and hadronic phase, the interacting systems keep expanding. It may expand, until freeze out, when interactions cease and the particles stream away to be detected by the experimental apparatus.

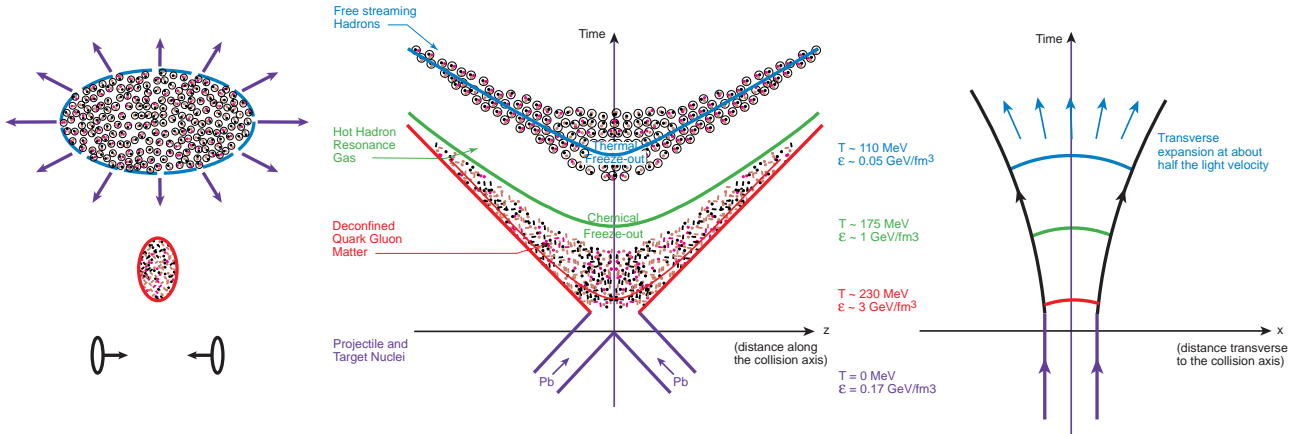


Figure 1.1: Space time evolution of a heavy-ion collision describing the chemical freeze out (where the interactions changing particle species are stopped) and thermal freeze out (where the mean free path is comparable to the size of the system).

## 1.3 Signals of Quark Gluon Plasma

In order to assess whether or not deconfined matter has been created, suitable signatures are looked for. Some of the QGP signatures are strange particle production, charmonium suppression, jet quenching, elliptic flow, electromagnetic signals like direct photon and dilepton production [5].

Strangeness enhancement was one of the main pieces of evidence for CERN's claim to have produced deconfined matter in 2000 [6] [7]. If a QGP phase was formed in nucleus-nucleus collisions, the yield of strange particles produced, such as those that contain one or more strange quarks or antiquarks, is expected to increase compared to a non-QGP scenario. In other words, the density of strange quark pairs is predicted to be unusually high compared to that for a hadron gas phase [8].

It was also predicted that the  $J/\Psi$  meson should be suppressed if a QGP state was formed at SPS energies [9] [10]. Because the mass of the charm quark is ten times greater than that of the strange quark, at SPS energies, charm (and bottom) quarks can be seen as particles exclusively produced during the early stages of the collision through high energy hard interactions. The high abundances of quark-antiquark pairs and gluons produced in the de-confined state would screen the heavy quarks by surrounding  $q\bar{q}$  pairs, which leads to the break up of  $J/\psi$  in quark medium. At Large Hadron Collider energies, in particular in Pb-Pb collisions,  $c\bar{c}$  and  $b\bar{b}$  will be produced abundantly. Quarkonia [5] will probe the medium created in a collision. The production of quarkonia is described well by pQCD ( more details in next chapter). Due to Debye screening the produced state is split up depending upon the temperature of the surrounding medium. More details of why  $J/\psi$  is used as a

probe will be given in chapter 2.

The RHIC experiments [11] have confirmed that information about the QGP can be revealed by studying the regime of high transverse momentum particles [12, 13, 14, 15]. Jets of hadrons are formed from the initial hard scattered partons, which are thought to be modified when they traverse the medium in the QGP phase [16].

Another tool to study the QGP is to examine electromagnetically interacting probes which have already decoupled from the hot coloured phase of the matter. Direct photon and lepton pairs are such observables. They emerge as thermal radiation from the heated matter without being altered by the final states so bringing information about the temperature of the system.

# Chapter 2

## J/ $\Psi$ measurement in heavy ion collisions

### 2.1 Introduction

Strongly interacting matter, at sufficiently high density, is predicted to undergo a transition to a state of deconfined quarks and gluons. In such a state colour screening shields a given quark from the binding potential of any other quarks or antiquarks. Bound states of very heavy quarks, such as J/ $\Psi$  or  $\Upsilon$ , have radii which are smaller than those of the usual mesons and nucleons: hence they can survive in the deconfined medium until the temperature or density become so high that screening dissolves their tighter binding (see figure 2.1) J/ $\psi$  suppression appears as a signal for Quark Gluon Plasma formation.

The  $J/\psi$  system is a meson resonance which consists of a  $c$  and  $\bar{c}$  quark. It has a mass of about 3.097 GeV (in natural units with  $c=1$ ). The PDG value corresponds to  $3096.916 \pm 0.011$  MeV [98]

This chapter is divided into two sections. The first half describes the mechanism of  $J/\psi$  production and the effect of coloured medium on  $J/\psi$  production. Second half gives the summary of results on  $J/\psi$  production from previous experiments.

### 2.1.1 Discovery of the $J/\psi$

In November 1974 a narrow resonance at 3.1 GeV/ $c^2$  in the  $e^+e^-$  invariant mass spectrum was observed [17] at the Brookhaven alternating gradient synchrotron (AGS) in collisions of 28 GeV/ $c$  protons on a Beryllium target and in electron-positron collisions at Stanford Linear Accelerator Centre (SLAC), using the  $e^+e^-$  collider Stanford Positron Electron Accelerating Ring (SPEAR) [18]. The particle was named  $J/\psi$ . At that time the known quarks were up, down and strange quarks. In addition a fourth quark was predicted by the Glashow-Iliopoulos-Maiani (GIM) [19] mechanism. Soon after the discovery it was evident that the newly discovered particle consisted of the predicted quark species, the charm quark. Thus this discovery added a new particle to the fundamental building blocks of nature. Another sharp resonance peak in the dimuon<sup>1</sup> spectrum was later discovered in 400 GeV proton-nucleus collisions in 1977 at Fermilab. [20], the  $\Upsilon$ . The  $\Upsilon$  is the bound state of  $b\bar{b}$  quarks. The heaviest of all the quarks, the top quark, was discovered in 1995

---

<sup>1</sup>The dimuon spectrum denotes the invariant mass spectrum of muon anti-muon pairs. In general a combination of two leptons is called dilepton.

[21]. This discovery formed the quark family. Up(u), down(d) and strange(s) quarks are called the light quarks, while the charm(c), bottom(b) and top(t) are referred to as heavy quarks. Bound states of these heavy quarks with their corresponding anti-particles are called quarkonia. The top quark cannot form a bound state because of its short lifetime of less than  $10^{-24}$ s.

Given the mass of the charm quark of  $1.3 \text{ GeV}/c^2$  and the QCD coupling constant  $\alpha_{QCD} = 0.3$ , the system can be studied in a non-relativistic approach starting from the Schrödinger equation for the charm anti-charm system

$$(2m_c - \frac{1}{m_c} \nabla^2 + V(r))\Phi_i(r) = M_i\Phi_i(r) \quad (2.1)$$

where  $\Phi_i$  and  $M_i$  is the system wave-function and mass respectively with a binding potential

$$V(r) = \sigma r - \frac{\alpha}{r} \quad (2.2)$$

where  $m_c$  is the charm mass,  $r$  is the distance between the quarks,  $\alpha$  is the coupling constant of coulomb like term  $\alpha/r$ ,  $\alpha \simeq \alpha_{QCD}$  and  $\sigma$  is the string constant estimated as  $0.16 \text{ GeV}^2$ .

This so-called Cornell potential was proposed in papers [22][23]. It consists of a linear term accounting for the specific feature of QCD that the potential energy increases with increasing distance. The charmonium spectrum is well described by the Schrödinger equation (2.1). One can use the uncertainty principle that the product of uncertainty in the position and momentum is approximately equal to 1 i.e.  $r.p \simeq 1$  to estimate the energy of the bound state:

$$E(r) \simeq 2m_c + \frac{1}{m_c r^2} + \sigma r - \frac{\alpha_{QCD}}{r} \quad (2.3)$$

Minimising  $E(r)$  with respect to  $r$  gives the radius of the ground state:

$$\frac{dE(r_0)}{dr} = 0 = -\frac{2}{mr_0^3} + \sigma + \frac{\alpha}{r_0^2} \quad (2.4)$$

With  $\alpha_{QCD}$  (coupling constant of coulomb like term) = 0.3 and  $\sigma$  (string constant) = 0.16 GeV<sup>2</sup> and the charm mass  $m_c = 1.3$  GeV/ $c^2$ , one can obtain the radius of the ground state  $r_0 = 0.36$  fm. With this radius the mass of the ground state is calculated as  $M_0 = E(r_0) = 2.95$  GeV/ $c^2$ , close to the measured mass of 3.096 GeV/ $c^2$ . Table 2.1 shows the radius, mass, binding energy ( $\Delta E = 2m_c - M_0$ ) and difference in the theoretical and the measured mass ( $\Delta M$ ) for the  $J/\psi$ . The theoretical values are obtained by solving the exact Schrödinger equation (2.1) [4] though having a agreement with the uncertainty principle.

Table 2.1: Radius, mass, binding energy and  $\Delta M$  of  $J/\psi$  [4].

|                          |          |
|--------------------------|----------|
| state                    | $J/\psi$ |
| mass [GeV/ $c^2$ ]       | 3.10     |
| $\Delta E$ [GeV]         | 0.64     |
| radius [fm]              | 0.25     |
| $\Delta M$ [GeV/ $c^2$ ] | 0.02     |

### 2.1.2 Why charmonium as a probe

There have been significant developments in the study of quarkonium production, both in theory and experiment, and these developments have important implications for the use of charmonium as a probe in heavy ion collisions. The charmonium states are produced in abundance in heavy-ion collisions. The heavy nature of charmonium ( $c\bar{c}$ ) allows one to apply potential models in non-relativistic quantum mechanics to

calculate the meson binding radius. It was predicted that the modification of the heavy quark pair potential in the hot dense matter created in heavy ion collisions would cause the pair to become uncorrelated due to colour charge screening. This modification of the pair potential via Debye screening leads to charmonium suppression [24] when compared to a binary collision.<sup>2</sup>

Due to the different binding energies for the different charmonium states, as seen in figure 2.1, it is possible to gain access to the temperature of the medium. Charmonium suppression in hot and dense matter has been considered to be a signature for the production of the quark gluon plasma (QGP).

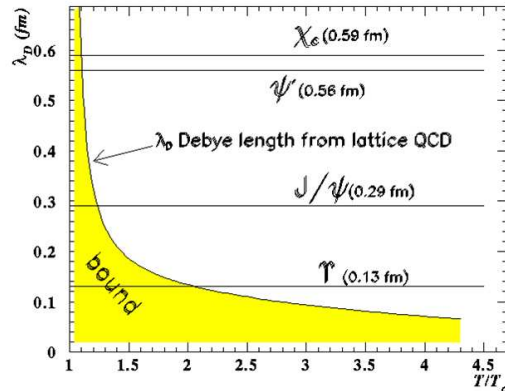


Figure 2.1: Different charmonium states corresponding to different temperature.

Some of the non-QGP factors leading to the suppression include shadowing of the partons in a nuclear environment, breakup of a correlated  $c\bar{c}$  as it traverses the nuclear fragment, suppression of feed-down from higher mass state as well as

---

<sup>2</sup>A binary collision is a collision between two nucleons. The nucleons in a heavy ion collision can (and often do) collide more than once during the course of the nucleus-nucleus collision, hence for a given process typical collision numbers are higher than the corresponding numbers of participating nucleons

other initial state interactions. In order to disentangle these effects it is important to measure the charmonium production rates in both proton+proton and proton nucleus collisions. The p-p collisions serve as a baseline for searching for suppression compared to the binary scaling predictions, predicts the amount of feed-down from higher states and serve as a tool to distinguish between different theoretical calculations for charmonium production mechanisms. In order to quantify nuclear effects it is also necessary to study charmonium production in proton-nucleus collisions where the temperature and density of the system are low compared to the heavy ion collision.

### 2.1.3 $J/\psi$ production

The charmonium production in proton-proton can be divided into two parts:

- Production of a heavy quark pair in hard collisions
- Formation of quarkonia out of the two heavy quarks

Due to the high mass of the heavy quarks ( $m_{charm} \simeq 1.3 \text{ GeV}/c^2$ ,  $m_{bottom} \simeq 4.7 \text{ GeV}/c^2$ ) the first process can happen only during the first phase of a collision. Only at that time can the elementary collisions with sufficiently high momentum transfers to create such high masses take place. For this reason the heavy quark production is called a hard process that can be treated perturbatively. In next-to-leading order (NLO) calculations the available experimental data at different energies and collision systems [25][26] are used to obtain parameters to predict the total cross-section in

proton-proton collisions at the LHC energies. The charm production cross-section is predicted to be 6.3 mb and that of bottom is 0.19 mb [27].

The second part, namely the formation of quarkonia out of the quark-antiquark pair, a priori cannot be treated perturbatively. Due to the high quark masses and small relative velocities in the quarkonia system, the formation can be described using non-relativistic QCD (NRQCD). This allows the factorisation into a perturbative small range, high momentum part and a long range, low momentum part. In the past, three models were developed, namely the Colour Singlet Model (CSM) [28][29], the colour Octet Model (COM) [30][31][32] and the Colour Evaporation Model (CEM) [33][34][35].

A quarkonium state has to be formed from two quarks that are colour neutral but, in principle, the two heavy quarks are not necessarily carriers of one colour and the corresponding anti-colour, so the combination might be coloured. The colour singlet model rejects all colour octet states; in the NRQCD factorisation the produced quarkonium state has the same quantum numbers as the quark-antiquark pair. Predictions by the CSM for the production of the quarkonia at the Tevatron underestimated the data by an order of magnitude. Thus it was clear that the colour octet state cannot be neglected. Figure 2.2 shows  $J/\psi$  production mechanism as described in the colour singlet model [36].

Figure 2.3 shows the cross-section for production of prompt charmonium in  $p\bar{p}$  collisions. Prompt means that the charmonium is produced by the QCD interaction rather than by weak decays of hadrons containing bottom quarks. The cross-section for prompt  $\psi$  production at the Tevatron has been measured by the CDF collabora-

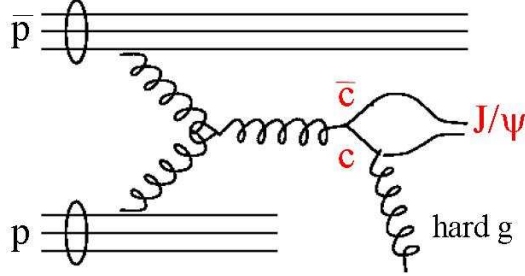


Figure 2.2:  $J/\psi$  production as predicted by the colour singlet model in  $p\bar{p}$ .

tion for the transverse momenta in range  $5 < p_T < 20$  GeV/c [37]. The background from decays of bottom hadrons and radiative decays were subtracted. In figure 2.3, the dashed curve shows the leading-order predictions of the colour singlet model, and the dotted line the predictions from fragmentation in the colour singlet model. The measured cross-section was found to be about a factor of 30 larger than predicted by the colour-singlet model and hence there is the need to take into account the colour octet model.

The colour octet model considers the octet state as well and within the model quarkonia is produced in an octet <sup>3</sup> and thus coloured state. The pre-resonant coloured state neutralises its colour by the emission of soft gluons [36] as seen in figure 2.4. Though the colour octet model was able to reproduce the production cross-section, it failed to describe the large transverse  $J/\psi$  polarisation [38] at intermediate to large  $p_T$  [39].

---

<sup>3</sup>The symmetry group of QCD is  $SU(3)$ . In this group there are three colour triplet R, G, and B and their corresponding descriptors  $\bar{R}$ ,  $\bar{G}$  and  $\bar{B}$ . Out of these one can form  $3 \oplus 3 = 8 \oplus 1$  combinations, which contain both the octet and the singlet state

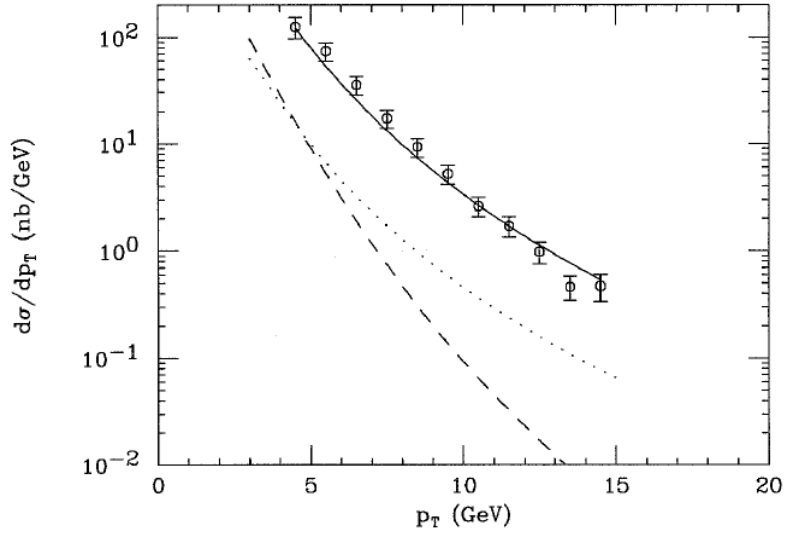


Figure 2.3: CDF data on differential cross-section for prompt  $\psi$ . The dashed curve shows the leading-order predictions of the colour singlet model, and the dotted line the predictions from fragmentation in the colour singlet model, while the solid line is the prediction of the colour-octet mechanism, with the normalisation adjusted to fit the data [37].

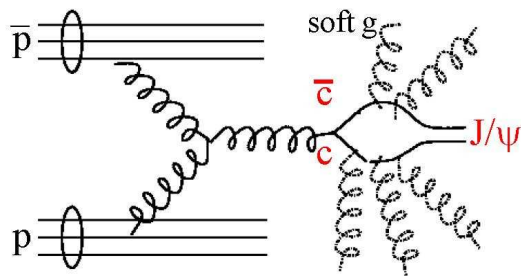


Figure 2.4:  $J/\psi$  production as predicted by the colour octet model in  $p\bar{p}$ .

Due to the limitation of the COM, another model, the Color Evaporation Model was developed. It included the evaporation of surplus colour via different processes not by the the emission of a soft gluon. The large number of processes results in a relatively large number of parameters, that have to be determined by comparison to existing data. This large number of the parameters limits the predictive power of the CEM. Nevertheless it is the best available approach to describe the available measurements and it is used to predict the cross-section at the LHC energies.

In this approach the parameter sets matching the CDF data are taken to extrapolate the cross-sections to a LHC energy of 14 TeV (pp) and 5.5 TeV/A (pp). The resulting cross-sections are given in Table 2.2. The production cross-sections include two effects:

- The expected feed down. Feed-down denotes the effect that the observed cross-section of  $J/\psi$  is the composite of directly produced  $J/\psi$  and  $J/\psi$  originating from the decay of heavier particles.
- Branching ratio into dielectrons.

Table 2.2: Prediction for  $J/\psi$  cross-sections at the LHC by the CEM. The cross-section includes the branching ratio into electrons as well as feed down from higher states. All the numbers are given in  $\mu b$  [40].

| system        | $\sqrt{s}$ (TeV) | $\sigma (J/\psi) \mu b$ |
|---------------|------------------|-------------------------|
| proton-proton | 14 TeV           | 3.18                    |
| proton-proton | 5.5 TeV          | 1.83                    |

#### 2.1.4 Behaviour of $J/\psi$ in the hot matter

T. Matsui and H. Satz were the first to suggest that heavy quarkonia could be used as a probe for the matter created in a heavy ion collision [9]. There are different scenarios for the matter created. The first scenario revolves around the assumption that the energy density is not sufficient to dissolve the hadrons contained in the colliding nuclei. This is what is known as a hadron gas. The second scenario is that of Quark-Gluon-Plasma, where the energy density is large enough for the hadrons to be melted and results in a state of free quarks and gluons. The basic aim is to find a probe which is sensitive to the surrounding material. Quarkonium production measurement is one of the ideal probes for the following reasons:

- Due to the high masses heavy quarks are produced in the first stages of the collision, such that the initial production is not affected by the produced medium.
- Due to the high decay probability into leptons, which have the property of not interacting with the medium, they remain unchanged by the medium they traverse
- Also they are highly sensitive on whether the surrounding medium consists of deconfined matter or not, which is described below.

Since a hadron gas consists of hadrons and is thus colour neutral one would expect quarkonia to be produced in a comparable way as observed in proton-proton or proton-nucleus collisions. The dominant interaction between produced quarkonia and the medium would be scattering off nucleons and pions. These scattering processes can lead to the dissociation of the quarkonium state. Since the cross-sections

of these processes are hardly known and also the theoretical predictions range from 0.1 to 8 mb, the effect of these processes has to be evaluated by comparison with collisions of smaller systems and extrapolated to heavy-ion collisions. All these effects are usually called Cold Nuclear Matter effects.

By taking into account, where the Quark-Gluon-Plasma is formed, that the hadron melts and that a state of free quarks and gluons is formed, these particles can move freely within a volume of few  $fm^3$ . As this medium is not colour neutral, it behaves as a colour conductor. Analogously to the screening of Coulomb potential where the effect is called Debye screening (screening of the charges), the Cornell potential (eq. 2.2) is modified to

$$V(r) = \sigma \lambda_D (1 - e^{-\frac{r}{\lambda_D}}) - \frac{\alpha}{r} e^{-\frac{r}{\lambda_D}} \quad (2.5)$$

where  $\lambda_D$  is the Debye screening radius and it depends upon the temperature of the produced medium.

## 2.2 Results from Previous Experiments

The expected yields per central collision <sup>4</sup> of  $c\bar{c}$  and  $b\bar{b}$  at SPS, RHIC and LHC are given in table 2.3. This yields are proportional to the amount of produced quarkonia. The aim is to measure a suppression that can be interpreted as a result of quarkonium dissociation in the deconfined medium. Most of the measurements

---

<sup>4</sup>The distance between the centres of the nuclei in the impact parameter plane (the more central the smaller the impact parameter).

relate the quarkonium production to either the number of participants  $N_{part}$  or with a parameter  $L$ , representing the length traversed from the parton collision point through the nuclear matter. Both quantities can be determined via Glauber model calculations [41] and reflect the volume of medium achieved in the collision. To observe a deviation, a reference process defining the normal or expected behaviour has to be chosen. Basically there are two different approaches for this reference process:

- The first approach relates the observed quarkonia production to a different process measured simultaneously. An example is the Drell-Yan process ( $q\bar{q} \rightarrow l^+l^-$ ) as it is used as a reference at the SPS experiments. The Drell-Yan process is a hard process, meaning that it includes large momentum transfers of more than 1 GeV/c. The necessary momentum transfers takes place during the first phases of the collision, thus the cross-section of the Drell-Yan process is expected to scale with the number of initial binary collisions. Since the Drell-Yan process is, in addition, expected not to be affected by a deconfined medium, the ratio between the two processes will be constant if the charmonium production is not affected by the medium. If charmonium production is affected, the ratio is expected to decrease with increasing centrality.
- The second approach, followed at RHIC, reflects the general question as to how the observations change when comparing binary proton-proton collisions to the collision of two nuclei. A basic model would predict that the cross-sections for hard processes of two colliding nuclei A and B can be described as proton-proton cross-section. Models include the geometry of the colliding nuclei and use the number of collisions as a scaling variable. For charmonium production the nuclear modification factor is defined in equation(2.6)

$$R_{AA}(c) = \frac{\sigma_{Ninel}^{pp}}{\sigma_{J/\psi}^{pp}} \cdot \frac{N_{J/\psi}^{AA}(c)}{N_{binary}(c)} \quad (2.6)$$

where  $\sigma_{Ninel}^{pp}$  and  $\sigma_{J/\psi}^{pp}$  are the total inelastic cross-section and the cross-section for  $J/\psi$  production in pp collisions, respectively.  $N_{J/\psi}^{AA}(c)$  is the measured number of  $J/\psi$  per A-A collisions at centrality  $c$ , and  $N_{binary}(c)$  is the number of binary collisions for the same centrality. By definition, if no nuclear modification, meaning no medium effect, is present, one expects  $R_{AA} = 1$ . Any deviation from one can then be attributed to the produced medium.

The existing experimental status of  $J/\psi$  production is described in the following sections. The measurements performed by the three fixed target experiments NA38 [42], NA50 [43] and NA60 [44] and the measurements of the collider experiment PHENIX [45] are described along with the most prominent theoretical models and their possible implications for the LHC.

Table 2.3: Number of heavy quark-anti-quark pairs per central collision (small impact parameter) for SPS, RHIC and LHC energies

|                | SPS $\sqrt{s}=17$ AGeV | RHIC $\sqrt{s}=200$ AGeV | LHC $\sqrt{s}=5500$ AGeV |
|----------------|------------------------|--------------------------|--------------------------|
| $N_{c\bar{c}}$ | 0.2                    | 10                       | 120                      |
| $N_{b\bar{b}}$ | -                      | 0.05                     | 5                        |

## 2.3 Results from the CERN SPS

### 2.3.1 Results from NA38

There has been a series of experiments at the SPS, starting with NA38 continuing with NA50 and then NA60 over a fairly long period from 1986 until now.

The NA38 experiment consisted mainly of a muon spectrometer [46]: tracks were deflected by a toroidal magnet, and reconstructed using two sets of four Multi Wire Proportional Chambers(MWPCs). Muon pairs were detected in the pseudo rapidity interval  $2.8 < \eta < 4.0$ .

The first signal of the  $J/\Psi$  suppression was observed in 1989 by the NA38 experiment [42]. They examined oxygen-uranium collisions with an incident oxygen beam energy of 200 GeV per nucleon, resulting in a collision energy of  $\sqrt{s} = 20$  GeV per nucleon. Figure 2.5 shows the measured  $J/\psi$  yield normalised to number of dimuons pairs in the mass region 2.7-3.5 GeV/c<sup>2</sup> as a function of the measured transverse energy as a measure of centrality. A similar pattern was observed later in sulphur-uranium collisions [42]. With increasing centrality, the nuclear matter is more compressed, and at some point a volume of deconfined matter forms, containing free colour charges. Due to these charges the charmonium binding potential is screened, the bound state is dissolved and the measured  $J/\psi$  production decreases with respect to the reference process.

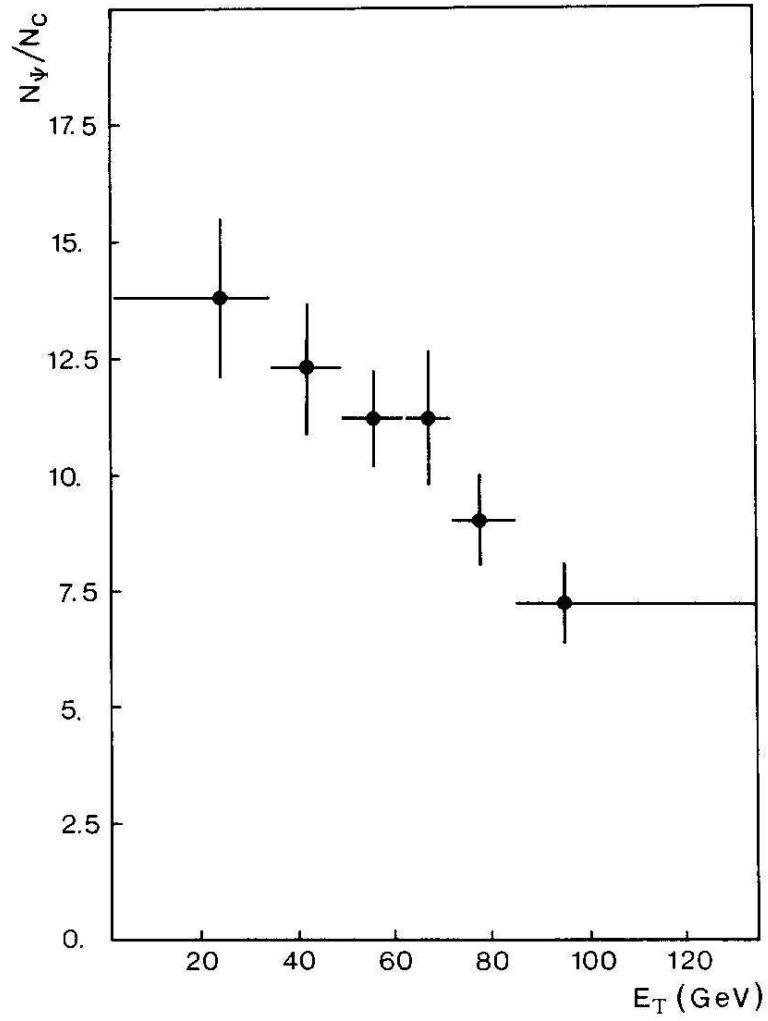


Figure 2.5: The evolution of the ratio of produced  $J/\psi$  over produced Drell-Yan dimuons pairs as a function of the transverse energy along with systematic , as measured by NA38 [46]. Systematic error is included in error bars.

### 2.3.2 Results from NA50

NA50 was a high luminosity fixed target experiment, essentially dedicated to the study of dimuon production in Pb-Pb collisions at 158 GeV per nucleon. The NA50 apparatus was also used for the study of the p-A system. NA50 was the upgraded version of the NA38 experiment for the study of Pb-Pb interactions at 158 GeV/nucleon. The main change was the introduction of a new target system under vacuum [47], which allowed a better rejection of out-of-target interactions and, in particular, of Pb-air interactions. Furthermore, in order to identify almost simultaneous multiple interactions, a new method was developed based on the shape analysis of the signal in the Electromagnetic Calorimeter. The setup is described in detail in Ref. [43].

Figure 2.6 shows the comparison of the Pb-Pb results with lighter collision systems. The ratio of produced dimuons from  $J/\psi$  to dimuons from the Drell-Yan process is shown as a function of the length  $L$  of traversed nuclear matter together with the results obtained in S-U (NA38) and p-A (NA50) interactions.  $L$  is obtained from Glauber model calculations [41] and is directly related to the centrality of the collision. The model estimates the mean length  $L$  traversed by the  $J/\psi$  by assuming that the  $J/\psi$  can be created anywhere along the length of the interaction volume (assumed to be the intersection of two hard spheres). The solid line represents the suppression obtained from proton-proton and proton-nucleus collisions. Thus the line shows the amount of suppression due to nuclear absorption, that cannot be related to dissociation due to deconfinement. A deviation is observed for  $L > 7.5$  fm [48]. At this centrality the energy density is sufficiently high to create deconfined matter, leading to dissociation of charmonium beyond the dissociation by

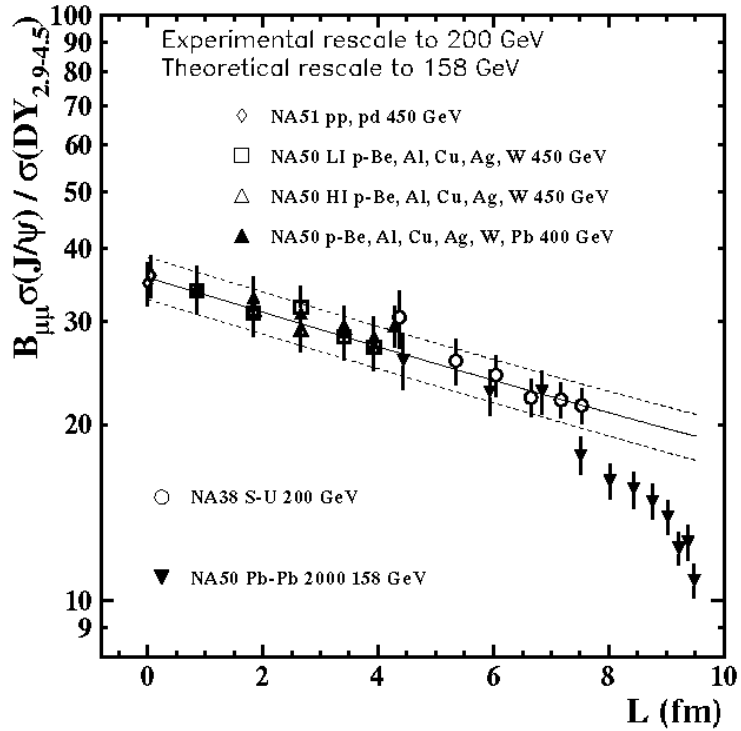


Figure 2.6: The  $J/\psi$  suppression pattern as measured by the NA50 experiment. The solid line indicates the normal nuclear absorption as expected from comparison to proton nucleus data.  $L$  is the length of traversed nuclear matter. Anomalous suppression is observed for  $L > 7.5$  fm [48]. The measured data have been rescaled to 158 GeV/nucleon.

nucleon scattering. However an alternative description to this suppression can also be made in terms of co-movers (hadrons move along the  $J/\psi$  with small relative velocity, excite the nuclear medium and thus disrupt  $J/\psi$ ) [49] that does not require deconfinement.

### 2.3.3 Results from NA60

NA60 has been the last heavy ion experiment running at the SPS and performed a measurement of dimuon production in p-A and In-In collisions. NA60 had a silicon pixel detector to get a precise measurement of the interaction vertex. In addition a vacuum target cell was added to suppress the beam gas interactions which could be mistaken as peripheral collisions.

The suppression of charmonium states in nuclear collisions is considered as one of the most powerful signatures of the production of a deconfined state [9]. However, cold nuclear effects, and in particular the interaction of the projectile and target nucleons with  $c\bar{c}$  pair, sizeably contribute to the observed suppression [50]. Such effects are usually studied in p-A collisions, then extrapolated to A-A collisions and compared with the observed yield in nuclear collisions, as a function of centrality.

Figure 2.7 shows the results of nuclear effects on  $J/\psi$  production in p-A collisions at 158 GeV and 400 GeV. In order to provide reference p-A data collected at the same energy and kinematic domain. NA60 also studied  $J/\psi$  production in p-A collision at 158 GeV. The incident beam, with an intensity of  $5 \cdot 10^8$  protons/s, was incident on various sub targets, with the mass ranging from 9 (Be) to 238 (U). The analysis

of the  $J/\psi$  production data at 158 GeV was performed in the rapidity domain  $0.28 < y_{cm} < 0.78$ , covered with reasonable acceptance by all the sub-targets, and for rapidity range  $-0.17 < y_{cm} < 0.33$  for 400 GeV.

In Figure 2.7 [51] the y axis represents the cross-section ratios  $\sigma_{pA}^{J/\psi} / \sigma_{pBe}^{J/\psi}$  for the 7 nuclear targets (Be, Al, Cu, In, W, Pb and U) with mass number A with respect to lightest one (Be). This was done so that beam luminosity factors cancel out, apart from a small beam attenuation factor. Along the x axis is L, the mean thickness of the nuclear matter crossed by the  $c\bar{c}$  pair in its way through the nucleus. The same figure, shows the results of the same analysis, carried out on a data sample at 400 GeV. These results refer to the rapidity range  $-0.17 < y_{cm} < 0.33$ , corresponding to the same rapidity in the lab as 158 GeV. Performing a Glauber fit to the data, the cross-section obtained for the NA60 p-A data is :  $7.6 \pm 0.7$  (stat.)  $\pm 0.6$  (syst.) *mb* at 158 GeV and  $4.3 \pm 0.8$  (stat.)  $\pm 0.6$  (syst.) *mb* at 400 GeV. The  $J/\psi$  absorption cross-section result at 400 GeV is smaller with respect to the one extracted from the 158 GeV, pointing to an energy dependence of this quantity. The lower slope corresponding to 158 GeV indicates that the nuclear effects are more important when moving towards lower energy. Systematic errors include uncertainties on the target thickness on the y distribution used in the acceptance calculation and on the reconstruction efficiency.

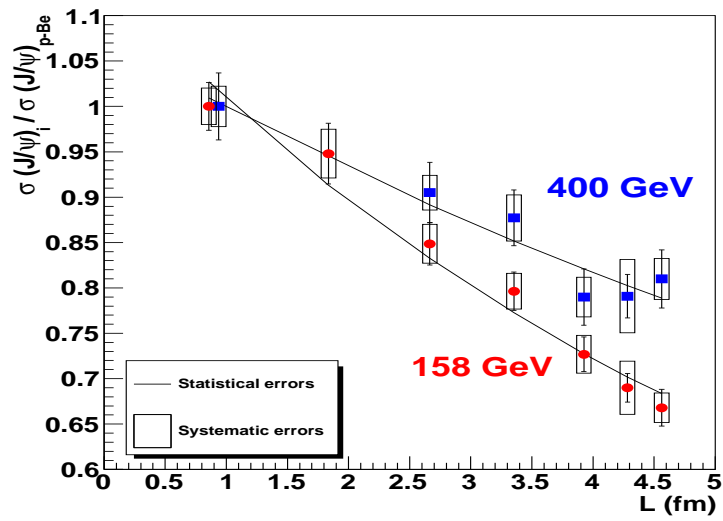


Figure 2.7:  $J/\psi$  absorption cross-section as a function of  $L$ , the mean thickness of nuclear matter crossed by the  $c\bar{c}$  pair in its way through the nucleus [51]. On the y-axis the index  $i$  refers to 7 nuclear targets. The nuclear effects in lower energy range change the slope as seen in the figure. Systematic errors include uncertainties on the target thickness, on the  $y$  distribution used in the acceptance calculation and on the reconstruction efficiency.

## 2.4 Results from RHIC

The  $J/\psi$  production mechanism is expected to depend on rapidity at RHIC energies centre-of-mass energy of 200 GeV. In the mid rapidity region, it is expected to be dominated by gluon fusion but can also come from gluon or quark fragmentation or from feed down from heavier mesons. In the forward rapidity, it is hypothesised that the dominant production comes from intrinsic heavy flavour components in the proton wave function [52].

The PHENIX collaboration compared  $J/\psi$  data in A-A collisions to pp ones. Such a comparison was carried out using the  $R_{AA}$  ratio, which can be written as in equation(2.6).

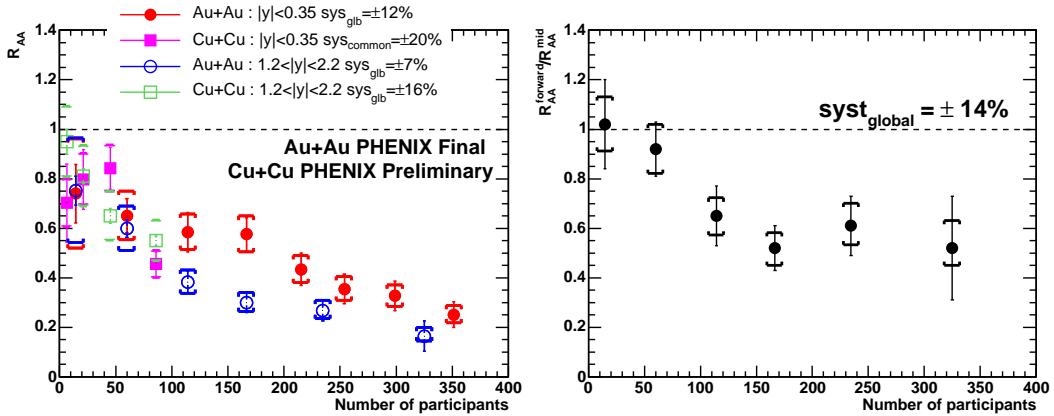


Figure 2.8: The nuclear suppression factor for Au-Au (circle) and Cu-Cu (square) collisions at mid-rapidity (closed symbols) and at forward-rapidity (open-symbols) at  $\sqrt{s} = 200$  GeV, as a function of centrality [53]. The  $J/\psi$  production is suppressed for large number of participants. Right: Ratio of  $R_{AA}$  at forward-rapidity to that at mid-rapidity in Au-Au collisions

Figure 2.8 (left) shows the suppression factor observed by the PHENIX collaboration at RHIC [45] in Cu-Cu and Au-Au at  $\sqrt{s} = 200$  GeV, as a function of centrality. The  $J/\psi$  production is suppressed for large numbers of participants.  $R_{AA}$  is similar between mid-rapidity and forward-rapidity up to  $N_{part} \approx 100$  and stronger suppression is observed at forward rapidity for  $N_{part} > 100$ . Figure 2.8 (right) shows the ratio  $R_{AA}$  at forward-rapidity to that at mid-rapidity, which goes down to  $\approx 0.6$  for  $N_{part} > 100$ . Figure 2.9 shows a comparison of the PHENIX and STAR [3] results for nuclear modification in Cu-Cu at  $\sqrt{s} = 200$  GeV. Suppression is observed in PHENIX data. The  $R_{AA}$  vs  $N_{part}$  was obtained using minimum bias Cu-Cu collision only.

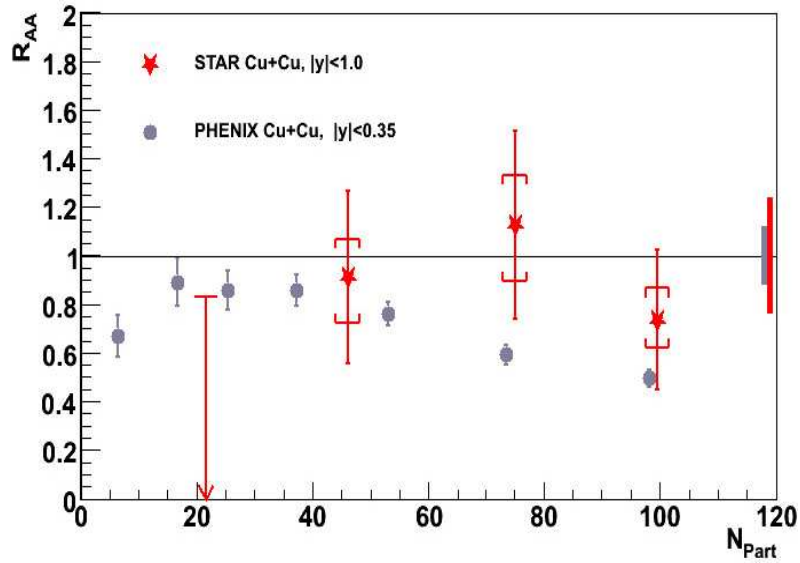


Figure 2.9: The nuclear suppression factor of  $J/\psi$  as a function of centrality (represented by the number of participants). Suppression is more clear in PHENIX data [3]. STAR data points have statistical (bars) and systematic (caps) uncertainties. The solid line and band show the average and uncertainty of the two 0-20% data points.  $R_{AA}$  equal to 1 means no suppression.

## 2.5 Theoretical interpretation

The models can be divided into two classes: pure dissociation models and models including recombination. The pure dissociation models [54] of quarkonium are computed using lattice QCD calculations. This leads to a charmonium dissociation temperature close to the proposed critical temperature of 170 MeV [54] [55] [56] [57] [58]. Higher charmonium states dissociate sooner due to their size. Since a large fraction of the measured  $J/\psi$  originate from decay of the higher excited charmonium states, the total yield of  $J/\psi$  will decrease as well. This effect, called sequential dissociation [59] is used to explain the suppression pattern observed at the SPS.

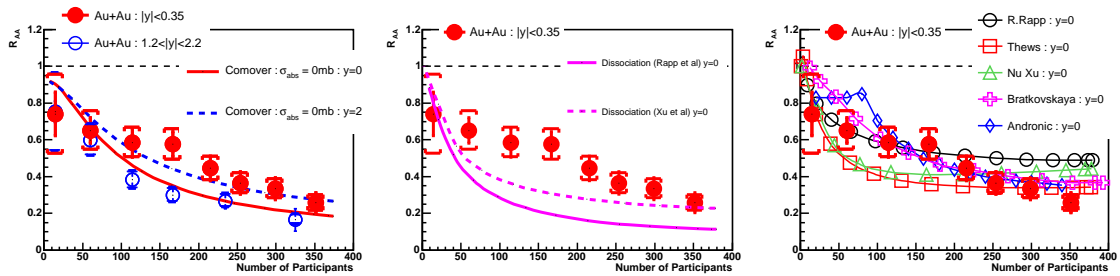


Figure 2.10: Left: Comparison of  $R_{AA}$  to the models with dissociation by comovers [54]. Middle: Comparison of  $R_{AA}$  to the models with dissociation by thermal gluons [60]. Right: Comparison of  $R_{AA}$  to the models with dissociation and recombination of  $J/\psi$  [61, 64].

According to this model one would expect that at RHIC, due to the higher energy density, the ground state melts and charmonia are almost completely suppressed. Figure 2.10 (left and middle) shows a comparison of  $R_{AA}$  in Au-Au collisions to the models involving only the dissociation of  $J/\psi$  by comoving partons and hadrons

and by thermal gluons, respectively [60]. These models [60] over-predict the suppression. Even before the suppression was measured, different authors argued that the relatively large number of charm quarks produced at RHIC ( $\sim 10$ ) would lead to charmonium production at the hadronization stage. These models became known as recombination models. Several models include the charm hadronization in their calculations. A comparison of these recombination models [60] [61] [62] [63] [64] is shown in the figure 2.10. The details of these models are not described in this thesis. The recombination models include the assumption that the charmonium is dissolved in the deconfined medium and they do not contradict the original idea of charmonium suppression.

However at the LHC about 100  $c\bar{c}$  -pairs per central collision will be produced and about 1  $J/\psi$ . At the LHC a higher energy density is expected compared to RHIC. Thus all initially produced  $J/\psi$  are expected to be suppressed. But due to the large number of charm quarks produced within the hadronization phase it is expected to produce an even higher  $J/\psi$  yield compared to production from initial collisions [65]. The  $J/\psi$  should be strongly enhanced, as predicted by the recombination models.

In the next chapter I will concentrate on  $J/\psi$  in p-p collisions mainly for two reasons. Firstly the  $J/\psi$  cross-section comparison with the QCD prediction and secondly to provide a benchmark to compare p-p collision with heavy ions.

# Chapter 3

## The ALICE experiment at the LHC

### 3.1 LHC

The Large Hadron Collider [66] is an accelerator complex at the CERN laboratory in Switzerland, which accelerate protons and/or nuclei to unprecedented energies, allowing access to the highest energy densities and temperatures ever created in man-made experiments. The LHC ring sits in the tunnels of its predecessor, the LEP (Large Electron and Positron) collider, crossing the French-Swiss border with a circumference of 27 km. It has 4 intersection points between the two conversely circulating beams where collisions occur, marking the sites of the four detector experiments: ALICE [1], ATLAS [68], CMS [69] and LHCb [70], as in Figure 3.1.

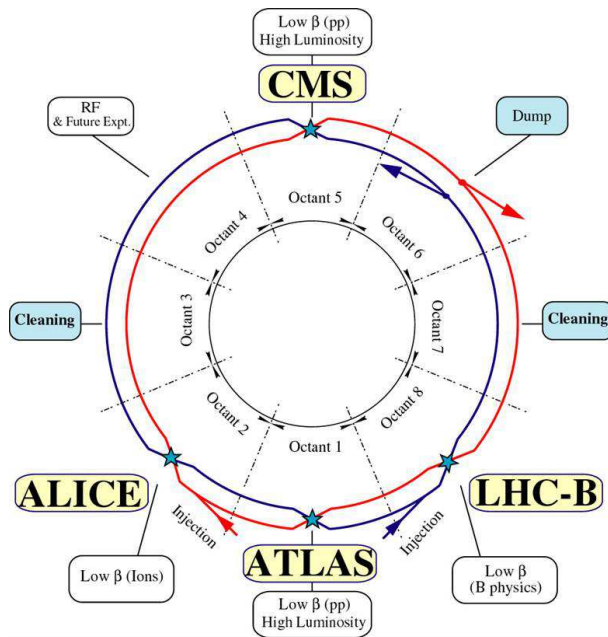


Figure 3.1: Schematic layout of the LHC [66]

The protons fed into the LHC are first created by stripping hydrogen atoms from their electrons. These protons are then injected from the LINAC2 (linear accelerator) into the Proton Synchrotron Booster which accelerates the protons to an energy of 1.4 GeV before injecting them into the Proton Synchrotron. The PS ring accelerates protons up to 25 GeV, at which point they are fed into the SPS, which accelerates protons to 450 GeV. Then they can be fed in either direction into the LHC, where they achieve a maximum energy of 7 TeV. Figure 3.2 shows the layout of the injection complex.

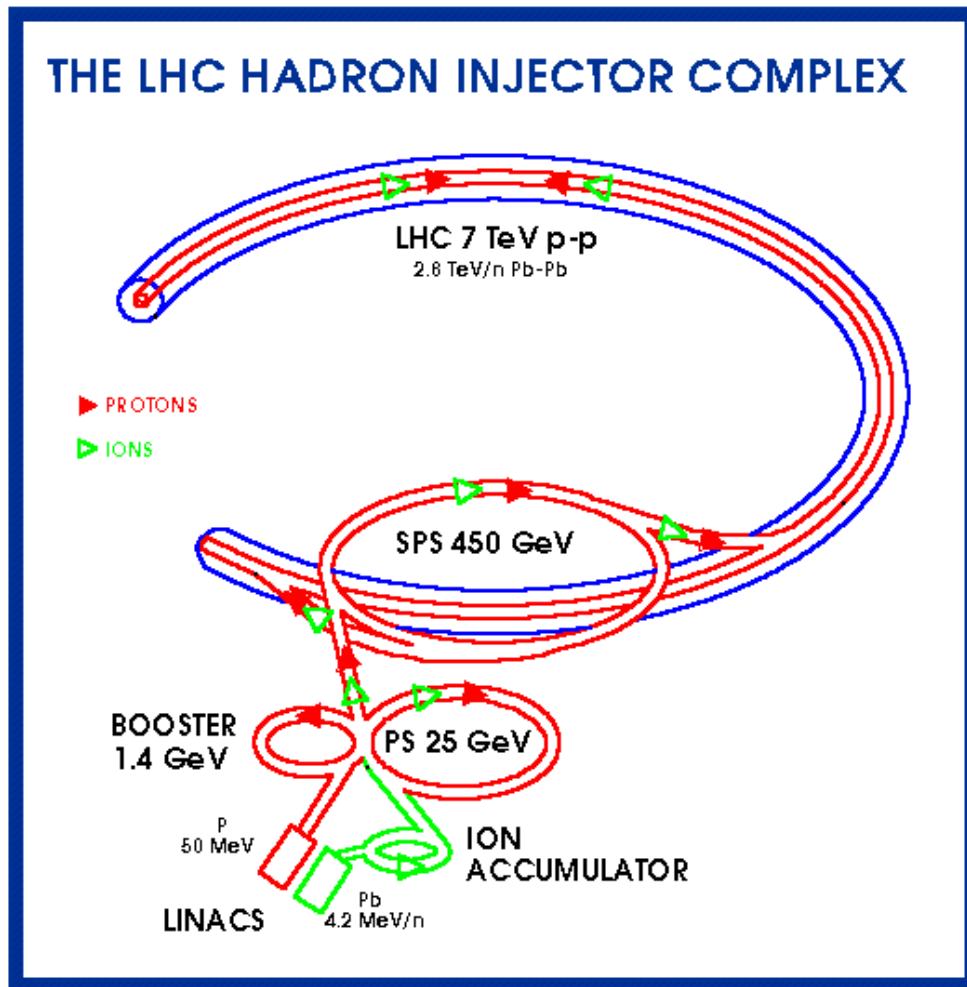


Figure 3.2: The various stages of acceleration of both protons and ions on their way to injection into the LHC [71].

## 3.2 The ALICE detector

The ALICE (A Large Ion Collider Experiment) [1] experiment is a general-purpose heavy ion detector. It has been designed to detect, measure and identify mid-rapidity hadrons, leptons and photons produced in heavy ion interactions. In addition it will study collisions of protons (both pp and pA) which primarily provide reference data for nucleus-nucleus collisions. ALICE is required to track and identify particles, from very low ( $\approx 100\text{MeV}/c$ ) to fairly high ( $\approx 100\text{ GeV}/c$ ) transverse momentum  $p_t$ , to reconstruct short-lived particles such as hyperons and do this in a high multiplicity environment. The detectors are designed to cope with charged particle densities  $dN_{\text{ch}}/dy$  of up to 8000. Theoretical predictions for the multiplicity in central Pb-Pb collisions at the LHC currently range from 2000 to 6000 charged particles per unit rapidity giving a comfortable safety margin. The key design features of the main ALICE sub-detectors are described in this chapter. A cutaway drawing of the ALICE experiment is shown in figure 3.3. It consists of a central detector system, covering mid-rapidity  $|\eta| \leq 0.9$ <sup>1</sup> over the full azimuth, and several forward systems. The central system is installed inside a large solenoidal magnet which generates a magnetic field of up to 0.5 T. The main factor in choosing this value of the magnetic field is to optimize the range over which accurate tracking can be done. This means that the radius of curvature should lead to sagittas over the typical allowed length of track that are well measurable by the detector. Too

---

<sup>1</sup>Pseudorapidity,  $\eta$ , is a commonly used variable describing the angle of a particle relative to the beam axis. Mathematically it can be represented as

$$\eta = -\ln \left[ \tan \left( \frac{\theta}{2} \right) \right]$$

strong a field leads to very curved tracks which are difficult to reconstruct. Too weak a field leads to straight tracks which give poor momentum resolution. The central barrel system includes, from the interaction vertex to the outside, six layers of high-resolution silicon detectors (Inner Tracking System-ITS), the main tracking system of the experiment (Time-Projection Chamber - TPC), a Transition Radiation Detector for electron identification (TRD), and a particle detector which can discriminate between lighter and heavier particle of the same momentum using their time of flight ( Time-Of-Flight - TOF). The central system is complemented by two small-area detectors: an array of ring-imaging Cherenkov detectors for the identification of high-momentum particles (High-Momentum Particle Identification Detector-HMPID), and two electromagnetic calorimeters consisting of array of high-density crystals (Photon Spectrometer - PHOS and EMCal).

The forward muon arm consists of a complex arrangement of absorbers, a large dipole magnet, and fourteen planes of tracking and triggering chambers [67]. An absorber positioned very close to the vertex shields the muon spectrometer. A system of scintillators and quartz counters (VO) and (TO) provide fast trigger signals, and two sets of hadron calorimeters, located about 115 m away on either side of the interaction vertex, measure the centrality (Zero-Degree Calorimeter - ZDC). Another forward detector in ALICE is the Photon Multiplicity Detector (PMD), which measures the multiplicity and spatial distribution of photons produced in the collisions. An array of scintillators (ACORDE) on the top of the L3 magnet is used to trigger on cosmic rays.

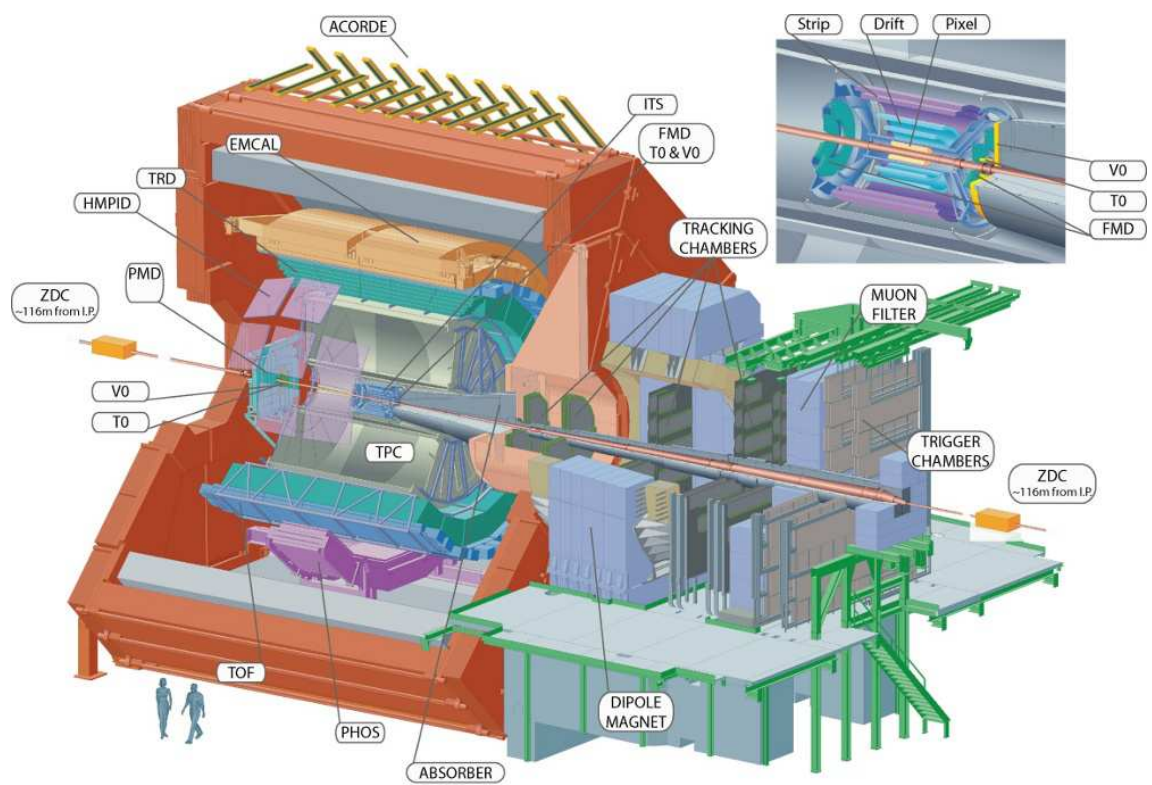


Figure 3.3: The ALICE detector schematic layout.

### 3.2.1 Inner Tracking System (ITS)

The main purpose of the ITS is the detection of secondary vertices (hyperons and charm particles) and the stand-alone track finding of low- $p_t$  charged particles, down to a  $p_t$  of 20 MeV/ $c$  for electrons. Also it has a number of additional roles: improvement of the momentum resolution at large momenta, momentum reconstruction of low energy particles, and their identification. The ITS recognises particles containing heavy quarks by identifying the point at which they decay.

The ITS is made up of six layers of silicon detectors, shown in figure 3.4. It is required to localise the primary vertex to better than 100  $\mu\text{m}$ , and give excellent spatial resolution so that an impact parameter of better than 60  $\mu\text{m}$  can be achieved for low momentum particle, as well as coping with a high track density. The Silicon Pixel Detector (SPD) makes up the inner two layers, with a spatial resolution of 12  $\mu\text{m}$  which optimises impact parameter resolution, followed by SDD (Silicon Drift Detector) layers. These two detectors handle the high particle density of heavy ion collisions. The SSD (Silicon Strip Detector) layers are placed in the region where the particle density reduces to below 1 per  $\text{cm}^2$ .

#### Silicon Pixel Detector (SPD)

The two innermost layers of the ITS as shown in figure 3.3 are fundamental in determining the vertexing quality of ALICE (determination of the position of the primary vertex and measurement of the impact parameter of secondary tracks from the weak decays of strange, charm and beauty particles). They operate in a region

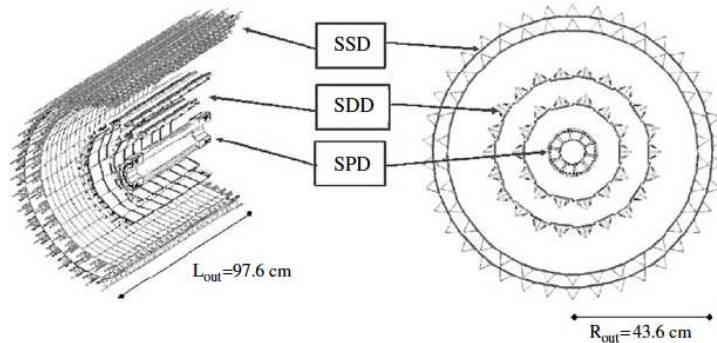


Figure 3.4: ITS showing six layers of silicon detector.

where the track density can exceed  $50 \text{ tracks/cm}^2$ . Thus it is a detector of high precision and granularity and also operates in a relatively high-radiation environment. The SPD is based on hybrid silicon pixels, consisting of a two dimensional matrix of reverse biased silicon detector diodes bump bonded to readout chips. Each diode is connected through a conductive solder bump to a contact on the readout chip corresponding to the input of an electronics readout cell. The readout is binary: in each cell, a threshold is applied to the pre-amplified shaped signal and the digital output level changes when the signal is above a set threshold. The basic building block of the ALICE SPD is the ladder, consisting of a pixel detector matrix bonded to 5 front-end chips. The detector matrix consists of  $256 \times 160$  cells, each measuring  $50 \mu\text{m}$  in the  $r\phi$  direction by  $425 \mu\text{m}$  in the  $z$  direction. Each detector ladder measures  $12.8 \text{ mm}$  ( $r\phi$ )  $\times$   $70.7 \text{ mm}$  ( $z$ ). Each front-end chip contains the electronics for the readout of a sub matrix of  $256$  ( $r\phi$ )  $\times$   $32$  ( $z$ ) detector cells. The detector is  $200 \mu\text{m}$  thick and the electronics chip is  $150 \mu\text{m}$  thick.

## Silicon Drift Detector (SDD)

SDDs have been selected to equip the two intermediate layers of the ITS as shown in figure 3.3, since they couple a very good multi-track capability with  $dE/dx$  information. The SDDs, with  $7.25 \times 7.53 \text{ cm}^2$  active area each, are mounted on linear structures called ladders, each holding six detectors for layer 3, and eight detectors for layer 4. The layers are located at average radii of 14.9 and 23.8 cm respectively and are composed of 14 and 22 ladders respectively.

SDDs, like gaseous drift detectors, exploit the measurement of the transport time of the charge deposited by a traversing particle to localise the impact point in one of the dimensions, thus enhancing resolution and multi-track capability at the expense of speed. They are therefore well suited to applications in which very high particle multiplicities are coupled with relatively low event rates.

A linear SDD has a series of parallel, implanted p+ field strips, connected to a voltage divider on both surfaces of the high-resistivity n-type silicon wafer. The voltage divider is integrated on the detector substrate itself. The field strips provide the bias voltage to fully deplete the volume of the detector and they generate an electrostatic field parallel to the wafer surface, thus creating a drift region.

Electron-hole pairs are created by the charged particles crossing the detector. The holes are collected by the nearest p+ electrode, while the electrons are focused into the middle plane of the detector and driven by the drift field towards the edge of the detector where they are collected by an array of anodes composed of n+ pads. The small size of the anodes, and hence their small capacitance ( 50fF), imply low

noise and good energy resolution. The readout is at the end of the SDD cell and measures the charge deposited in time slices. The amount of collected charge is measure of particle energy loss  $dE/dx$ . With a bias voltage of about 1.65 kV the charge drifts at 5.6 microns/ns (which can be checked by calibration triggers to get accurate local triggers) and is read out using the PASCAL chip, which samples the charge arriving at the anode at 40.08 MHz (LHC clock rate) and digitizes.

Owing to diffusion and mutual repulsion during the drift, the electrons reach the anode region with a Gaussian distribution. The coordinate perpendicular to the drift direction is given by the centroid of the collected charge. The coordinate along the drift direction is measured by the centroid of the signal in the time domain, taking into account the amplifier response. The SDDs are positioned so that the electrons drift orthogonal to the beam axis and therefore to the ALICE magnetic field. The low magnetic field would cause a marginal effect on the electron cloud formation and essentially none on the charge transport, since the Lorentz force is compensated by the confining electric field. The average resolution is 35 microns in  $r\phi$  direction and 25 microns in  $z$  direction.

### **Silicon Strip Detector (SSD)**

The two outer layers of the ITS as shown in figure 3.3 are crucial for the connection of tracks from the ITS to the TPC (Time Projection Chamber). They provide  $dE/dx$  information to assist particle identification for low-momentum particles. Both outer layers of the ITS consist of double-sided SSDs with a 35 mrad stereo angle. Each detector has an active area of 73 mm by 40 mm. The active area is surrounded

by bias and guard rings which occupy 1 mm along each side of the detector. The implanted strips are inclined with a 17.5 mrad angle with respect to the 40 mm side of the detector. Therefore the patterns are identical on the p and the n-sides of the detector. The stereo angle is small in order to minimise of ambiguities for the high particle densities expected. The detectors are mounted with the strips (nearly) parallel to the magnetic field, so that the best position resolution is obtained in the bending direction.

### **3.2.2 Time Projection Chamber (TPC)**

The Time Projection Chamber (TPC) is the main tracking detector in the central barrel of the ALICE experiment as shown in figure 3.3. With its large acceptance, it enables us to analyse individual events and perform charged particle exclusive analysis in a wide range of pseudo-rapidity  $|\eta| \leq 0.9$ . Its function is to provide track finding, charged particle momentum measurement, particle identification, and two-track separation in the region  $p_t \leq 10$  GeV/ $c$  and pseudo-rapidity  $|\eta| \leq 0.9$ . Particles can be identified within the TPC by their specific loss of energy due to interactions with the TPC gas. TPC is the main detector for the hadronic observables in both heavy-ion and proton-proton collisions.

#### **TPC Layout**

The TPC is cylindrical in shape with an active gas volume that ranges from about 85 cm to 250 cm, in the radial direction, and has a length of 500 cm along the beam

direction resulting in an active volume of  $95\text{m}^3$ , the largest TPC ever built. The detector is made of a large cylindrical field cage, filled with Ne/CO<sub>2</sub>/N<sub>2</sub> (90:10:5) which is needed to transport the primary electrons over a distance of up to 2.5 m on either side of the central electrode to the end-plates. N<sub>2</sub> is also used as it is more adequate quencher for neon.

The advantage of this gas mixture is that it shows almost no ageing effects in contrast to other mixtures like CF<sub>4</sub>. Further advantages are a short drift time, small diffusion and a low radiation length. These nice features have to be paid for with a strong dependence of the drift velocity on the temperature. For this reason the temperature has to be kept constant within an interval of 0.1 K. To prevent heat conduction from the outer detectors a thermal shield is added between the TPC and the TRD (Transition Radiation Detector).

The central electrode operates at a voltage of 100 kV, giving a field gradient of 400 V/cm and a maximum drift time of 106  $\mu\text{s}$ . The signals are read out at the two end caps by 72 multi-wire proportional chambers. Each of these chambers has three layers of wires. To prevent space charge effects within the detector volume, the outermost wire layer of the read-out chambers is used as a gating grid such that electrons are only collected in the chambers if a Level-One trigger was sent. The TPC detector is shown in the figure 3.5

ALICE is the only experiment at the LHC using a large TPC as the central tracking detector. This can be understood when looking at the desired physics observables. The ALICE TPC is divided in two drift regions by the central electrode located at its axial centre. A field cage creates a uniform electric field along each half

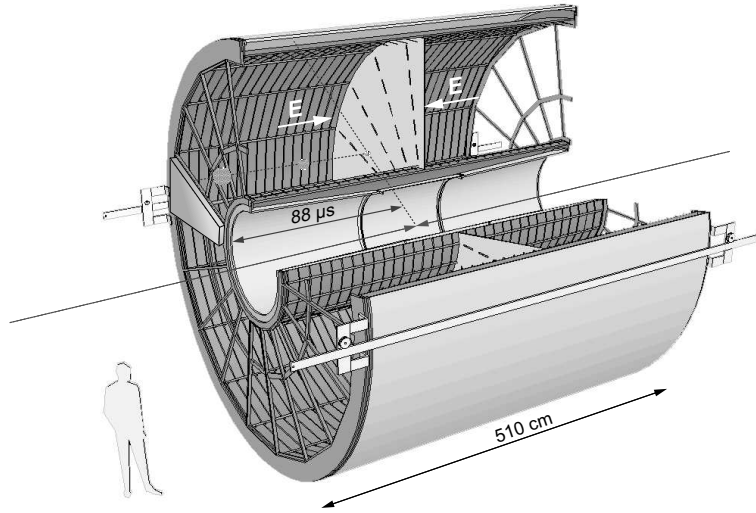


Figure 3.5: The Time Projection Chamber (TPC) layout.

of the chamber. Charged particles traversing the TPC volume ionise the gas along their path, liberating electrons that drift towards the end plates of the chamber is shown in figure 3.6. The necessary signal amplification is provided through avalanche effect in the vicinity of the anode wires. Moving from the anode wire towards the surrounding electrodes, the positive ions created in the avalanche induce a positive current signal on the pad plane. This current signal, which is characterised by a fast rise time (less than 1 ns) and a long tail with a rather complex shape, carries a charge of 4.8fC, for a minimum ionising particle.

### 3.2.3 Transition-Radiation Detector (TRD)

Transition radiation is produced by the passage of highly relativistic charged particles through layers of material with different indices of refraction. Transition radiation detectors are unique tools for separating high energy electrons and positrons

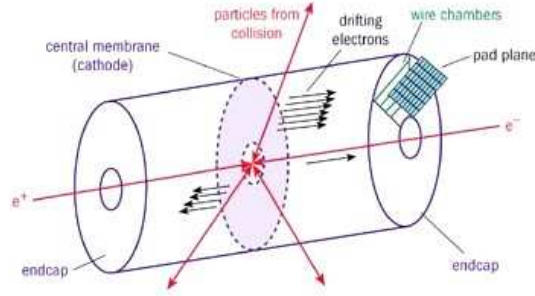


Figure 3.6: The Time Projection Chamber ionisation cage.

from charged pions. Unlike pions, electron and positrons are not subject to the strong force. This makes them ideal probes to study the hottest and densest phase of such collisions. In ALICE the Transition Radiation detector (TRD) will be used to study the production of  $J/\psi$  and  $\Upsilon$  -particles both in Pb-Pb and pp collisions where its principal use is the identification of electrons among the charged tracks. It has two main purposes: the identification of electrons over a large momentum range via their emission of transition radiation, and to serve as a trigger device for events containing high  $p_T > 3 \text{ GeV}/c$  electrons. In addition, since it provides additional points to charged particle tracks, it increases the tracking resolution.

The detector is shown in figure 3.7. It consists of 540 read-out chambers arranged in 18 super modules covering the same angle as a corresponding TPC sector. Each of these super modules consists of 30 chambers arranged in 6 radial layers and 5 stacks in the  $z$ -direction. The total active volume is about  $27 \text{ m}^3$ , filled with a mixture of Xenon (85%) and  $\text{CO}_2$  (15%). Since Xenon is a very rare noble gas (0.08 ml Xenon in  $1 \text{ m}^3$  air), the amount of Xenon used in the TRD represents roughly one years worth of production worldwide. This puts strong requirements in terms of gas tightness on the detector. The total sensitive area of the detector is

roughly  $750\text{m}^2$  divided into 1.16 million read-out pads. Each channel is individually readout; 18 read-out channels are bundled and connected to a highly integrated multi chip module (MCM). The MCM contains two main parts: the pre-amplifier and shaper chip ( PASA ) and the Tracklet processor (TRAP) [72] containing a 10 bit analog to digital converter with a sampling rate of 10MHz, configurable digital filters providing further shaping, pedestal subtraction, tail cancellation and zero suppression. In addition short tracks within one chamber, called tracklets, are used for the trigger on high  $p_t$  particles.

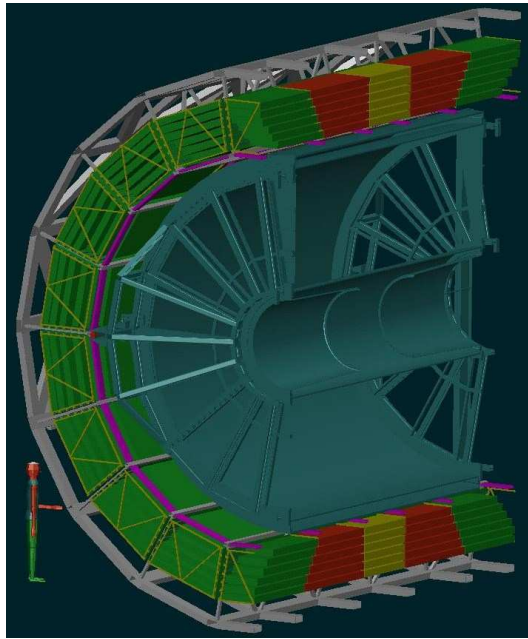


Figure 3.7: Schematic drawing of (one half) of the ALICE TRD. The complete detector consists of 540 read-out chambers (green, red and yellow) arranged in 18 super modules covering the full azimuth. Each of these super modules consists of 6 radial layers and 5 stacks of chambers in the z-direction. The total sensitive area of the detector is  $750\text{m}^2$  divided into 1.16 million read-out channels.

## Electron Identification

The principle the TRD is used to discriminate between electrons and heavier particles in the emission of transition radiation. Transition radiation was predicted in 1945 [73] and first observed in 1959 [74]. It denotes the effect that a charged particle, moving with a certain velocity, undergoing transitions between materials of different dielectrical properties emits electromagnetic radiation. Since the electrical field surrounding every charged particle depends not only on the charge but also on the speed of the particle and on the dielectric properties of the surrounding medium, changing one of these parameters leads to a change in the field. For example changing the velocity of a charged particle leads to the emission of Bremsstrahlung. Changing the medium surrounding the particle also leads to a changing field and thus to the emission of transition radiation. A detailed theoretical treatment can be found in [75] [76]. Important for the design of a transition radiation detector are the probability to produce a transition radiation photon and its energy.

The probability to produce a photon during one transition of a charged particle depends on the relativistic  $\gamma$ -factor, which is directly related to the mass of a particle. This enables, just by the observation of transition radiation, the distinction between different particles without the need of a precise momentum measurement like is needed for particle identification via the specific energy loss of particles in the medium.

Table 3.1 shows values for  $\gamma$  for different particles with different momenta. The threshold transition radiation emission depends on the thickness and on the plasma frequency difference of the radiator materials. For polypropylene/air radiators parti-

cles with a  $\gamma$  exceeding 1000 produce transition radiation [77]. Over a large momentum range (1-100 GeV/c) only electrons are expected to emit transition radiation. Thus transition radiation detectors are very well suited to separate especially electrons from heavier particles. The probability to emit a transition radiation photon during one transition is of order of  $\alpha_{em} = 1/137$ . For this reason transition radiation detectors are designed such that the particles undergo not one but many transitions.

Table 3.1: The relativistic  $\gamma$  factor for different particles with various momenta. Only particles with  $\gamma > 1000$  produce significant transition radiation for a typical detector with polypropylene/air interfaces.

| Particle                  | e        | $\mu$    | $\pi$    | K        | p        |
|---------------------------|----------|----------|----------|----------|----------|
| Mass(MeV/c <sup>2</sup> ) | 0.511    | 105.658  | 139.57   | 493.677  | 938.272  |
| p (GeV/c)                 | $\gamma$ | $\gamma$ | $\gamma$ | $\gamma$ | $\gamma$ |
| 0.1                       | 195.     | 1.4      | 1.2      | 1.0      | 1.0      |
| 1.                        | 1956.    | 9.5      | 7.2      | 2.26     | 1.5      |
| 10.                       | 19569.   | 94.5     | 71.2     | 20.3     | 10.7     |
| 100.                      | 195000.  | 946.     | 716.5    | 202.6    | 106.6    |
| 1000.                     | 2106000  | 9500.    | 7200     | 2000.    | 1065.    |

### 3.2.4 Forward detectors and Trigger system

The forward detectors were designed for different functions. They are used to extend the measurement of the charged particles and photons at large values of rapidity, and to characterise the event in terms of the collision centrality. Centrality is a bit difficult to quantify, but is usually measured using some measure of the energy, or number of particles, produced at rapidities close to that of the centre of mass.

The name probably comes from the distance between the centres of the nuclei in the impact parameter plane (the more central the smaller the impact parameter). Since we cannot measure the impact parameter (a few fm) directly, instead we use correlated quantities, such as the transverse energy or the multiplicity. In ALICE we use the multiplicity.

Two detectors are especially designed to deliver fast trigger information of general interest namely the detector V0 triggering on centrality, and the detector T0 delivering fast information on multiplicity. The pulse height in each slab in V0 is proportional to the number of tracks going through it, so by converting and summing we can estimate the multiplicity from the pulse height information. We use the V0, which are not at mid-rapidity but slightly forward, because that way we do the main physics measurements based on different tracks, and avoid auto-correlations, which could be a problem in the case of (e.g.) jet production, where large numbers of particles are produced.

In addition more specialised detector systems can cause triggers on their specific process of interest: like the EMCAL, that will trigger on jets; PHOS on high  $p_t$  photons; the muon spectrometer triggers on muons; and the TRD offers the possibility to trigger on electrons. The trigger system is staged into three levels. The lowest level trigger L0 is delivered within  $1.2 \mu s$  of an interaction and registers if there was a collision and evaluates simple information like multiplicity, centrality or if there was a signal in one of the especially dedicated detectors as previously mentioned. The next higher trigger level L1 gives an accept or reject within  $6.5 \mu s$ . It allows time to do more complex analysis like electron identification with the TRD, coarse momentum determination (low/high  $P_T$ ) or topological cuts. The third trigger level

L2 prevents recording events with pile-up. As the interaction rate is predicted to be 8 kHz in Lead-Lead collisions there is a non-negligible probability that within the drift time of the TPC of  $92 \mu\text{s}$  a second collision might be recorded that would spoil the previous event. To ensure that only pure events are recorded the L2 rejects events where a subsequent collision caused signals in the detector within the drift time interval. The past future protection which counts the number of interactions in a given time interval is used for this purpose

## **T0 Detector**

T0 detector consist of two arrays of Cherenkov counter as shown in figure 3.3 with time resolution of 50 ps. It is the fast timing and trigger detector for the ALICE experiment at CERN. It gives a the trigger and timing signals, measures on-line vertex position and give rough centrality. Data from T0 are crucial not only for extraction of the precise interaction time but also for normalisation between proton-proton and heavy ion runs. Its aims include the supply of several signals to the ALICE trigger, to deliver an early ( prior to L0 trigger) wake-up to TRD, and also to give a precise start for the time-of-flight (TOF) particle identification.

The trigger functions requested from T0 are to measure the approximate vertex position, to give a rough estimate of event multiplicity and to also inform that at least one of the arms of the T0 detector has registered a valid pulse.

Given its location, the pseudo-rapidity range covered is  $2.9 < \eta < 3.3$  and  $-5 < \eta < -4.5$  . The measured multiplicity is analysed against 2 pre-set values

to generate one of the three possible trigger signals: T0(minimum bias), T0(semi-central), or T0(central) corresponding to low, intermediate, and high multiplicities. There are only two threshold values because the minimum bias signal is identical with T0-vertex. T0 vertex is a proposed trigger signal ( not yet implemented) which notes the relative timing between the hits in the two T0s (one on either side of the vertex point) and does not allow the difference to be too big. This amounts to demanding that the vertex must be inside a certain range in z, and so constrains the z co-ordinate for accepted vertices.

## V0 Detector

The V0 detector is a small angle detector consisting of two arrays of scintillator counters, called V0A and V0C, which are installed on either side of the ALICE interaction point as shown in figure 3.3. The V0C counter is located right upstream of the dimuon arm absorber and cover the spectrometer acceptance while the V0A counter is located at around 3.5 m away from the collision vertex, on the other side. The counters cover the pseudo-rapidity ranges of  $2.8 < \eta < 5.1$  (V0A) and  $-3.7 < \eta < -1.7$  (V0C).

It is designed to provide the minimum bias trigger and triggers on centrality <sup>2</sup> in Pb-Pb mode, multiplicity information and luminosity control. It also provides beam gas interaction identification. A "beam gas" interaction is one where one of the beams interacts with the residual gas in the beam pipe. They can occur

---

<sup>2</sup>The distance between the centres of the nuclei in the impact parameter plane (the more central the smaller the impact parameter).

anywhere, but are more likely to do so outside the zone between the two V0s than the one between them (more space). Let us imagine tracks coming from an upstream interaction outside the V0 area. The "normal" timing of the V0s is based on an interaction between them, and then a short flight for particles from the interaction point to each of the V0s. In the beam gas case, particles hit the nearer V0 BEFORE the expected time of the interaction (which is a known time based on the timing of the LHC bunches). The timing in the further V0 will look fairly similar to that from an ordinary interaction. It is these early hits in V0 which signal a beam gas interaction.

## Central Trigger Processor

The ALICE trigger system is situated in the experimental cavern and has a centralised layout: the Central Trigger Processor (CTP), the detector interface or Local Trigger Unit (LTU), and the Trigger Timing and Control partitions are all installed in adjacent racks. The CTP generates three levels of hierarchical hardware triggers : L0, L1 and L2. At any time, up to 24 detectors from the ALICE experiment can be dynamically partitioned into up to 6 independent clusters (group of read out detectors). The level of event pile up is controlled by the past-future Protection logic <sup>3</sup>. The LTU serves as a uniform interface between the CTP and the detector readout electronics. In the standalone mode of operation, the LTU fully emulates the CTP protocol.

---

<sup>3</sup>A procedure that selects events with a programmable time interval before and after the collision, during which there can be a number of pile-up interactions tolerated up to a programmable limit.

The Central Trigger Processor [80] is designed to combine and synchronise information from all triggering detectors and to send the correct sequences of the trigger signals to all the detectors, in order to make them read out correctly. It also co-ordinates calibration requests from the detectors and generates data summarising why a particular trigger has been taken. It is designed to operate in several modes with significantly different characteristics: in Pb-Pb mode, the interaction rate is 8 kHz, but, due to the high multiplicity, the event size is very large (up to 86 MB); while in the proton-proton mode, the event size is smaller (2.5 MB), but the interaction rate goes up to 200 kHz.

### **Trigger logic**

In all, there are 60 trigger inputs: 24 for those inputs with a latency of less than 800 ns (L0); 24 for those with a latency of up to  $6.1 \mu\text{s}$  (L1); 12 for those with a latency of up to about  $96 \mu\text{s}$  (L2). These can be used to activate up to 6 different detector groupings, called clusters, which can be made up from any arbitrary combination of detectors. The same detector can be included in more than one cluster. While taking data it is possible for the CTP to generate internal signals which are treated in the same way as detector inputs by the CTP logic. These are: two random inputs (RND1 and RND2) with a programmable mean rate, and two regular inputs (BC1 and BC2) with a programmable rate determined from the LHC clock by downscaling. Up to 50 different trigger definitions, called classes, can be run simultaneously. The parameters required to make up a trigger selection together define a trigger class. To specify a trigger class it is necessary to define the trigger logic condition at each trigger level, to associate the trigger cluster with the trigger class, and the

downscaling factors to be applied.

The data used for the analysis contains a sample of p-p collisions at a beam momentum of 3.5 TeV corresponding to LHC10b and LHC10c periods for a series of run from 114778 to 116572 and 118507 to 120069 respectively. The data was recorded in April 2010. In the LHC four proton bunches per beam were circulated, with two pairs of bunches crossing at the ALICE interaction region. The detector readout was triggered with signals from the two upstream beam pick-up counters and a minimum-bias interaction trigger requiring a signal in at least one of the SPD pixels or one of the VZERO counters [97]. These counters are placed around the beam pipe on either side of the interaction region and are known as VZERO-A and VZERO-C. A total of 78 million events are studied in this thesis. The integrated luminosity corresponding to the data set analyzed in this thesis is  $(1.25 \pm 0.09) \text{ nb}^{-1}$ , the details of which are found in chapter 5.

# Chapter 4

## Reconstruction and selection of $J/\Psi$ at ALICE

### 4.1 Introduction

One of the aims of the ALICE experiment is to measure the yield of  $J/\psi$ . To achieve this, it is necessary to reconstruct its decay products and to obtain a pure sample. In order to remove the background, a set of selection criteria is imposed, known as track quality cuts and selection cuts. These will be described and justified in this chapter.

## 4.2 ALICE Software Framework

Since the ALICE experiment is expected to take data for at least the next ten years, the accumulated raw data for a particular run have to be completely reconstructed before the next run in order not to generate a backlog of unprocessed raw data. The analysis framework includes generation and reconstruction. The software used for the ALICE offline is called ALIROOT and is based on the ROOT analysis framework.

ROOT [81] is an object oriented framework written in the C++ language. It consists of 650 classes, taken from C++ base classes. This structure is suited to manage the enormous amount of data from a high energy experiment as it provides the packages for event generation, detector simulation, data reconstruction and data analysis. As an extension to ROOT, ALIROOT [82] was developed to include and simulate the geometry of the ALICE detectors, and their response to the passage of particles. The scheme of ALIROOT is shown in figure 4.1. The module STEER provides the interface to detector specific code, to event generators, to Monte-Carlo simulators and to steering class for reconstruction. There are several event generators (like PYTHIA) and detector generators (like GEANT3) which will be described later in this chapter.

For proton-proton data the first reconstruction can be run on-line in parallel with the data taking. For lead-lead raw data, this is not possible due to the ten times higher data volume. For this reason the Grid computing concept has been adopted. The Grid is hierarchically subdivided into 3 levels of so-called Tier centres. A Tier level is defined by the type of the stored data. There are four different types of data:

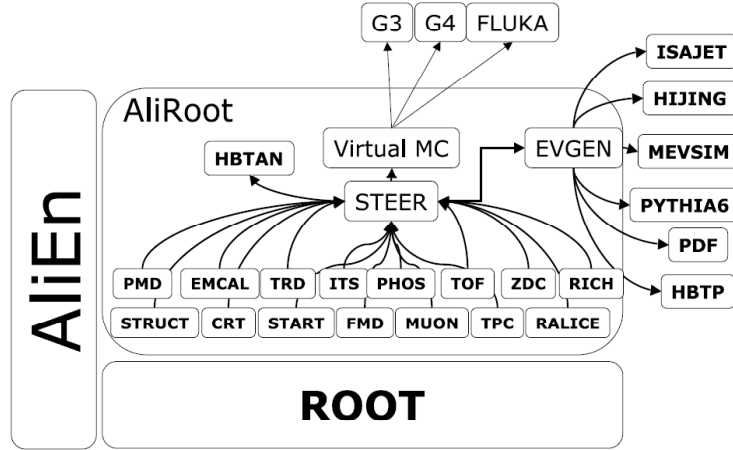


Figure 4.1: Schematic view of the ALIROOT framework.

- Raw Data: As recorded by the data acquisition.
- ESD (Event Summary Data): Reconstructed data; minimal cuts.
- AOD (Analysis Oriented Data): Extracted from the ESDs, only data relevant for a specific type of analysis are stored.
- TAG - Event tags for event selection

Grid computing is designed to handle the huge amounts of data as well as to give physicists access to it for further analysis. The raw data are kept in the Tier 0 centre, namely at CERN, where also parts or even all of it will be reconstructed for the first time. Parallel to this the raw data are distributed among the Tier 1 centres, usually one large computer centre per country. In the Tier 1 centres the raw data are reconstructed for at least a second time with improved calibrations. Due to the huge costs in terms of CPU power to reconstruct the raw data, this task is done centrally, and since it consumes the available computing resources during

one ALICE running period, more iterations on the reconstruction is carefully planned and are not repeated arbitrarily often on the full data set. In addition the Tier 0 centre is not foreseen to contribute significantly to the data analysis. The Tier 1 centres, apart from parts of the raw data, keep a subset of all ESDs; however via the Grid all ESDs are available for analysis. The Tier 2 centres do not contribute to the reconstruction of the raw data at all, and for this reason do not store the raw data. Instead the Tier 2 centres perform the necessary Monte-Carlo production needed for the data analysis. Each centre keeps a subset of all ESDs and AODs for data analysis. The next Tier levels are the Tier 3 and 4. Tier 3 centres are planned as medium sized clusters at laboratories or universities keeping only a small subset of the total amount of the data as a copy. Finally the desktop machine of a physicist doing analysis is regarded as Tier 4.

The AODs represent a more specific version of the ESDs. During the production of the ESDs any cuts or irreversible changes are avoided. The AODs are produced with respect to the requirements of a specific analysis and might for this reason, as an example, already include cuts on the quality of ESD tracks as well as particle identification. In addition, results of very CPU intensive algorithms like secondary vertex finding might be performed during the production of the AODs; in this way such expensive operations need to be performed only once. The analysis of data is performed within the framework of an **AliAnalysisTask**. The concept of an analysis task is that, since a lot of time is spent on reading the data from disks or tape, one should perform not only one specific analysis task within one analysis run, but many tasks, to make maximal use of the event currently stored in the memory. To perform an analysis on the complete data set one has to first develop a task derived from a prototype class. Different tasks, which may even depend on each

other, can then be organised in an analysis train. The input and output of this train is managed by the analysis manager. Each task residing in this train is then subsequently executed as soon as the data are available. This system ensures that a lot of tasks can run on the full data set, without too many files being queried at the same time.

For the studies presented on  $J/\psi$  production, an analysis train has been developed by the author. The train has been run on data sets of real data at  $\sqrt{s} = 7$  TeV (as described in later sections) and on three MC samples (as mentioned later) to evaluate the effect of the applied cuts with respect to signal as well as to possible background contributions. This analysis train was used on AliEn [83]. AliEn is a Grid framework built around existing Open Source components using a combination of Web Service and distributed agent models. It is being developed by the ALICE collaboration as a production environment for the simulation, reconstruction and analysis of physics data.

### 4.3 Event Generators

Multi particle production is an important feature of high-energy physics. It is here that the so-called event generators come into play. In an event generator, the aim is to use computers to generate events as detailed as those observed by a perfect detector. The output of the event generator is a set of events, with almost the same behaviour as real data. In generators, Monte-Carlo techniques are used to get all the desired probability distributions, thus ensuring randomness in final events. Event

generators are used for the following purposes:

- To get an idea of the kind of events one may expect or hope, and also at what rates.
- In the planning of a new detector, so that detector performance is optimised.
- To plan the analysis strategies that should be used on the real data, so that signal to background conditions are optimised
- To calculate the detector acceptance corrections that needs to be applied to raw data so that physics signals can be extracted. The detector simulation is tuned to reproduce the real data. The MC sample is used to perform correction to reproduce real data. For MC data to agree with the real data certain control regions are defined. Comparison is done within these controlled regions. If a agreement is reached, then MC can be used to correct the data.

The event generators are grouped in a module called EVGEN. This module includes a variety of generators which were developed outside the ALICE collaboration. As some of these were written in the FORTRAN language, they are linked to ALIROOT through wrapping classes. The main generators used for the hadron-hadron collisions are PYTHIA [84] and PHOJET [85]. The generators for heavy-ion collisions are HIJING [86], DPMJET (Dual Parton Model Jet [87]) and SFM (String Fusion Model Jet [88]). The generator used in the work presented here is PYTHIA for the p-p collisions, while HIJING is in generally used for Pb-Pb interactions. The PYTHIA program is a tool for the generation of high-energy collisions as accurately as possible, comprising a set of physics models for the evolution from a few-body hard process to a complex multi-hadronic final state.

## 4.4 Detector Simulations

The behaviour of the detector after particles are produced by the event generator, how they traverse the detector, spiral in magnetic fields, shower in calorimeters, or escape through cracks is simulated in programs such as GEANT3 [89] and FLUKA [90], written in FORTRAN. GEANT4 [91] is the evolution of GEANT3 towards C++ language. So far, GEANT3 has been used and FLUKA is thought to be what ALICE will use in the near future. These transport packages also include models describing all the possible interactions occurring between radiation and matter. The various sub-detectors provide independent modules with specific code for simulation and local reconstruction. The information that one gets from these local reconstructions are grouped into the global event reconstruction, which gives the track reconstruction, primary and secondary vertices and particle identification. The output of this simulation has exactly the same format as the real data recorded by the detector, and thus can be put through the same event reconstruction and physics analysis chain.

### Event simulation and reconstruction

Figure 4.2 shows a chain of event simulation and reconstruction. The left part is the simulation down to raw data, while the right part is the procedure which is used for the real data. The various steps corresponding to simulation and reconstruction are as following.

**Simulation:** In the collisions, the particles produced are generated with a generator code. The simulation packages help in transporting the final state particles through the detector, while taking into account all the processes occurring via the interac-

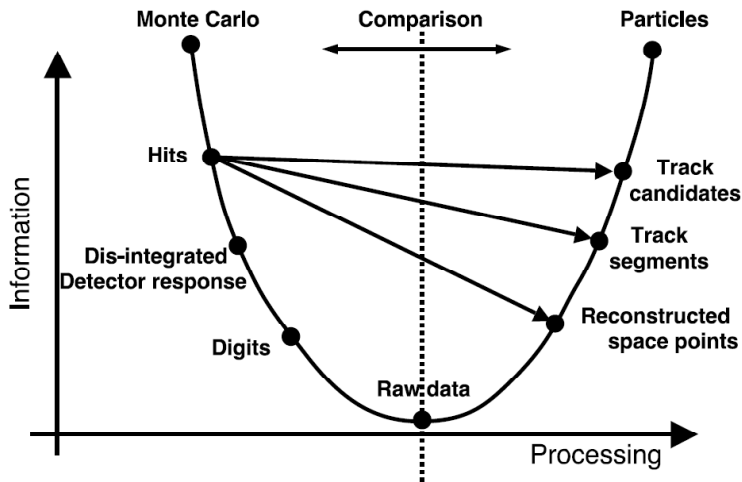


Figure 4.2: Data processing framework. [92]

tion of particles with detector materials. In these processes the energy deposited in the detector is calculated and is called hits. Hits represent the ideal response of the detector to the passage of particles. The next step is the transformation of hits into digits, which represents the real detector response and takes into account instrumental effects such as the physical noise due to the front end electronics which adds to the physical signal. After the transformation of hits into digits, the digits are transformed into the raw data format, which is identical to that coming from the data acquisition system during data taking.

**Reconstruction:** The reconstruction starts after the raw data have been created. A single signal is formed from the digits which are extracted from the raw signal and convoluted with physical and electronic contributions. The clusterisation process takes place, in which several digits are grouped together in order to find a cluster which represents the realistic signal given by a particle in the detector. The reconstructed point (called rec point) is found by calculating the centre of gravity of

the cluster. This rec point is a realistic estimate of the position where the particle crossed the sensitive area of the detector. The reconstruction points are then associated to tracks, which not only contain information on the kinematic variables but also the identity and the energy loss of the particles. In the ALICE experiment the reconstruction of tracks is based on the Kalman filter algorithm[93] which is widely used in high-energy physics experiments. In the Kalman filter procedure, a track is identified by a state vector of five parameters which define the track, and by its covariance matrix. Tracking starts from the track-seed performed considering all the pairs of points in the TPC outer-most pad row. A second seed finding is performed using another couple of pad rows. Then it proceeds with the Kalman filter through the whole TPC. If the procedure reaches the inner wall of the TPC it tries to find matching clusters within the ITS. Especially in a high multiplicity environment this may result in a large tree of possibilities which have to be analysed with respect to the highest probability. During this extrapolation, multiple scattering (by adding the corresponding matrix to the track covariance matrix [94]) and energy loss (by means of the Bethe-Bloch formula) are taken into account. Thus for all the clusters whose coordinates are inside suitable **windows**, a  $\chi^2$  - **increment** is calculated. The **windows** are estimated taking into account the cluster position precision and the uncertainty of the track position extracted from covariance matrix associated to the track state vector. The cluster with the minimum  $\chi^2$  is assigned to the track and state vector and its covariance matrix are updated according to the standard filtering procedure. Clusters with large  $\chi^2$  [95] are removed from the track. From the outer wall of the TPC the track is then propagated into the TRD and from there to TOF, HMPID, PHOS and EMCAL. At the last reconstruction step, the information relevant for particle identification is assigned to the track and the track is refitted towards the centre of the detector.

Thus the tracking procedure takes place in three steps [96]:

- the seeding of tracks,
- the reconstruction of tracks,
- a best fit of the track parameters.

The track reconstruction process allows one to determine the momentum of particles and their charge in space. Also, it is capable of precisely extrapolating the tracks to the detectors that provide the particle identification information such TOF, HMPID and PHOS. These are situated far away from the main interaction point.

## 4.5 Monte-Carlo Samples:

### Primary, Secondary and Minimum Bias Samples

Samples of  $2 \times 10^6$  primary  $J/\psi$ ,  $10^6$  secondary  $J/\psi$  and about  $10^6$  Minimum Bias proton-proton events were produced with PYTHIA 6.214 and analysed using AliEn. The analysis was performed using the MC data provided by the ALICE Particle Data Challenge production during 2010 for primary  $J/\psi$ , secondary and Minimum Bias data samples. Both primary and secondary  $J/\psi$  samples are not minimum bias i.e. there is

$$1 B \rightarrow J/\psi + X \tag{4.1}$$

$$1 J/\psi \rightarrow e^+e^- \quad (4.2)$$

per event. In the primary  $J/\psi$  MC sample of  $2 \times 10^6$  events, the signal is thus enhanced by:

$$1/(0.059 \times 0.14 \times 10^{-3}) = 1.21 \times 10^5 \quad (4.3)$$

where 0.059 corresponds to the branching ratio of  $J/\psi \rightarrow e^+e^-$  and  $0.14 \times 10^{-3}$  is the number of  $J/\psi$  per collision. This is equivalent to

$$(1.21 \times 10^5) \times 2 \times 10^6 = 2.42 \times 10^{11} \quad (4.4)$$

minimum bias events. In case of the secondary sample, the enhancement is

$$1/(0.01 \times 0.059 \times 0.0072) = 2.35 \times 10^5 \quad (4.5)$$

where 0.01 corresponds to the branching ratio of  $B \rightarrow J/\psi X$ , and 0.0072 corresponds to the number of  $b\bar{b}$  pairs per minimum bias collision. This means the secondary sample of  $10^6$  is equivalent to

$$(2.35 \times 10^5) \times 10^6 = 2.35 \times 10^{11} \quad (4.6)$$

minimum bias events.

## 4.6 Data Sample

The data used for the analysis contains a sample of p-p collisions at a beam momentum of 3.5 TeV corresponding to LHC10b and LHC10c periods for a series of run from 114778 to 116572 and 118507 to 120069 respectively. The data was recorded in April 2010. In the LHC four proton bunches per beam were circulated, with two pairs of bunches crossing at the ALICE interaction region. The detector read-out was triggered with signals from the two upstream beam pick-up counters and a minimum-bias interaction trigger requiring a signal in at least one of the SPD pixels or one of the VZERO counters [97]. These counters are placed around the beam pipe on either side of the interaction region and are known as VZERO-A and VZERO-C. The time resolution of this detector is better than 1 ns. Its response is recorded in a time window of  $\pm 25$  ns around the nominal beam crossing time. A total of 78 million events are studied in this thesis.

## 4.7 Cuts

The basic idea of the analysis is that for each event all electron and positron tracks are combined with each other and the invariant mass is calculated. This is done by running the AnalysisTask on two AODs simultaneously. One is known as general AOD, which contains information about the tracks; the other is called friend AOD, which contains information about the candidates. In order to obtain an estimate of the uncorrelated background one uses mass sideband fitting and mixing of like sign pairs. The major background contributions are expected from semi-leptonic

decays of charm and beauty-mesons and from misidentified pions and protons. There are various possible cuts that can be applied to increase the performance of the measurement and hence increase the signal over background ratio. The following cuts will be discussed in detail:

- cuts on track quality
  
- selection cuts one can apply to improve the signal to background ratio

#### 4.7.1 Track quality cuts

The standard track quality cuts for 2010 are used while forming AODs from the ESDs:

**Number of TPC Clusters( $N_{cls}$ ):** A cluster denotes a combination of TPC channels used for a given track reconstruction. For the presented studies, in the case of TPC we demand  $N_{cls} > 70$  to ensure good quality tracks while rejecting background. Figure 4.3 shows the distribution of the number of TPC clusters for the MC primary and secondary  $J/\psi$ , MC minimum bias and real data respectively. Real data is data sample mentioned in section 4.6.

$\chi^2/N_{cls}$ : In order to measure the quality of the fit to the track, the  $\chi^2$  [95] of each fit is stored. For a good fit the quantity  $\chi^2/N_{cls}$  should be close to 1. A cut of  $\chi^2/N_{cls} < 3.5$  is used for this analysis.

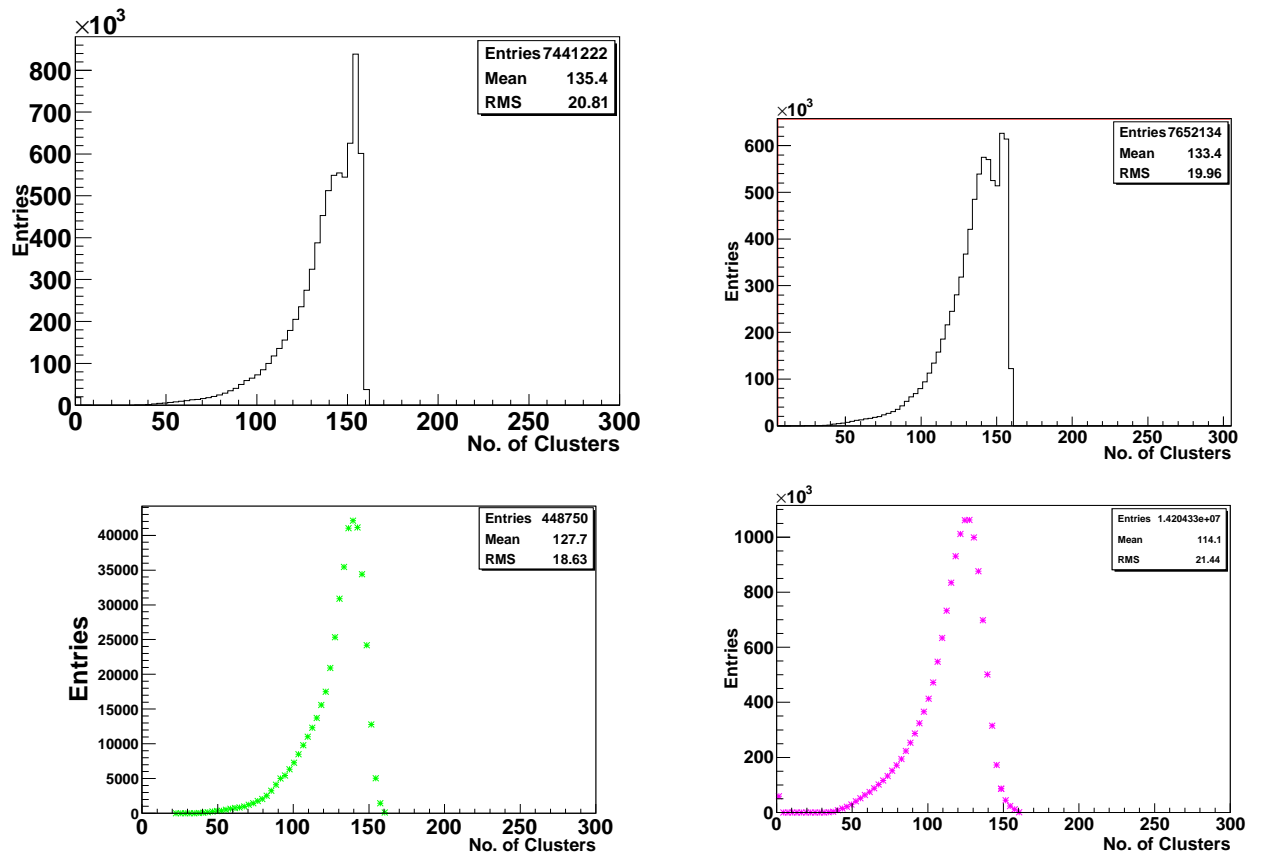


Figure 4.3: Top left: Distribution of Number of TPC Clusters in case of Primary MC  $J/\psi$ , Top right: Secondary MC  $J/\psi$ , Bottom left: Minimum Bias MC Sample, Bottom right: real data.

**TPC and the ITS Refit:** For every track a status word is stored. This consists of 32 bits, each bit indicating whether a certain criterion is fulfilled for this track or not. It is stored whether a certain track is successfully propagated to inner TPC wall (TPCin), then passed over to ITS (ITSin), fitted back out (ITSout, TPCout), propagated and tracked through the TRD (TRDout) and finally if the refit through all detectors is successful (TRDrefit, TPCrefit, ITSrefit). Only tracks which pass TPC and ITS refit are selected.

**KinkDaughters:** Apart from the parameters discussed above, originating from the basic reconstruction, another parameter which is of great importance is used: **the kink index**. The algorithm to find kinks was introduced to detect Kaon decays such as  $K^+ \rightarrow \mu^+ \nu$ , where only the muon is measured, but since the neutrino carries momentum and is not measured, the whole process appears as a positively charged track with a kink at the point of the Kaon decay. Although this algorithm was designed for these Kaon decays it also finds a lot of kinks for other tracks, which basically leads to a duplication of the corresponding track. Whether a track was reconstructed as a mother (decaying particle) or daughter (produced particle) is indicated via the kink index. Since double counting of tracks should be avoided, all kink daughter particles are excluded from further analysis. Another kinks are the particles such as pions produced or scattered during the interaction in the detector.

**MaxCovDiagonalElements:**

This represents the maximum value of the covariance matrix diagonal elements. The  $\sigma^2$  constraints correspond to the error limits on track values that the tracking detector can measure, namely the  $x$  and  $y$  coordinates of the cluster hits on the

readout pads of the TPC, the azimuthal and polar angle of the track, and  $P_t^{-1}$ . The diagonal elements are  $\sigma_x^2$ ,  $\sigma_y^2$ ,  $\sigma_{\sin\phi}^2$ ,  $\sigma_{\sin\theta}^2$ ,  $\sigma_{1/P_t}^2$ , where  $P_t$  is the track transverse momentum. The  $\sigma_x^2$  and  $\sigma_y^2$  are the mean square deviation of the scattered track incidence points about the unscattered one. The values corresponding to these diagonal elements are  $\sigma_x^2 < 2 \text{ cm}^2$ ,  $\sigma_y^2 < 2 \text{ cm}^2$ ,  $\sigma_{\sin\phi}^2 < 0.5$ ,  $\sigma_{\sin\theta}^2 < 0.5$ ,  $\sigma_{1/P_t}^2 < 2 \text{ (GeV/c)}^{-2}$  respectively and are related to track momentum errors. The track cuts select good quality tracks suppressing the background from inefficient reconstruction.

### 4.7.2 Kinematic cuts

The cuts in the previous section are made at track level and they select only tracks with reasonable quality. The remaining cuts, since they reflect more on the kinematics of the  $J/\psi$  and its decay products, are called kinematic cuts, and will be discussed giving the distribution in each of the three MC samples and data sample. The various parameters studied are:

- Distance of Closest Approach (DCA) of  $J/\psi$  candidate tracks
- $\text{Cos}\theta^*$  angle between negative track and  $J/\psi$  flight line in  $j/\psi$  rest frame
- $P_t$  transverse momentum of positive or negative track

In the first subsection, a comparison of the distributions of above mentioned parameters for candidates in primary, secondary, minimum bias and real data samples are shown. To observe the effect of these cuts on the signal, a study on Monte-

Carlo distributions with ideal particle identification using monte-carlo information is carried out and discussed in the next subsection.

**Distance of Closest Approach** The distance of closest approach (DCA) denotes the closest distance between the two tracks of the electron pair. The distribution for DCA for all the electrons coming from primary  $J/\psi$  and also for electron positron pairs originating from the decay of the secondary  $J/\psi$  sample, is shown in figure 4.4 (top left and right respectively). The distributions for electron positron pairs from a minimum bias Monte-Carlo sample and real data are shown in figure 4.4 (bottom left and right respectively).

**Cos $\theta^*$ :**  $\theta^*$  is defined as the angle between negative track momentum and  $J/\psi$  flight line in the  $J/\psi$  rest frame. The distributions for the primary and secondary  $J/\psi$  sample are shown in figures 4.5(top left and right respectively). The distributions in the case of a minimum bias Monte-Carlo sample and from real data are given in figure 4.5 (bottom left and right respectively). The  $\cos \theta^*$  of the background is more populated at values  $\pm 1$ . As there is no significant difference between the minimum bias MC sample and real data as seen in figure 4.5,  $\cos \theta^*$  is not applied in the final cuts.

**Transverse Momentum  $P_t$ :** Another cut used in reducing the amount of background is the  $P_t$  of the two tracks. We denote the value of this cut as  $PCUT_t$ . The range of  $PCUT_t$  from 1 GeV/c to 5 GeV/c is investigated. The implications of this cut are shown later in this chapter. The  $P_t$  distributions of positive tracks in case of the primary and secondary  $J/\psi$  samples are shown in figure 4.6 (top left and right respectively). For the minimum bias MC sample and real data they are shown in

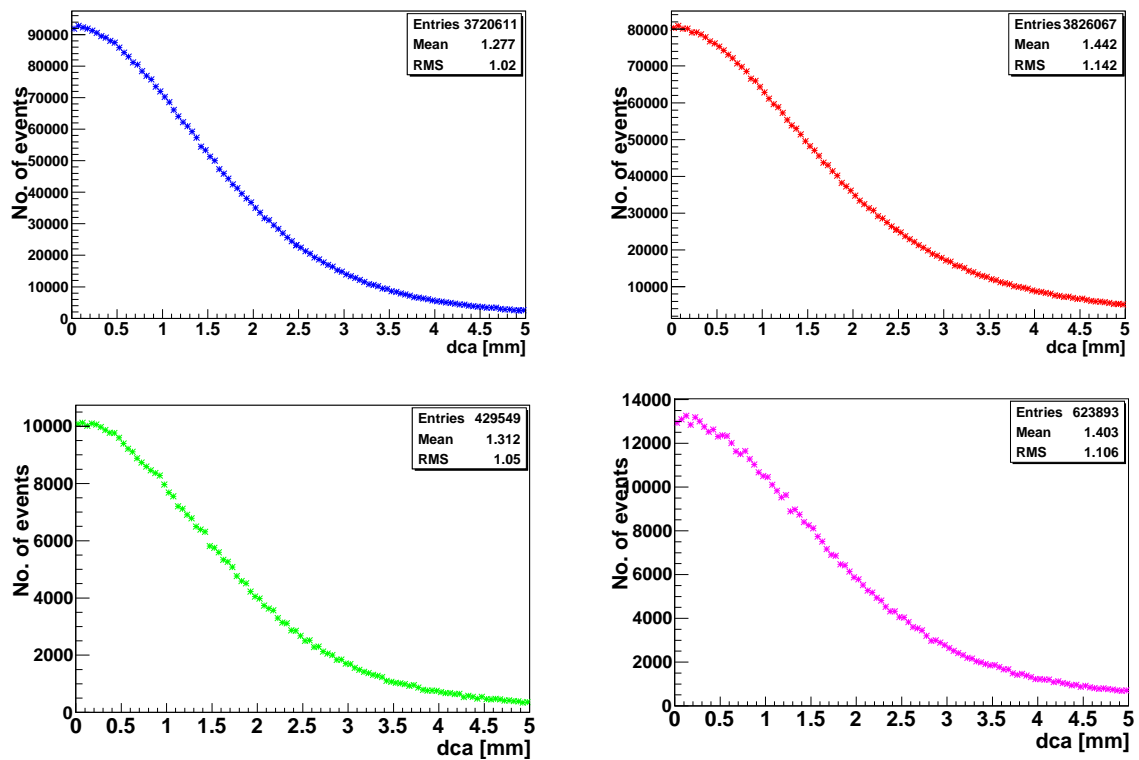


Figure 4.4: DCA distribution of the two decay tracks in case of Top left: Primary, Top right: Secondary  $J/\psi$  MC Sample, Bottom left: Minimum Bias MC sample and Bottom right: real data sample. These distributions includes all type of particles.

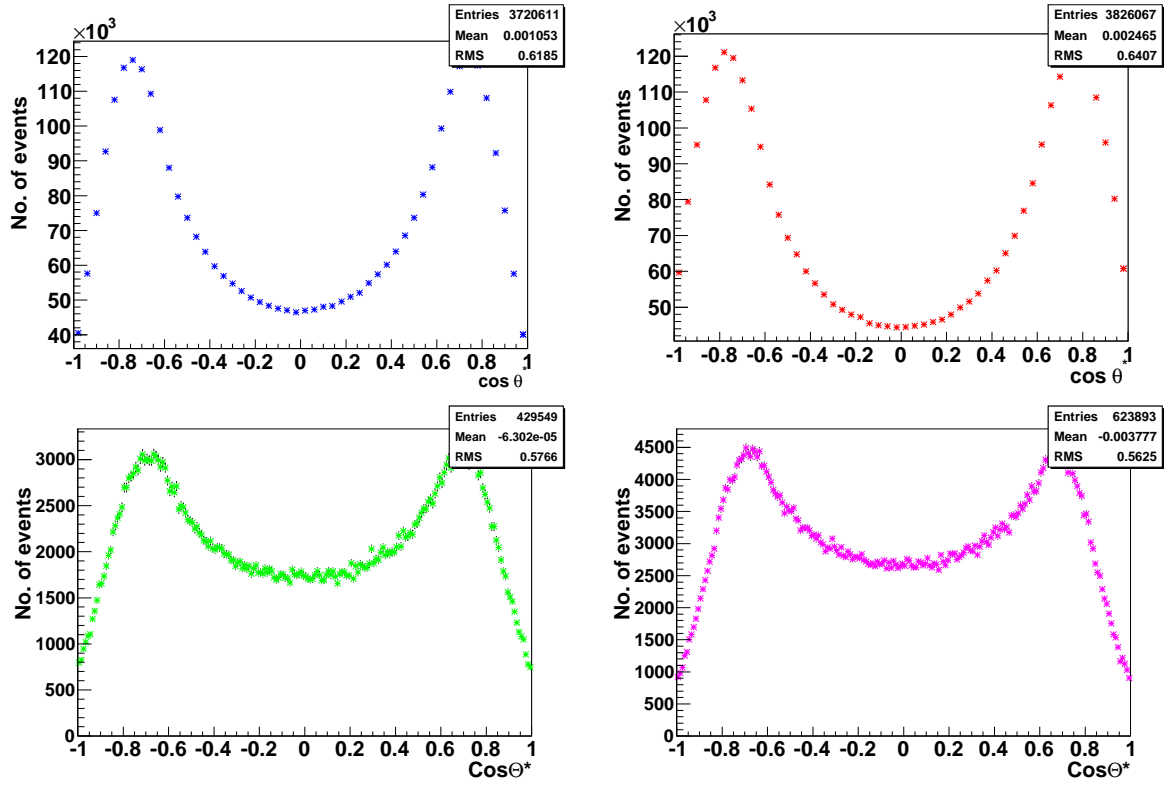


Figure 4.5:  $\cos \theta^*$  distribution in case of Top left: Primary  $J/\psi$  MC Sample, Top right: Secondary  $J/\psi$  MC Sample, Bottom left: Minimum Bias MC and Bottom right: data sample. These distributions includes all type of particles.

figure 4.6 (bottom left and right respectively). The  $P_t$  distributions in the case of negative tracks are compatible with those for the positive tracks.

### 4.7.3 True PID distributions and Summary of the cuts

The effect of cuts on the  $J/\psi$  signal can be studied using so-called true PID distributions. In the MC sample a flag is available for each track, to indicate its true identity. Therefore in order to select only those tracks which belong to generated  $J/\psi$  we can use the **true electron PID** available in MC. Then the tuning of all the above mentioned cuts is done using the true PID. Figures 4.7 and 4.8 show the distribution of DCA,  $\cos \theta^*$ ,  $P_t$  for the cases of primary and secondary  $J/\psi$  MC sample with true electron identification. The lines show the position of the cuts.

Thus the cuts applied on the data are summarised below:

1.  $N_{cls} > 70$  ensures good quality tracks while rejecting the background.
2. ITS and TPC refit improving the quality of tracks.
3. Rejecting Kink daughters to avoid duplication of tracks.
4.  $\chi^2/N_{cls} < 3.5$  to measure the quality of the fit to the tracks.
5. DCA of  $J/\psi$  candidate pair  $< 0.5$  cm. This have been studied.
6. The positive and negative tracks transverse momenta  $P_t > 1.3$  GeV/c ( $PCUT_t = 1.3$  GeV/c). This have been studied.

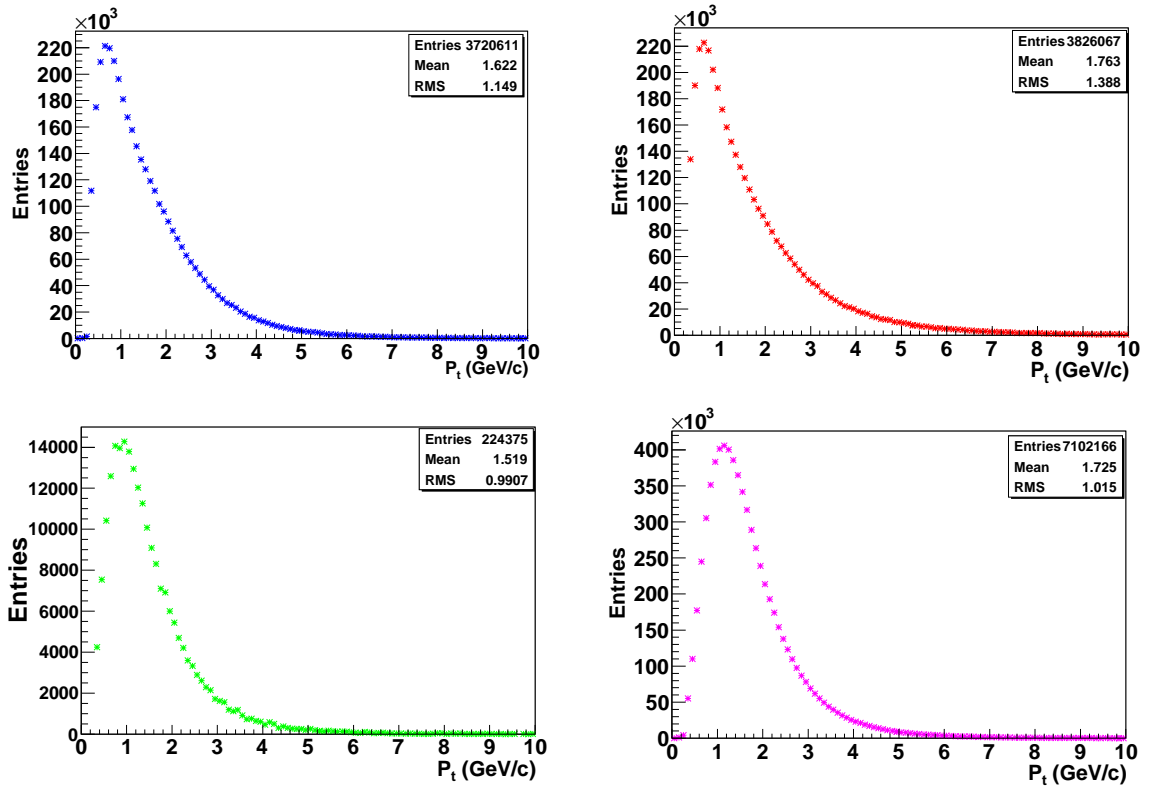


Figure 4.6: Top left and right is the Transverse Momentum of positive tracks distribution in case of Primary and Secondary  $J/\psi$  MC Sample. Bottom left and right is the Transverse Momentum of positive tracks distribution in case of Minimum Bias MC and data sample. These distributions includes all type of particles.

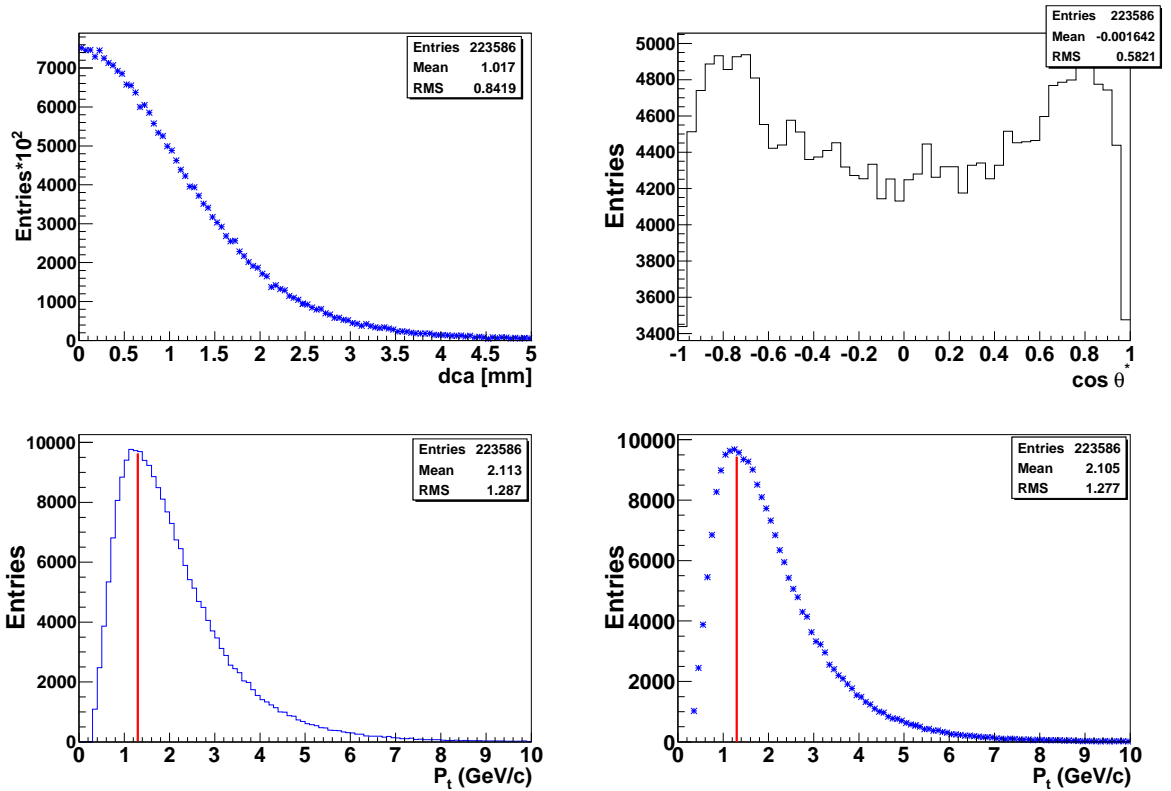


Figure 4.7: All the plots are with true electron identification in case of primary  $J/\psi$  MC sample. Top left and right is the DCA and  $\cos \theta^*$  distribution respectively. Bottom left and right are the  $P_t$  distributions for positive and negative tracks respectively. The red line represents where a cut has been made.

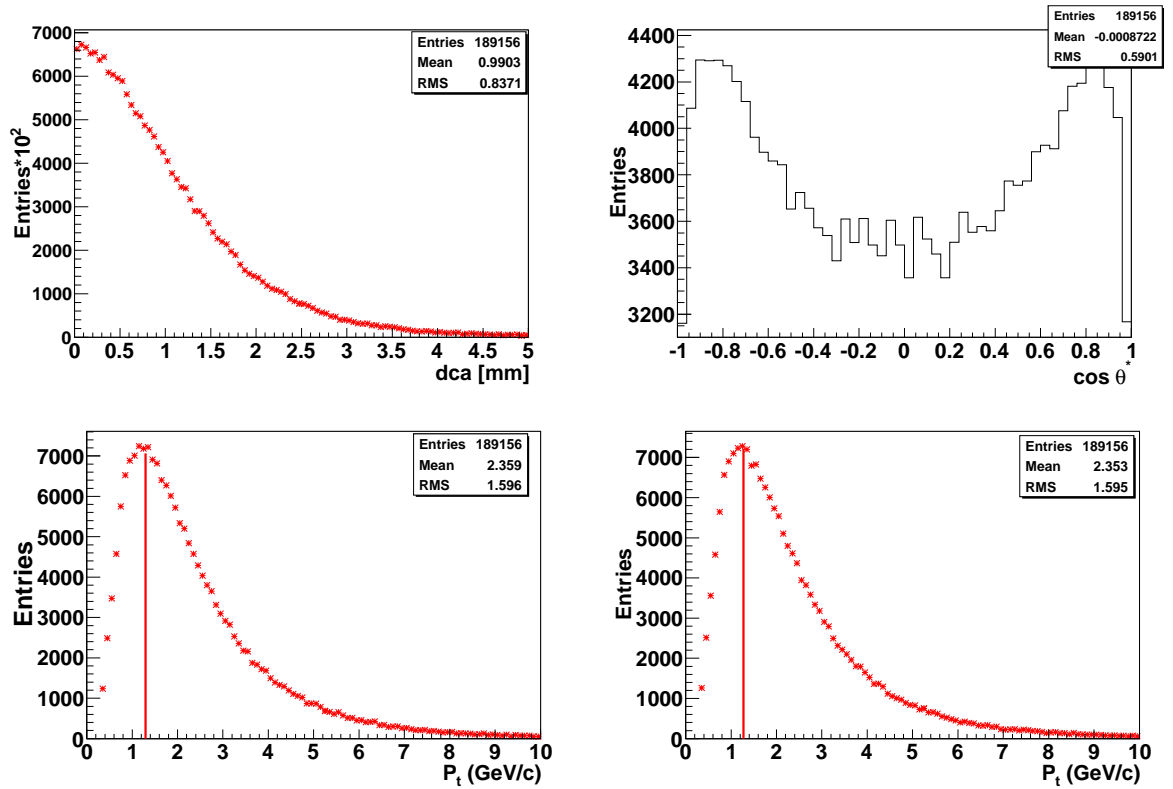


Figure 4.8: All the plots are with true electron identification in case of secondary  $J/\psi$  MC sample. Top left and right is the DCA and  $\cos \theta^*$  distribution respectively. Bottom left and right is the  $P_t$  distributions for positive and negative tracks respectively. The red line represents where a cut has been made.

7. A hit in at least one of the two innermost layers of the ITS to reduce the contribution of electrons from  $\gamma$  conversions
8.  $\delta M = |M_{measured} - M_{PDG}| < 1.2 \text{ GeV}/c^2$  where  $M_{measured}$  is the measured  $J/\psi$  mass value and  $M_{PDG}$  is the value from the Particle Data Group(PDG) [98]. The interval has been chosen to include the  $J/\psi$  peak and enough background to be able to perform a fit to the side-bands.

## 4.8 Particle identification using TPC $dE/dx$

Since true particle identification cannot be used and also since the combined PID technique has not yet been tuned for the real data and the TRD was not complete at that point, particle identification is done using uniquely  $dE/dx$  values from the TPC detector. The efficiency of the cut on energy loss  $dE/dx$  is estimated from data.

Charged particles, while traversing the TPC gas volume, interact with the gas atoms and lose energy by ionising electrons out of the gas atoms. This ionising energy loss per unit length, called the  $dE/dx$ , is a function of the magnitude of the particle velocity. This property is used for particle identification. The dependence of the specific energy loss on the particle momentum is shown in figure 4.9 and is almost constant in the momentum range 1-6 GeV/c. The energy loss of the charged particles is described by the Bethe-Bloch [99] formula, where low velocity particles lose a large amount of energy. With increasing momentum the energy loss approaches a minimum, e.g. for pions at around 0.6 GeV/c. For electrons

due to their small mass the minimum is outside the momentum range of the TPC and their  $dE/dx$  is constant for momenta larger than 200 MeV/c. However kaons with momenta around 600 MeV/c and protons with momenta around 1 GeV/c lose the same amount of energy in TPC as electrons. Applying a cut on the different particle bands on the TPC signal  $> 65$  (arb. units see in figure (4.9)) can help in removing the background. Thus a cut on TPC  $dE/dx$  is used to improve the signal to background ratio. While a clear band for electrons is present in the primary and secondary  $J/\psi$  MC sample, a much less pronounced contribution is visible in the MC minimum bias. This is because electron fraction in  $J/\psi$  samples is enhanced (see discussion in section 4.5) and so background pion tracks are dominant in MB sample. It is evident from figure 4.9 that the TPC  $dE/dx$  distributions in data and in Monte Carlo minimum bias are different because the Monte-Carlo code for PID has not been yet been tuned fully for real data. For this reason the efficiency of TPC  $dE/dx$  cut is estimated using only real data. For the explanation of the different bands, see figure 4.9 top left. In figure 4.9 bottom right, a band due to deuteron is also visible.

The Bethe-Bloch formula [100] predicts the energy loss of charged particles in a material. At low momentum, ionisation energy loss is approximately inversely proportional to the square of the particle velocity. From the measured energy loss and particle momentum, the particle type can be determined by comparing the measurement against the Bethe-Bloch expectations. Figure 4.10 (left) and 4.11 (left) show the distribution of energy loss ( $dE/dx$ ) as a function of particle momentum  $p$  in the case of real data and Monte-Carlo primary  $J/\psi$  samples. Different bands correspond to different particles. These particles are separated at low  $p$  as seen in figure 4.11 (left). As one proceeds towards higher  $p$ , they all converge together.

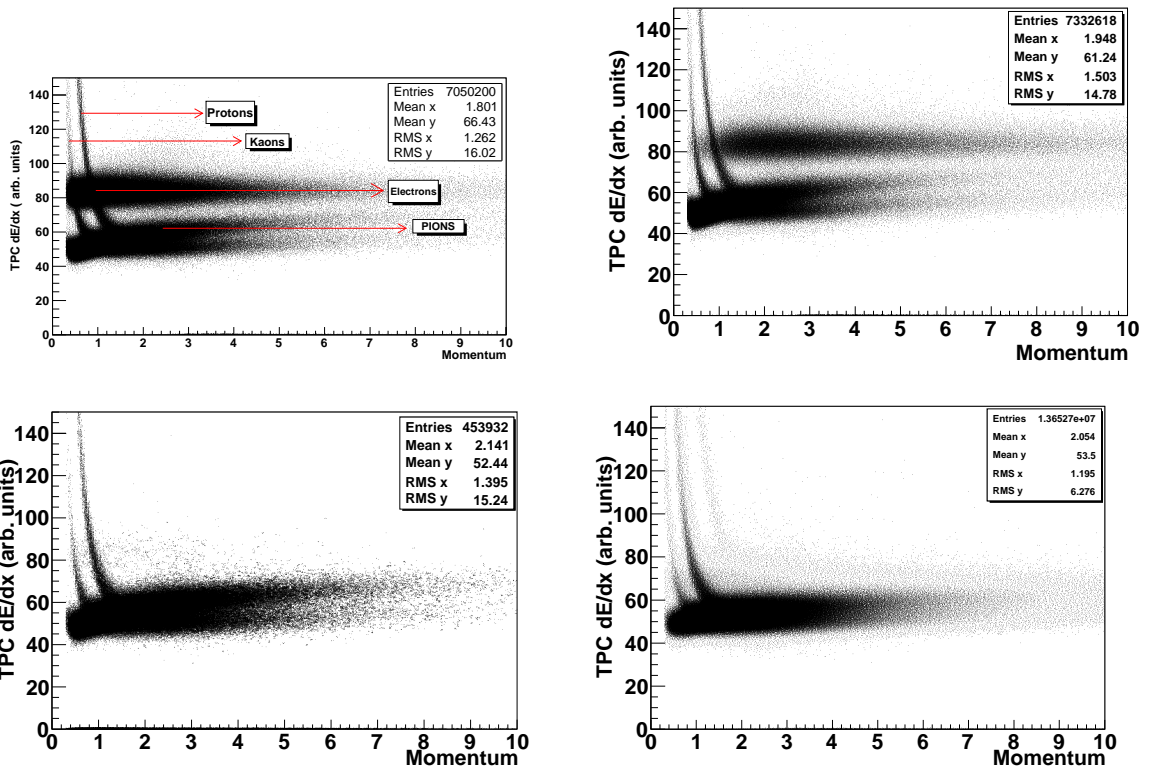


Figure 4.9: Top left and right is the TPC  $dE/dx$  (arb. units) distribution in case of Primary and Secondary  $J/\psi$  MC Sample. Bottom left and right is the TPC  $dE/dx$  (arb. units) distribution in case of Minimum Bias MC and data Sample. In all the plots momentum is measured in GeV/c. Deuteron band is visible in data sample.

Particles can be distinguished by a fitting procedure which allows us to disentangle the overlapped distributions into several components. This technique was also used by the STAR [3] experiment. Since, for a fixed particle type, the  $dE/dx$  distribution is not a Gaussian [101], a new variable called  $z$  is used, whose distribution in momentum bins is close to a Gaussian as seen in previous experiment [3]. The variable  $z$  is defined as:

$$z_i = \ln\left(\frac{dE/dx}{(dE/dx)_i^{BB}}\right) \quad (4.7)$$

where  $(dE/dx)$  is the measured energy loss,  $(dE/dx)_i^{BB}$  is the Bethe-Bloch value of  $dE/dx$  for a given particle type  $i$ , and  $i$  for the present case is the electron. For this study  $(dE/dx)_i^{BB}$  is defined as

$$(dE/dx)_i^{BB} = A_i\left(1 + \frac{m_i^2}{p^2}\right) \quad (4.8)$$

where  $m_i$  is the particle rest mass and  $p$  is the particle momentum magnitude.  $A_i$  is a normalisation constant determined from the data.  $A$  is chosen in such a way that the average expected value of  $z$  for electrons is 0. Figures (4.10 (right) and 4.11 (right)) show the distribution of  $z$  versus momentum for real data and primary MC  $J/\psi$  sample respectively.

The electron energy loss, see figure 4.11 (left), does not depend on momentum in the range  $0.2 < p < 6$  GeV/c; therefore in this range the electron PID efficiency can be estimated as one number independent of momentum. As the  $J/\psi$  signal selection uses a cut on transverse momentum of the  $J/\psi$   $P_T > 1$  GeV/c or higher, we apply the same cut on PID spectra as plotted in figures 4.12 (left) and 4.13

(left) for Monte-Carlo and data samples. A simultaneous Gaussian fit to electron and hadron signals is used to estimate the composition of the sample and therefore electron PID efficiency. The method is tested first on the Monte-Carlo sample and then applied to data.

The distributions of electron and hadron signals for  $p > 1$  GeV/c for the MC primary sample are shown in figure 4.12 (right). In this case hadrons and electrons are well separated. The curve is well described using one Gaussian for all hadrons and another for electrons. The fit results are shown in figure 4.12 (right). The fraction of electrons above the  $z_{cut}$  is estimated as

$$f = \int_{z_{cut}}^{\infty} \text{Gauss}_{electron}(z) dz. \quad (4.9)$$

where  $\text{Gauss}_{electron}$  is the Gaussian probability density function fitted to electron curve.

A check of the Gaussian fit can be done by retrieving results using true electron identification, i.e. PDG identification available in Monte-Carlo. For this purpose, a Monte-Carlo sample of 62198 primary J/ $\psi$  was studied. Firstly, for  $z_{cut} = 0.2$  and the formula (4.9),  $f = 0.342 \pm 0.007$  is derived. Counting the number of true electrons in MC gives

$$f = 1 - 3240/4940 = 0.344 \pm 0.011 \quad (4.10)$$

which is in agreement with the fitting procedure.

A TPC dE/dx cut above 65 is equivalent to  $z_{cut} = \log(65/70) = -0.074$ , where

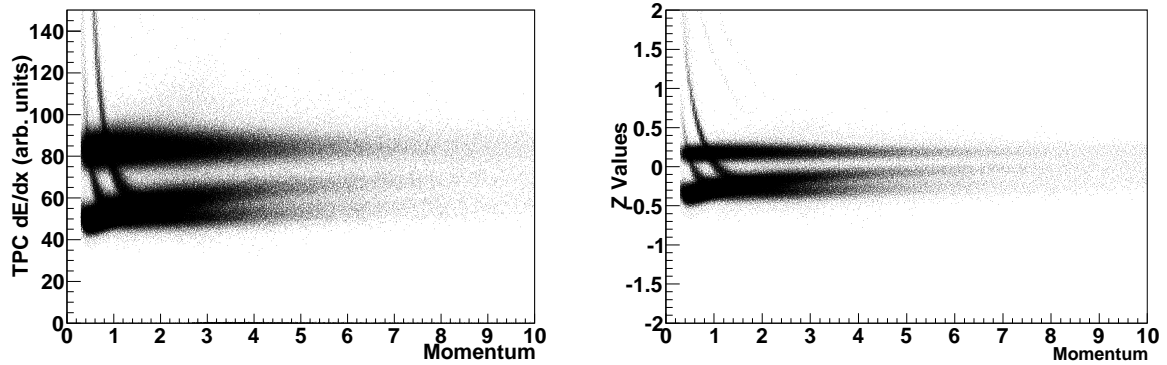


Figure 4.10: Left: Ionisation loss ( $dE/dx$ ) of various particles as a function of momentum measured in  $\text{GeV}/c$  in MC Primary  $J/\psi$  sample; Right:  $z$  variable for electron in MC Primary  $J/\psi$  sample as a function of momentum measured in  $\text{GeV}/c$ .

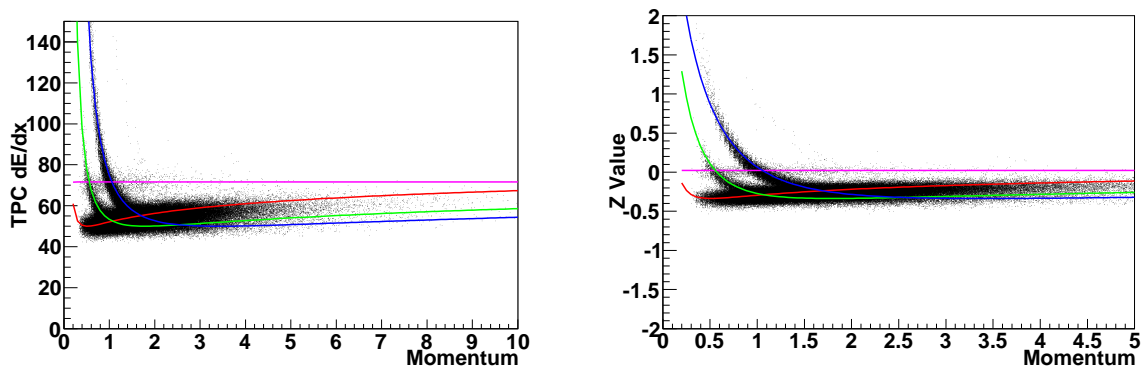


Figure 4.11: Left: Ionisation loss ( $dE/dx$ ) of various particles as a function of momentum measured in  $\text{GeV}/c$  in data taken with 7 TeV pp collisions; Right:  $z$  variable for electron in data taken with 7 TeV pp collisions as a function of momentum measured in  $\text{GeV}/c$ . In both the figures red corresponds to pions, green corresponds to kaons, blue corresponds to protons and pink to electrons.

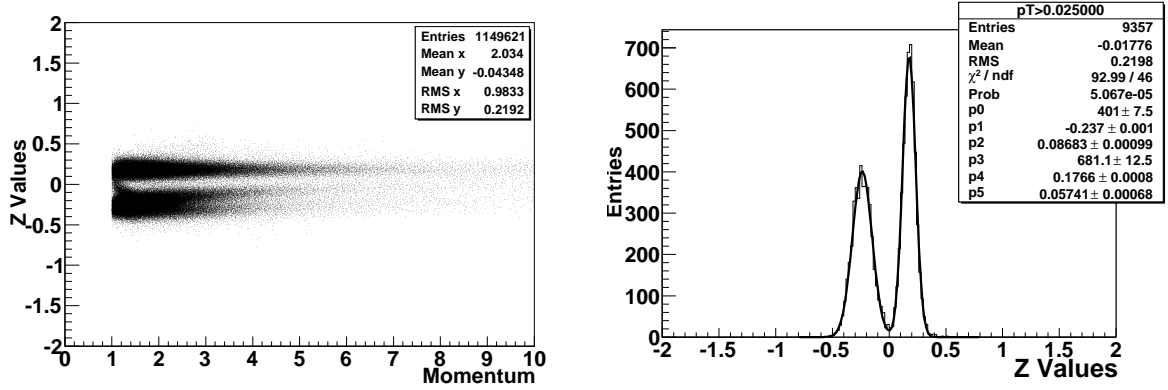


Figure 4.12: Monte-Carlo Primary  $J/\psi$  sample: Left:  $z$  variable for electrons with  $p > 1 \text{ GeV}/c$  ; Right: fitted  $z$  variable with two Gaussians. The peak at  $z > 0$  corresponds to electrons which are offset as normalisation is tuned to real data. The peak at  $z < 0$  corresponds to superposition of  $\pi$ , K, and p signals.

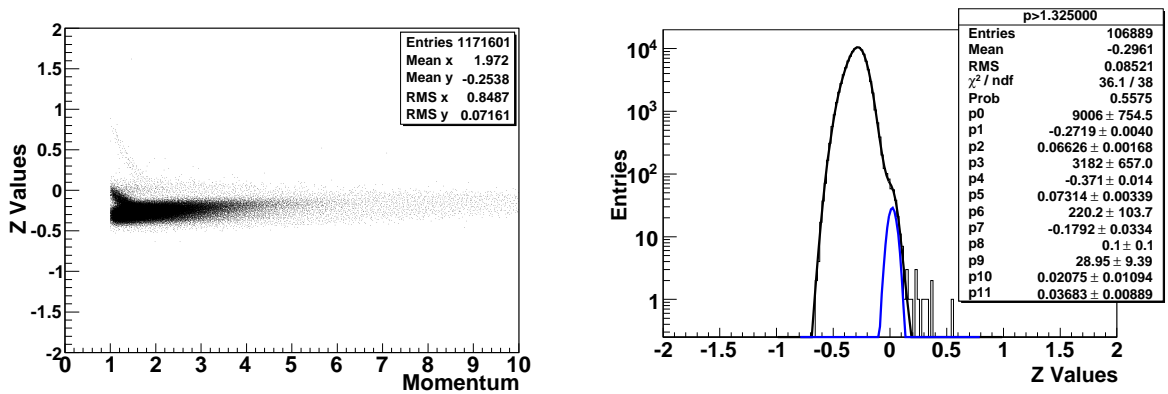


Figure 4.13: Data sample: Left:  $z$  variable for electrons with  $p > 1 \text{ GeV}/c$ ; Right: fitted  $z$  variable with four Gaussians at  $p > 1 \text{ GeV}/c$ . The black curve correspond to the sum of four Gaussians and blue corresponds to the electron signal. Deuteron band is visible in left plot.

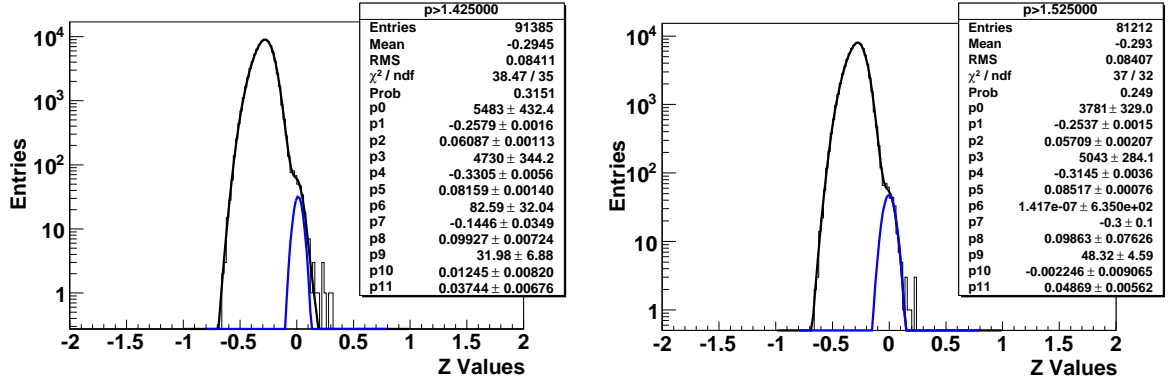


Figure 4.14: Data sample: Left: fitted  $z$  variable with four Gaussian at  $p > 1.425$  GeV/c; Right: fitted  $z$  variable with four Gaussian at  $p > 1.525$  GeV/c. The black curve correspond to the sum of four Gaussians and blue corresponds to electron signal.

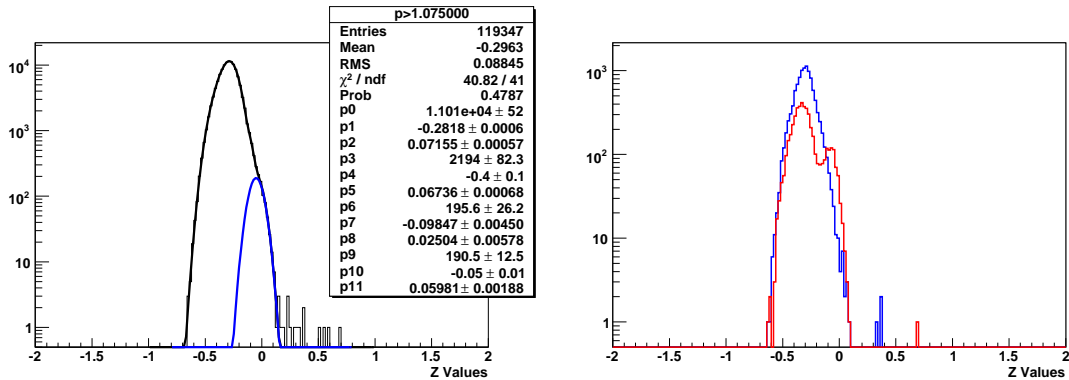


Figure 4.15: Data sample: Left: Fitted  $z$  variable with four Gaussian at  $p > 1.075$  GeV/c. The black curve correspond to the sum of four Gaussians and blue corresponds to electron signal; Right: Superposition of two momentum slices: Red corresponds to  $1.075 < p < 1.075 + 0.05$  GeV/c, blue to  $1.375 < p < 1.375 + 0.05$  GeV/c. In the red curve a proton contamination is visible at zero and disappears in the blue curve.

70 is the normalisation constant from the data, and the momentum dependence of  $z$  in formula (4.7) is neglected due to the small electron mass. Using this  $z$ -cut and the Gaussian curve from figure 4.12 (right), the estimated PID efficiency for electrons is  $f = 1 \pm 0.02$ . Information from the true electrons gives a second estimate for the efficiency. For electrons with  $p_T > 1 \text{ GeV}/c$ :

$$f = 1 - 2/4940 = 0.9996 \pm 0.0003 \quad (4.11)$$

where 2 is the number of electrons that are lost and 4940 is the number of entries in the same plot when considering only true electrons.

The distribution for electron and hadron signals for the data sample is shown in figure 4.13. In this case the particles are not well separated due to the incomplete TPC Calibration. Four Gaussians, one each for pions, kaons, protons and electrons, are used in the fit.

Figure 4.13 and 4.15 demonstrates the dependence of proton contamination of electron signal on the lepton momentum. The superposition of fitted curves to different  $p$  are shown on the figure 4.15 (right). The red Gaussian corresponds to  $1.075 < p < 1.075 + 0.05 \text{ GeV}/c$ , the blue one corresponds to  $1.375 < p < 1.375 + 0.05 \text{ GeV}/c$ . As observed, there is a small proton peak around 0 in case of  $1.075 < p < 1.075 + 0.05 \text{ GeV}/c$  and this peak disappears for the higher  $p$  values.

To estimate the systematic uncertainty the electron PID efficiency is calculated in 3 momentum regions:  $p > 1.325 \text{ GeV}/c$ ,  $p > 1.425 \text{ GeV}/c$ ,  $p > 1.525 \text{ GeV}/c$ . The fitted parameters are as shown in figures 4.13 (right), 4.14 (left), 4.14 (right). The fraction of electrons above the  $z_{cut} = \log(65/70) = -0.074$  is estimated following (4.9). The three momentum ranges correspond to efficiencies as listed in table 4.1.

All the values are consistent.

Table 4.1: Values of efficiencies for different momentum ranges

| $P_t(\text{GeV}/c)$ | Efficiencies    |
|---------------------|-----------------|
| 1.325               | $0.95 \pm 0.05$ |
| 1.425               | $0.99 \pm 0.05$ |
| 1.525               | $0.93 \pm 0.05$ |

The final efficiency is thus taken as the value closest to  $P_t > 1.325$  GeV/c and the spread in three different momentum ranges gives the estimate of the systematic error. The statistical error on efficiency is calculated by propagating the fit parameter errors – the Gaussian mean and width, using the numerical derivation of equation (4.9) – and is estimated to be 5%. This is only partial investigation of systematics. For example the contribution from PID calibration and the shape of various PID curves has not been investigated here. The ALICE paper [105] follows a more sophisticated method of PID which leads to a stronger background reduction. However this also leads to systematics of 10%, being a dominant one.

The resulting efficiency is:

$$f = 0.95 \pm 0.05(\text{stat}) \pm 0.03(\text{sys})$$

## 4.9 Signal extraction

The  $J/\psi$  candidate pair distributions passing the cuts described in section 4.7 (i.e. no pid cut) step by step is shown in figures 4.16, 4.17, 4.18 for the cases of the

primary, secondary and minimum bias  $J/\psi$  MC sample respectively. The pid cut is studied in section 4.8 would be applied only to data itself. Apart from the minimum bias sample which is purely background a peak is found at a mass of  $3.1 \text{ GeV}/c^2$ , which corresponds to the  $J/\psi$  mass. The mass distributions for the primary and secondary  $J/\psi$  MC sample in the case of true electrons are shown in figure 4.16 and 4.17 (bottom right) respectively. The Crystal-Ball function parameters obtained from fit to Monte-Carlo sample (see figure 4.16) are tabulated in table 4.2. The parameters are fixed to values obtained from fit performed to data. These values are the starting point for the fit performed to data. The fit converge to values close to the starting point. An estimate of the signal to background ratio in each of these cases is tabulated in tables 4.3 and 4.4 and is discussed later in this chapter. Since signal to background is very sensitive to the  $P_t$  cut as it suppresses proton contamination, several  $P_t$  cuts on the real data are examined later in the chapter.

## 4.10 Fitting the mass plot

To fit invariant mass distribution of  $J/\psi$  candidates, a Crystal Ball function  $G_{CBM}$  is used while for the background polynomial function  $P(M_{ee})$  is used. In the case of the Monte-Carlo samples the background is fitted using a second order polynomial while in the case of real data higher orders are used. The total probability density function is:

$$F(M_{ee}) = f_{sig}G_{CBM}(M_{ee}) + (1 - f_{sig})P(M_{ee}) \quad (4.12)$$

Fraction of signal  $f_{sig}$  is defined as

$$f_{sig} = nsig/N_{tot}$$

where  $N_{tot}$  is the total number of events in fitted sample and  $nsig$  is fit parameter.

Fraction of background events in sample  $nbkg$  is estimated as  $nbkg = N_{tot}(1 - f_{sig})$

The Crystal Ball function can be defined as

$$G_{CBM}(x) = \begin{cases} \frac{(\frac{n}{|\alpha|})^2 e^{-\frac{1}{2}\alpha^2}}{(\frac{n}{|\alpha|} - |\alpha| - x)^n} & \text{for } x < -|\alpha| \\ \exp^{\frac{1}{2}(\frac{x-m}{\sigma})^2} & \text{for } x > -|\alpha| \end{cases} \quad (4.13)$$

The Crystal Ball line-shape distribution [102] is a Gaussian with a tail on the lower side that is used to describe the effect of radiative energy loss in an invariant mass distribution. It uses the five parameters  $x$ , mean  $m$ , sigma  $\sigma$ , cut  $\alpha$ , power  $n$ . The parameter  $n$  is not necessarily an integer, and is usually held fixed in a fit: lower values generate a longer tail. The parameter  $\alpha$  determines the crossover point from the Gaussian distribution to the power law tail distribution, in units of the peak width  $\sigma$ . Typical values for  $|\alpha|$  are 0.6-1.1. With  $\alpha > 0$  the tail is below the peak, and with a negative value the tail is above the peak.

A maximum likelihood method (see appendix A) is used for fitting the real data. For  $P_t < 1.1$  GeV/c due to the strong proton contamination, a fourth order polynomial is used while a second order polynomial is used for  $P_t > 1.1$  GeV/c. The mass distributions in case of real data for  $DCA < 0.5$  cm,  $TPC \text{ d}E/\text{d}x > 65$  (arb. units) and with different  $P_t$ , are shown in figure 4.19. The results of the fit are summarised in the tables 4.5, 4.6, 4.7, 4.8, 4.9, 4.10.

The parameters **nsig** (number of signal events) and **nbkg** (number of back-

Table 4.2: Table of Crystal-Ball function parameters from the fit to Monte-Carlo primary  $J/\psi$  sample from figure 4.12.

| Name           | Value  | Error  |
|----------------|--------|--------|
| mean           | 3.0981 | 0.0006 |
| sigma $\sigma$ | 0.0206 | 0.0004 |
| alpha $\alpha$ | 0.553  | 0.021  |
| $n$            | 1.485  | 0.037  |

ground events) are computed in the mass range is from  $2.1 < M < 4.2 \text{ GeV}/c^2$  (where  $M$  is the invariant mass). The probability for the non-existence of a peak in the invariant mass distributions in figure 4.19 is respectively, from top left to bottom right: 99%, 0.12%, 22%, 8%, 3%, and 75% (see Appendix-A for details of the calculation).

The results of the fit are cross-checked with the subtraction method in which like sign pairs are subtracted from unlike sign electron pairs. The distributions for different  $P_t$ , having  $DCA < 0.5 \text{ cm}$  and  $TPC \text{ } dE/dx > 65$  (arb. units), are shown in figure 4.20. The results of the fit are shown in table 4.11. The two methods are compatible within uncertainties and the fractional error are the same. But the subtraction method may suffer due to the presence of correlated background (mostly from semileptonic charm decays) in the opposite sign distribution, but also influenced by misidentified electrons. In the ALICE publication [105] the same sign background was multiplied with 1.25. However in this thesis no factor is applied because the subtracted spectrum is consistent with 0 within the uncertainty. Beside the background in the two cases is different because of the different PID procedure applied. In rest of the thesis the average of fitting and subtraction methods will be

used as the signal; the difference relative to the mean is taken as the estimate of the systematic error of the signal extraction. Despite of low statistics there is some evidence that a residual background is still present and this is compatible with the number of events in the subtraction method to be higher than as quoted in table 4.11

Tables 4.3 and 4.4 shows the signal to background ratio for the primary and secondary  $J/\psi$  MC samples. These ratios were not used in the calculations of the cross-section for  $J/\psi$  but in principle shows the effectiveness of the various cuts applied.

Table 4.3: Signal-to-Background ratio in case of Primary  $J/\psi$  MC sample.

| <b>Various steps</b>                                    | <b>S/B ratio</b> |
|---|------------------|
| Without the cuts  | 0.31             |
| With all the cuts mentioned in (4.7.3)                  | 0.49             |
| With all the cuts mentioned in (4.7.3) plus TPC $dE/dx$ | 3.39             |

Table 4.4: Signal-to-Background ratio in case for the Secondary  $J/\psi$  MC sample.

| <b>Various steps</b>                                    | <b>S/B ratio</b> |
|---|------------------|
| Without the cuts  | 0.30             |
| With all the cuts mentioned in (4.7.3)                  | 0.41             |
| With all the cuts mentioned in (4.7.3) plus TPC $dE/dx$ | 5.24             |

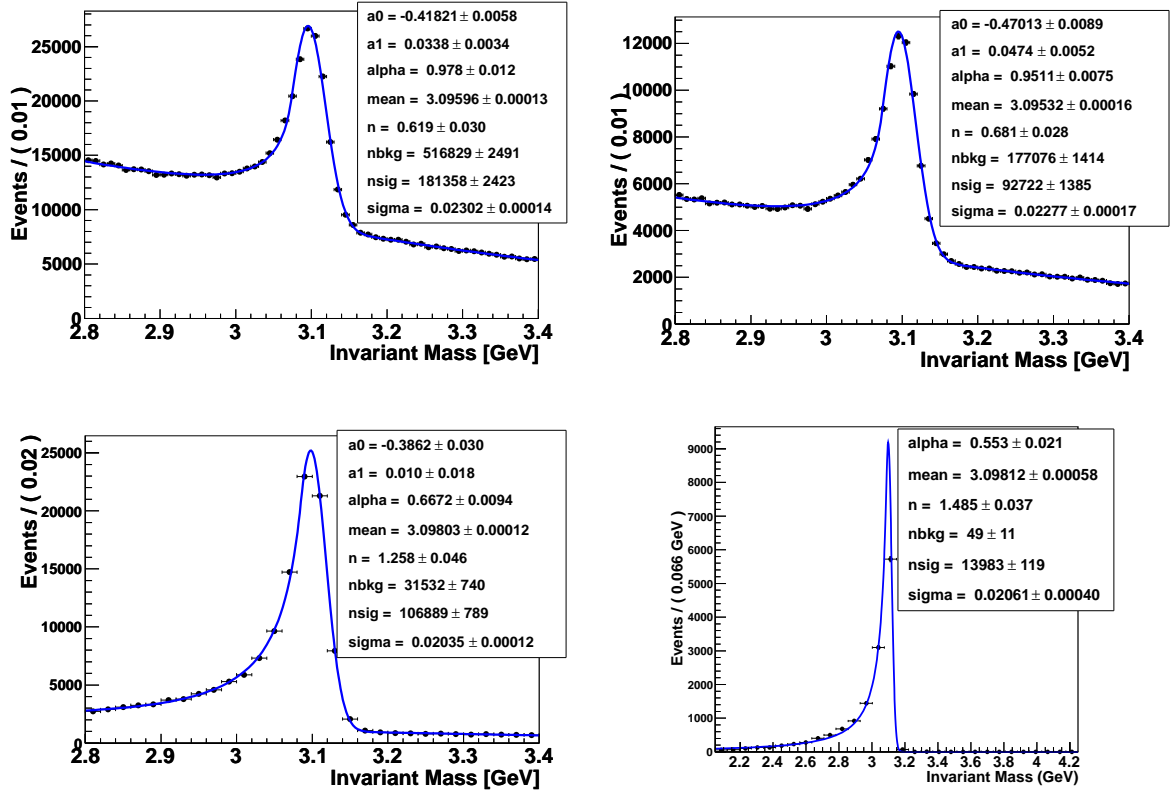


Figure 4.16: Invariant Mass (measured in GeV with natural units  $c=1$ ) distributions for primary  $J/\psi$  MC sample. Top left is the invariant mass plot without any cuts, top right is with  $DCA < 0.5$  cm,  $P_t > 1$  GeV/c for both the positive and negative track. Bottom left is the invariant mass distribution with the above cuts including TPC  $dE/dx > 65$  (arb. units). Bottom right is the invariant mass plot of the  $J/\psi$  with true particle identification of electrons.

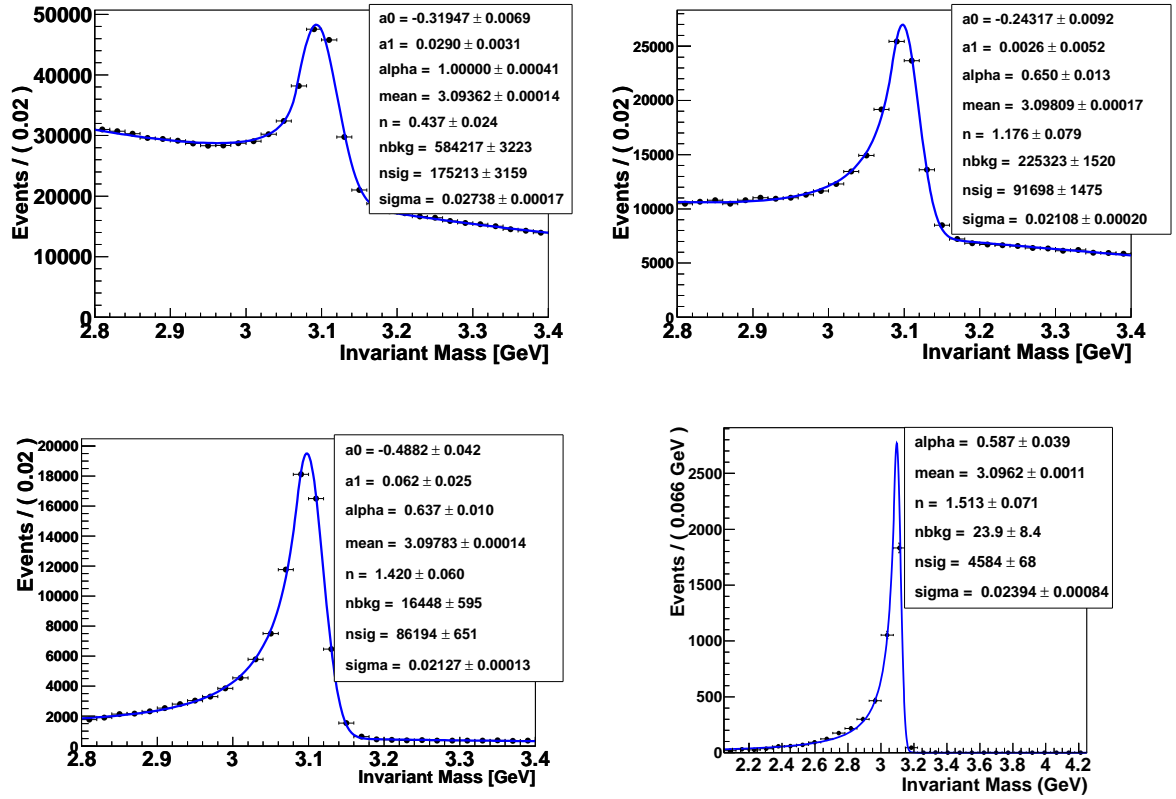


Figure 4.17: Invariant Mass (measured in GeV with natural units  $c=1$ ) distributions for secondary  $J/\psi$  MC sample. Top left is the invariant mass plot without any cuts, top right is with  $\text{DCA} < 5$  cm,  $P_t > 1$  GeV/c for both the positive and negative track. Bottom left is the invariant mass distribution with the above cuts including TPC  $dE/dx > 65$  (arb. units). Bottom right is the invariant mass plot of the  $J/\psi$  with true particle identification of electrons.

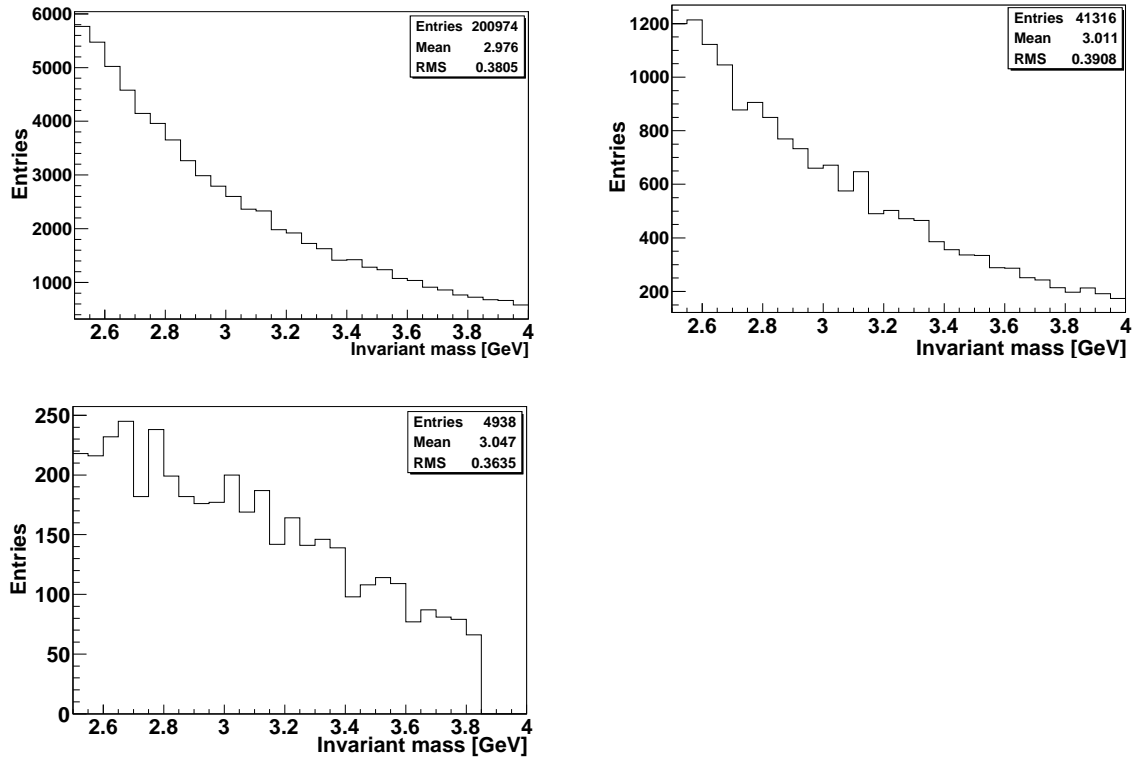


Figure 4.18: Invariant Mass (measured in GeV with natural units  $c=1$ ) distributions for Minimum Bias MC sample. Top left is the invariant mass plot without any cuts, top right is with  $DCA < 0.5$  cm,  $P_t > 1$  GeV/c for both the positive and negative track. Bottom left in the invariant mass distribution with the above cuts including TPC  $dE/dx > 65$  (arb. units). Applying true particle identification all the events are removed.

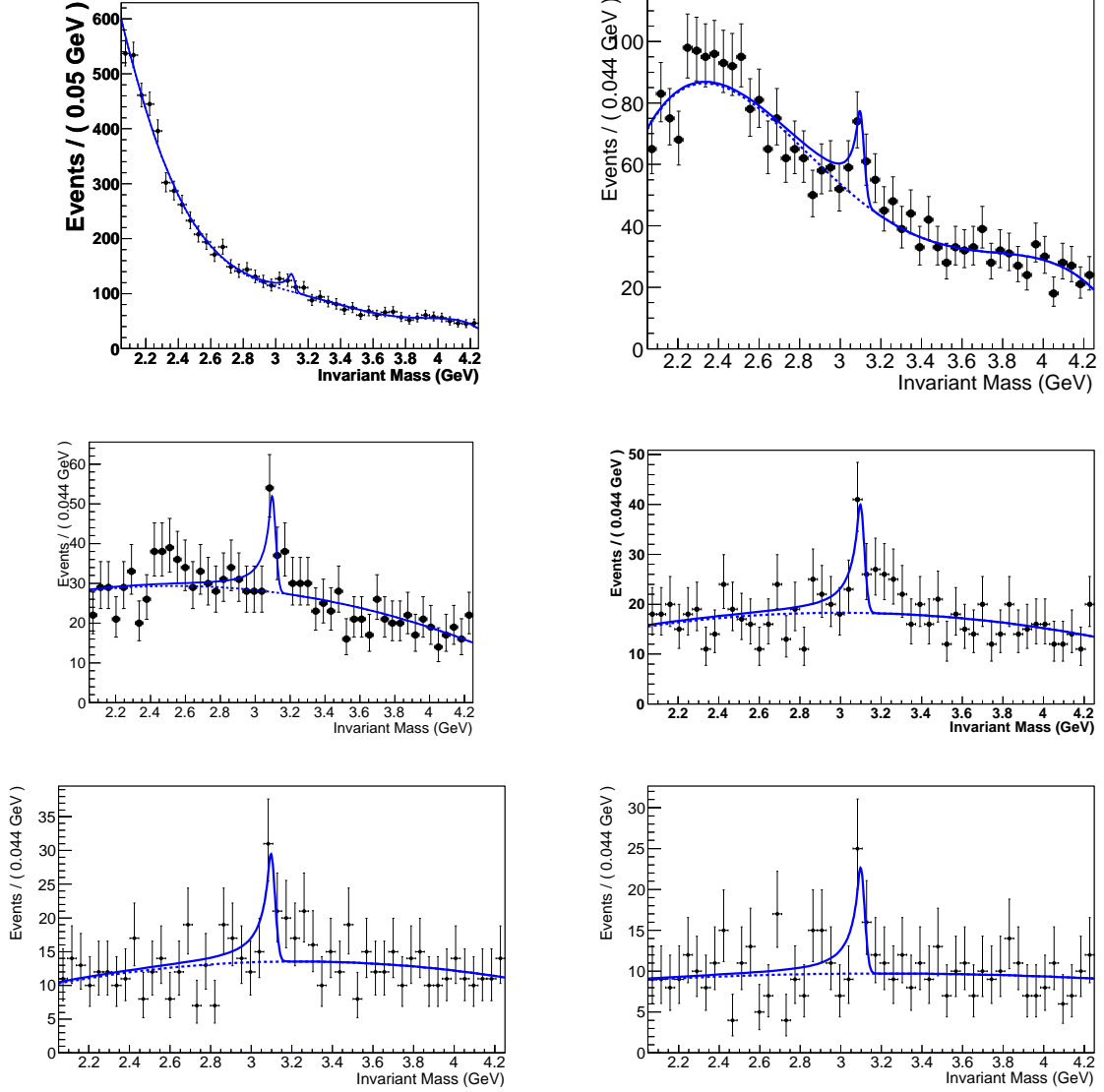


Figure 4.19: Invariant Mass distributions in case of real data sample measured in GeV with natural units  $c=1$ . Top left is the invariant mass plot with  $P_t > 1$  GeV/ $c$ , right is with  $P_t > 1.1$  GeV/ $c$ . In the middle row, left is with  $P_t > 1.2$  GeV/ $c$  while right is with  $P_t > 1.3$  GeV/ $c$ . At bottom, left is with  $P_t > 1.4$  GeV/ $c$  and right with  $P_t > 1.5$  GeV/ $c$ . The bin size is randomly chosen by likelihood fit. The probabilities for non-existence of the peak in the various cases is specified in the main text.

Table 4.5: Table of parameters from the likelihood fit with  $PCUT_t = 1.0$  GeV/c

| Numbers | Name | Value  | Error | Step-size |
|---------|------|--------|-------|-----------|
| 1       | a0   | -1.16  | 0.02  | 4.9e-05   |
| 2       | a1   | 0.59   | 0.02  | 4.0e-05   |
| 3       | a2   | -0.26  | 0.02  | 3.5e-05   |
| 4       | a3   | 0.08   | 0.02  | 3.3e-04   |
| 5       | nbkg | 6735.4 | 87.1  | 1.8e-04   |
| 6       | nsig | 74.4   | 31.6  | 6.0e-04   |

Table 4.6: Table of parameters from the likelihood fit with  $PCUT_t = 1.1$  GeV/c

| Numbers | Name | Value    | Error | Step-size |
|---------|------|----------|-------|-----------|
| 1       | a0   | -0.64    | 0.04  | 5.7e-05   |
| 2       | a1   | -1.9e-03 | 0.04  | 5.2e-05   |
| 3       | a2   | 0.13     | 0.03  | 4.7e-05   |
| 4       | a3   | -0.12    | 0.03  | 9.4e-05   |
| 6       | nbkg | 2609.7   | 55.3  | 2.2e-05   |
| 7       | nsig | 76.2     | 22.9  | 5.8e-05   |

Table 4.7: Table of parameters from the likelihood fit with  $PCUT_t = 1.2$  GeV/c

| Numbers | Name | Value  | Error | Step-size |
|---------|------|--------|-------|-----------|
| 1       | a0   | -0.27  | 0.05  | 5.8e-04   |
| 2       | a1   | -0.12  | 0.05  | 3.8e-05   |
| 3       | nbkg | 1277.9 | 39.1  | 2.1e-04   |
| 4       | nsig | 62.8   | 17.8  | 8.5e-04   |

Table 4.8: Table of parameters from the likelihood fit with  $PCUT_t = 1.3$  GeV/c

| Numbers | Name | Value | Error | Step-size |
|---------|------|-------|-------|-----------|
| 1       | a0   | -0.06 | 0.06  | 5.6e-04   |
| 2       | a1   | -0.12 | 0.06  | 3.7e-05   |
| 3       | nbkg | 849.2 | 31.9  | 5.6e-05   |
| 4       | nsig | 56.8  | 15.1  | 1.18e-04  |

Table 4.9: Table of parameters from the likelihood fit with  $PCUT_t = 1.4$  GeV/c

| Numbers | Name | Value | Error | Step-size |
|---------|------|-------|-------|-----------|
| 1       | a0   | 0.04  | 0.07  | 5.4e-04   |
| 2       | a1   | -0.12 | 0.07  | 1.8e-04   |
| 3       | nbkg | 630.3 | 27.4  | 4.7e-05   |
| 4       | nsig | 41.7  | 12.9  | 9.9e-05   |

Table 4.10: Table of parameters from the likelihood fit with  $PCUT_t = 1.5$  GeV/c

| Numbers | Name | Value   | Error | Step-size |
|---------|------|---------|-------|-----------|
| 1       | a0   | 7.7e-03 | 0.08  | 5.3e-04   |
| 2       | a1   | -0.04   | 0.08  | 3.4e-05   |
| 3       | nbkg | 474.2   | 23.9  | 4.0e-05   |
| 4       | nsig | 34.0    | 11.5  | 8.2e-05   |

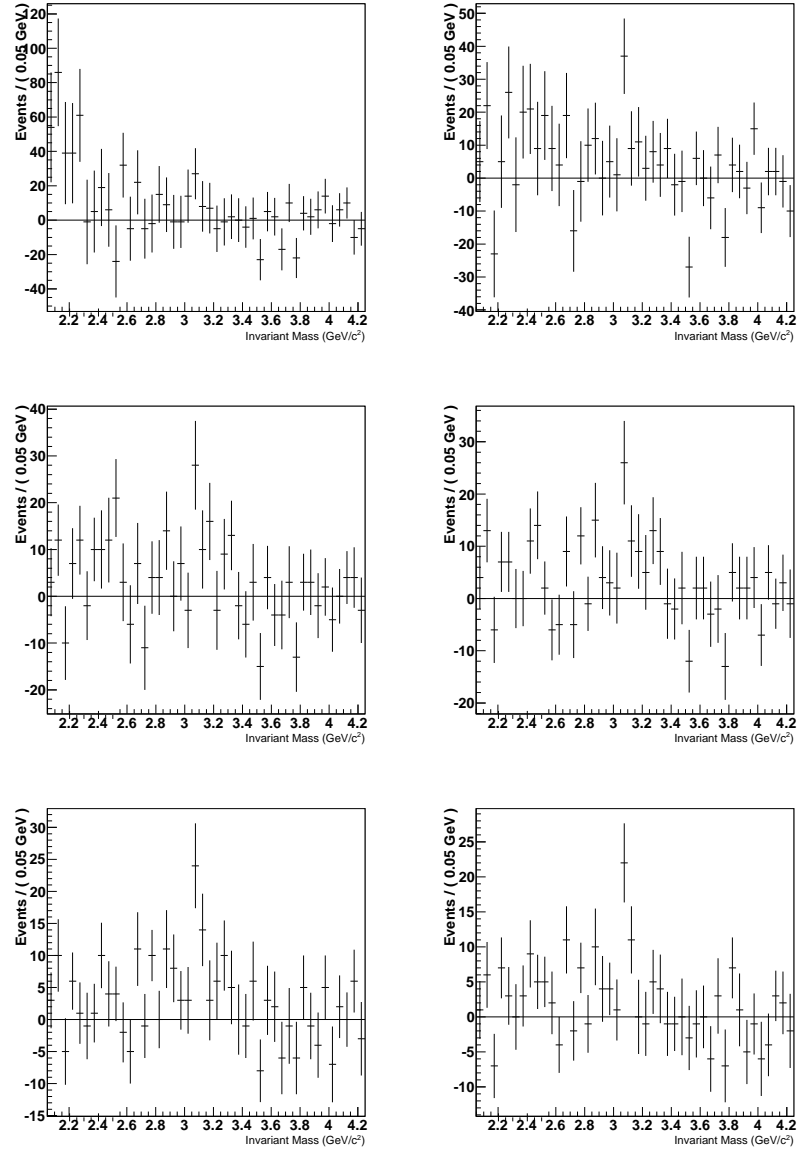


Figure 4.20: Invariant mass distributions in case of real data sample when like signs are subtracted from unlike signs. Top left is the invariant mass plot with  $P_t > 1$  GeV/c, right is with  $P_t > 1.1$  GeV/c. In the middle, left is the invariant mass distribution with  $P_t > 1.2$  while right is with  $P_t > 1.3$  GeV/c. At bottom left, is with  $P_t > 1.4$  GeV/c and right with  $P_t > 1.5$  GeV/c. Outside the signal region, the subtracted spectrum is consistent with 0 within the uncertainty.

Table 4.11: Table of comparison of  $n_{\text{sig}}$  with the errors for different  $P_t$  using the subtraction method and fitting method.  $n_{\text{sig}}$  is the number of signal events that are computed in the mass range from  $2.1 < M < 4.2 \text{ GeV}/c^2$  (where  $M$  is the invariant mass). The yields in the 2nd and 3rd column are relative to same data sample. The fractional errors of the two yields are similar. Therefore the uncertainties on the average yield is taken as the fractional error of the yield in the 2nd column, in order to take into account the correlation.

| $PCUT_t$ [GeV/c] | $n_{\text{sig}}$ (subtraction method) | $n_{\text{sig}}$ (fitting method) | average     |
|------------------|---------------------------------------|-----------------------------------|-------------|
| 1.0              | $76 \pm 45$                           | $74 \pm 32$                       | $75 \pm 39$ |
| 1.1              | $81 \pm 35$                           | $76 \pm 23$                       | $79 \pm 30$ |
| 1.2              | $73 \pm 26$                           | $63 \pm 18$                       | $68 \pm 22$ |
| 1.3              | $77 \pm 21$                           | $57 \pm 15$                       | $67 \pm 18$ |
| 1.4              | $80 \pm 18$                           | $42 \pm 13$                       | $61 \pm 16$ |
| 1.5              | $53 \pm 15$                           | $34 \pm 12$                       | $44 \pm 14$ |

## 4.11 Conclusions

Thus all the cuts mentioned above help in improving the signal(S)-to-background(B) ratio. From the fitted values, S and B are extracted. In the case of the Primary  $J/\psi$  MC sample (figure(4.16)), the ratios of signal to background before and after the cuts are 0.31 and 3.9 respectively, while for the secondary  $J/\psi$  MC sample (figure(4.17)), the ratios are 0.30 and 5.24 respectively. In the case of real data the likelihood fit is performed on different  $P_t$  ranges to see the variation of S/B ratio. The difference between the signal from fitting and subtraction method (see table 4.11) is taken as estimate of systematic error. The choice of  $P_t$  is explained in the next chapter. The corrected yield will be discussed and calculated in the next chapter.

# Chapter 5

## Production of $J/\psi \rightarrow e^+e^-$ in the ALICE Experiment

### 5.1 Introduction to the Correction Framework

In ALICE a framework has been developed to assist users in deriving the corrections for their respective analysis. The main utilities provided by this Correction Framework (CORFW)[103] are the possibilities to store, while performing analysis, both real and simulated data over binned N-dimensional grids. It then derives the efficiency correction maps and corrects the observed data (all stored in the so-called Container Class). Also general selections which may be common to several analysis, at different stages of the selection process (for example, generator, acceptance, reconstruction, user-specific analysis selection), are done within this framework and

the selection variables are all stored in the so-called Selection Class . The user can then calculate efficiencies in terms of the steps one chooses: for example, the ratio between reconstructed and generated levels.

Figure 5.1 shows the general scheme for the CF Container Classes, indicating the main functionalities of each class and the relationships between them. For the Correction Framework in ALICE the two main classes can be categorized into:

- Container Class
- Selection Class

This framework was first used for  $D^0 \rightarrow K\pi$ . Taking that as the base, it was modified by the author for the analysis of  $J/\psi \rightarrow e^+e^-$ .

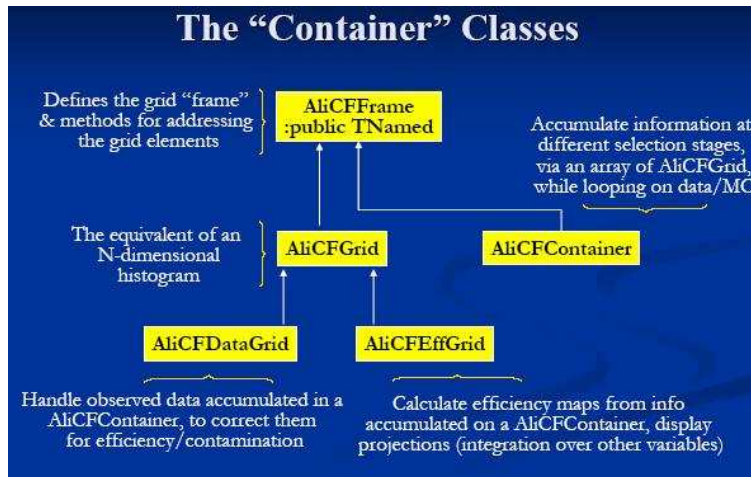


Figure 5.1: General scheme of the CF Container Classes, indicating the main functionalities of each class and relationships between them.

## 5.2 Steps in the Correction Framework

### 5.2.1 Steps at the Generated Level and Reconstructed level

The various selection steps involved at the generation and reconstruction level are:

- particle generation cuts performed on non-kinematic variables of generated particles (PDG value, production vertex, charge etc);
- kinematic cuts, applied both to the generated and reconstructed tracks for a given range in momentum and pseudo-rapidity;
- track quality cuts;
- selection cuts for  $J/\psi$  analysis.

For the efficiency calculations inside the correction framework, a container is defined with a 5-dimensional grid. 5 analysis steps are selected, 2 steps at the generated Monte-Carlo level and 3 at reconstructed level. For each of the 5 steps, five physical variables are considered: invariant mass  $M$ , transverse momentum  $P_T$  and rapidity  $y$  of  $J/\psi$ , transverse momentum of electron (or positron)  $P_T$  and  $\cos \theta^*$  of the electron. The transverse momentum  $P_T$  and  $\cos \theta^*$  of the positron is the same as that of electron.

The two steps at the generated level select the Monte-Carlo  $J/\psi$  decaying into dielectrons inside the fiducial volume which satisfies the condition  $P_T^{GEN} > PCUT_t$  GeV/c and  $\eta_t^{GEN} < 0.9$  for each lepton track.

The steps at the reconstructed level start by looking at reconstructed  $e^+e^-$  pairs. The second step at reconstructed level looks for the  $(e^+e^-)$  candidates which pass the condition  $P_T^{REC} > PCUT_i$  GeV/c and  $\eta_t^{REC} < 0.9$  (known as the acceptance step), along with ITS Cluster  $\geq 5$  (known as ITSCls cut) and TPC Cluster  $> 70$  to improve track quality. The third and final reconstructed step includes  $J/\psi$  selection cuts. For the present studies, the selection cuts include the list of cuts studied in chapter 4 except TPC dE/dx, which was considered in the previous chapter 4, section 4.8.

The AnalysisTask was run on the two AODs simultaneously. For each  $J/\psi$  candidate, either simulated or reconstructed, the five physical variables were calculated and the corresponding grid filled. Figures 5.2 - 5.6 shows the distributions of all 5 variables passing through the different analysis steps for a sample of primary  $J/\psi$  sample containing  $10^6$  events. In the tables 5.2 and 5.3:

- Step1 refers to Monte-Carlo generated  $J/\psi$ .
- Step2 refers to MC generated  $J/\psi$  passing acceptance cuts.
- Step3 is the reconstructed  $J/\psi$  candidates.
- Step4 includes step3 with acceptance, ITS and TPC Clusters cuts to improve track quality.
- Step5 includes step4 with selection cuts for  $J/\psi$  analysis.

From the various steps one can define the acceptance and efficiencies as:

- The geometrical acceptance:  $acc = \text{step2}/\text{step1}$ .
- The reconstruction efficiency:  $eff_{reco} = \text{step3}/\text{step2}$
- Track Cluster Cut efficiency:  $eff_{cluster} = \text{step4}/\text{step3}$ .
- Analysis efficiency:  $eff_{anal} = \text{step5}/\text{step4}$ .
- The weight:  $1/w = acc \times eff_{reco} \times eff_{cluster} \times eff_{anal} = \text{step5}/\text{step1}$ .

To maximise the number of  $J/\psi$  candidates the selection cuts are left as open as possible leading to almost 100% analysis efficiency.

## 5.2.2 Calculation of $J/\psi$ yield

Assuming that the Particle Identification (PID) procedure has 100% efficiency, and the Monte-Carlo sample was generated with the correct  $p_T$  and  $y$  distributions for the  $J/\psi$ , the observed yield  $Y$  is:

$$Y = N_{signal} \times w \quad (5.1)$$

where  $N_{signal}$  is taken from the fit to the invariant mass spectrum for data, (figure 5.9) and the weight is  $w = \frac{N_{signal}^{Gen}}{N_{signal}^{Gen}}$ , where  $N_{signal}^{Gen}$  is the number of generated  $J/\psi$  at step1 and  $N_{signal}^{Gen}$  is the number of reconstructed  $J/\psi$  in step5.

If instead the PID procedure is not fully efficient, the corrected number of  $J/\psi$  is given by

$$N_{J/\psi}^{PID} = \frac{N_{signal}}{f^2} \quad (5.2)$$

where  $f$  is the efficiency of electron identification (detailed discussion in section 4.8). The residual contamination from hadrons is assumed to be removed by using either a fit to the signal and background or by like-sign pair background subtraction (see section 4.10). The validity of this assumption is demonstrated in table 5.1 where a MC sample of primary  $J/\psi$  is used to compare the fit results and like-sign subtracted  $N_{signal}$  with respect to known number of  $J/\psi$ .

Table 5.1: Evaluation of signal extraction by fitting compared to like-sign pair subtraction. The cuts are those described in section 4.7.3. PID selection is done by MC TPC energy loss  $dE/dx$ .

|                  | No. of events | Fitting method | Like-sign subtraction |
|------------------|---------------|----------------|-----------------------|
| True             | 10000         | 1006           | 1006                  |
| Cuts without PID | 10000         | $1186 \pm 204$ | $1029 \pm 64$         |
| Cuts with PID    | 10000         | $1183 \pm 79$  | $1033 \pm 41$         |

Therefore the corrected number of  $J/\psi$  is instead :

$$Y = N_{J/\psi}^{PID} \times w. \quad (5.3)$$

The geometrical acceptance  $acc$ , reconstruction efficiency  $eff_{reco}$ , track cluster cut efficiency  $eff_{cluster}$ , analysis efficiency  $eff_{anal}$  and weight  $w$  for primary and secondary MC  $J/\psi$  samples for transverse momenta of  $J/\psi$  decay products  $P_T < 1$  GeV/c (i.e.  $PCUT_T = 1$ ) are given in table 5.2. The average acceptance for the secondary  $J/\psi$  is higher than for primary  $J/\psi$  due to the difference in the kinematic distributions. On the contrary, reconstruction efficiency is higher for the primary

$J/\psi$  sample due to the selection of primary tracks. As a result, the final weights for primary and secondary  $J/\psi$  are comparable. The  $J/\psi$  selection cuts do not bias the data sample with respect to the origin of the  $J/\psi$  (primary and secondary). In tables 5.3 and 5.4, the  $acc$ ,  $eff$ , and the  $w$  are given for different  $PCUT_T$  in case of primary and secondary  $J/\psi$  MC sample. The acceptances decrease with the increase of  $P_T$  while the efficiencies remains the same. This is due to the fact that the distribution of lepton momenta has a maximum around 1 GeV/c. So, bigger  $PCUT_T$  means that we are losing more  $J/\psi$ . The final weights for primary and secondary  $J/\psi$  are comparable.

Table 5.2: Table of acceptance and efficiency for Primary and Secondary  $J/\psi$  MC sample for  $PTCUT_T = 1$  GeV/c.

| Steps                                       | Primary MC $J/\psi$ sample | Secondary MC $J/\psi$ sample |
|---|----------------------------|------------------------------|
| $acc = \text{step2}/\text{step1}$           | $0.325 \pm 0.002$          | $0.378 \pm 0.003$            |
| $eff_{reco} = \text{step3}/\text{step2}$    | $0.808 \pm 0.001$          | $0.650 \pm 0.001$            |
| $eff_{cluster} = \text{step4}/\text{step3}$ | $0.658 \pm 0.001$          | $0.658 \pm 0.001$            |
| $eff_{anal} = \text{step5}/\text{step4}$    | $0.999 \pm 0.0002$         | $0.999 \pm 0.002$            |
| $1/w = \text{step5}/\text{step1}$           | $0.173 \pm 0.001$          | $0.162 \pm 0.001$            |

The fraction of secondary  $J/\psi$  at the LHC energy of 7 TeV is estimated to be about 20% [104] with large uncertainty. To estimate the uncertainty due to the differences in correction factors for primary and secondary  $J/\psi$  (see table 5.2), the final weight is taken as the average ( assuming equal proportions) of the weights of primary and secondary  $J/\psi$  for  $PCUT_t = 1.3$  GeV/c:

$$1/w = 0.1025 \pm 0.0028 \quad (5.4)$$

Table 5.3: Table of acceptance and efficiency for Primary  $J/\psi$  MC sample with different  $PCUT_T$  cuts.

| $PCUT_t$ [GeV/c] | $acc = \text{step2}/\text{step1}$ | $eff = \text{step5}/\text{step2}$ | $1/w = \text{step5}/\text{step1}$ |
|------------------|-----------------------------------|-----------------------------------|-----------------------------------|
| 1.1              | $0.266 \pm 0.001$                 | $0.533 \pm 0.001$                 | $0.142 \pm 0.001$                 |
| 1.2              | $0.235 \pm 0.001$                 | $0.523 \pm 0.001$                 | $0.123 \pm 0.007$                 |
| 1.3              | $0.201 \pm 0.001$                 | $0.511 \pm 0.001$                 | $0.103 \pm 0.004$                 |
| 1.4              | $0.167 \pm 0.001$                 | $0.507 \pm 0.001$                 | $0.085 \pm 0.004$                 |
| 1.5              | $0.135 \pm 0.001$                 | $0.506 \pm 0.001$                 | $0.068 \pm 0.004$                 |

Table 5.4: Table of acceptance and efficiency for Secondary  $J/\psi$  MC sample with different  $P_T$  cuts.

| $PCUT_t$ [GeV/c] | $acc = \text{step2}/\text{step1}$ | $eff = \text{step5}/\text{step2}$ | $1/w = \text{step5}/\text{step1}$ |
|------------------|-----------------------------------|-----------------------------------|-----------------------------------|
| 1.1              | $0.352 \pm 0.001$                 | $0.392 \pm 0.001$                 | $0.137 \pm 0.001$                 |
| 1.2              | $0.317 \pm 0.001$                 | $0.365 \pm 0.001$                 | $0.116 \pm 0.007$                 |
| 1.3              | $0.282 \pm 0.001$                 | $0.362 \pm 0.001$                 | $0.102 \pm 0.004$                 |
| 1.4              | $0.247 \pm 0.001$                 | $0.358 \pm 0.001$                 | $0.088 \pm 0.004$                 |
| 1.5              | $0.215 \pm 0.001$                 | $0.352 \pm 0.001$                 | $0.076 \pm 0.004$                 |

and the difference between the two estimates is within statistical error. Recent measurement from other LHC experiment indicate a substantial component of secondary  $J/\psi$ . The exact ratio between primary and secondary  $J/\psi$  has small impact on the weight because the acceptance are very similar.

The next source of systematic error to be considered is the dependence of the weight on the  $J/\psi$  momentum distribution. A simple Monte-Carlo is used to estimate this effect. The Monte-Carlo takes into account the kinematics of the  $J/\psi$  decay and the acceptance of the ALICE TPC detector. In accordance with the PYTHIA generator,  $J/\psi$  particles with a flat rapidity distribution and exponential transverse momentum distribution  $dN/dP_T \propto P_T^{1.5} \exp(-\alpha P_T)$ , with  $\alpha = 0.95 \text{ GeV}^{-1}$  are generated. The calculated acceptance for  $\alpha = 0.95 \text{ GeV}^{-1}$  is equivalent to the acceptance as defined in table 5.3; and gives the value of 0.201 indeed. To study the influence of the momentum distribution on acceptance, the transverse momentum distribution is modified by changing the slope  $\alpha$  by 10%, and the flat rapidity distribution is modified to a Gaussian with  $\sigma = 6$  as estimated from ALICE dimuon data [105]. The results are in table 5.5. A systematic error of 13% is calculated, as maximum difference between the reference value and the values from modified distribution acceptances.

The other source of systematic error is the unknown  $J/\psi$  polarization. The angular distribution of leptons from  $J/\psi$  decay, integrated over the azimuthal angle, is given by [106]

$$\frac{d\sigma}{d\cos\theta^*} = A(1 + \lambda \cos^2\theta^*) \quad (5.5)$$

where  $A$  is a normalization constant and  $\theta^*$  is the angle between the momentum vector of electron (positron) and the direction of  $J/\psi$  momentum in the  $J/\psi$  rest

frame. The polarization parameter  $\lambda \in [-1, 1]$  is related to the dynamics of the  $J/\psi$  production. The systematic uncertainty due to the polarization is estimated as the variation of  $J/\psi$  acceptance between  $\lambda = -1$  and  $\lambda = 1$  in two different  $J/\psi$  centre of mass frames (for details see appendix B). The results are in table 5.6. The errors are quoted as a percentage.

Table 5.5: Variation of  $J/\psi$  acceptance with momentum distribution for different  $\alpha$  values.

| Rapidity Distribution | Slope $\alpha = 0.95$ | $\alpha = 1.045$ | $\alpha = 0.855$ |
|-----------------------|-----------------------|------------------|------------------|
| Flat                  | 0.201                 | 0.193            | 0.214            |
| Gauss                 | 0.208                 | 0.199            | 0.220            |

Table 5.6: Variation of  $J/\psi$  acceptance with polarization both for Helicity (HE) and Collins-Soper (CS) frames. For example the percentage error for  $\lambda = -1$  represents the difference between the acceptance for  $\lambda = -1$  with respect to  $\lambda = 0$ .

|            | $\lambda = 0$ | $\lambda = -1$ | $\lambda = 1$ |
|------------|---------------|----------------|---------------|
| acc. (HE)  | 0.201         | 0.248          | 0.179         |
| Error (HE) | 0             | +18.9%         | -12.3%        |
| acc. (CS)  | 0.201         | 0.260          | 0.173         |
| Error (CS) | 0             | +22.7%         | -16.2%        |

### 5.3 Checking of correction procedure using Monte-Carlo Samples

For real data, the  $J/\psi$  yield is calculated by multiplying the raw number of  $J/\psi$  obtained from the reconstructed distribution by the correction factor, i.e the weight

$w$ . To check the procedure, an exercise was performed using a fraction of Monte-Carlo data in the role of **real data**, using the correction framework (CORRFW). The MC sample of primary  $J/\psi$  containing about 2 million events was divided into two halves (sample 1 and sample 2). Sample 1 was considered to be real data (964200 events) while the sample 2 (933336 events) was used to retrieve the correction factor. The invariant mass distributions for each of the correction framework steps for the first half are shown in figure 5.7; the fitted mass plots after step 5 are shown in figure 5.8 for both samples. Figure 5.8 (left) refers to the first half and 5.8 (right) refers to the second half.

The correction factor  $w$  obtained from the sample 2 is defined as the ratio of the number of  $J/\psi$  in step 1 to the  $N_{signal}$  from the step 5 when fitted with Crystal-Ball function. Thus according to relation (5.1):

$$N(J/\psi) = w \times N_{signal} \quad (5.6)$$

where  $N_{signal}$  is the number of  $J/\psi$  when fitted with Crystal-Ball in step 5 from sample 1 and  $N(J/\psi)$  is the corrected Number of  $J/\psi$  in step 1 from sample 2. Substituting the values in equation (5.6) gives:

$$N_{J/\psi} = \frac{944200}{17569} \times 17293 = 929367. \quad (5.7)$$

The error of the result is the sum of fractional errors on the weight  $w$  and  $N_{signal}$ , giving:

$$N_{J/\psi} = 930,000 \pm 10,000 \quad (5.8)$$

This result is to be compared with the total number of  $J/\psi$  generated for the sample 2 which is 933336. Therefore the result is less than 1 standard deviation from the corrected value.

## 5.4 Measurement of the inclusive production $J/\psi$ cross-section ( $\sigma_{J/\psi}$ )

The  $J/\psi$  cross-section (sum of primary and secondary production)  $\sigma_{J/\psi}$  is defined as:

$$\sigma_{J/\psi} = \frac{N_{J/\psi}}{L} \quad (5.9)$$

where  $L$  is the integrated luminosity for the analyzed data sample and it is calculated as in equation 5.10. The integrated luminosity corresponding to the data set analyzed in this thesis is  $(1.25 \pm 0.09) \text{ nb}^{-1}$ :

$$L = \frac{N_{MB}}{\sigma_{MB}} = (1.25 \pm 0.09) \text{ nb}^{-1} \quad (5.10)$$

where  $\sigma_{MB} = 62.3 \pm 0.4 \text{ (stat)} \pm 4.3 \text{ (syst) mb}$  is the cross-section of minimum bias events measured in a Van Der Meer scan [108] and  $N_{MB} = 78$  million is the number of recorded minimum bias events..

The corresponding invariant mass plot of  $J/\psi$  with the selection cuts described in section (5.2.1) is shown in figure 5.9 and for an independent analysis done by ALICE [105] is shown in figure 5.10 respectively. In table 4.11 the results of the average between maximum likelihood fit and subtraction method gives for  $J/\psi$  decaut product transverse momenta  $P_T > 1.3 \text{ GeV}/c$  (i.e.  $PTCUT_T = 1.3 \text{ GeV}/c$ ):

$$N_{J/\psi} = 67 \pm 18 \quad (5.11)$$

The dependence of  $N_{J/\psi}$  on the  $P_T$  range was studied. The maximum likelihood fit was performed in six different  $P_T$  bins starting from 1.0 GeV/c to 1.5 GeV/c. For the calculation of the  $J/\psi$  cross-section,  $PTCUT_T > 1.3$  GeV/c is chosen as the pion contamination is least with this cut.

The PID efficiency for electrons as calculated in section (4.8) is

$$f = 0.95 \pm 0.05$$

The total correction factor for  $PTCUT_T > 1.3$  GeV/c is  $w = 9.76 \pm 0.04$ . So the corrected yield is

$$Y = \frac{N_{J/\psi}^{PID}}{f^2} w = \frac{67}{0.95^2} \times 9.76 \quad (5.12)$$

$$Y = 725 \pm 195 \quad (5.13)$$

The yields resulting from table 4.11, corresponding to different cuts  $P_T$  ( $PTCUT_T$ ) are given in table 5.7.

Table 5.7: Comparison of yields for different  $PTCUT_T$  resulting from fitting procedure

| $PTCUT_T$ (GeV/c) | Yield from fitting |
|-------------------|--------------------|
| 1.0               | $480 \pm 250$      |
| 1.1               | $616 \pm 242$      |
| 1.2               | $612 \pm 204$      |
| 1.3               | $725 \pm 195$      |
| 1.4               | $795 \pm 209$      |
| 1.5               | $717 \pm 228$      |

Therefore the cross-section for  $J/\psi \rightarrow e^+e^-$  is

$$\sigma(J/\psi \rightarrow e^+e^-) = \frac{Y}{L} = \frac{725}{1.25} \quad (5.14)$$

$$\sigma(J/\psi \rightarrow e^+e^-) = [580 \pm 156(stat.)] \text{ nb} \quad (5.15)$$

Given that the branching ratio of  $J/\psi \rightarrow e^+e^-$ :

$$J/\psi \rightarrow e^+e^- = (5.94 \pm 0.06)\% \quad (5.16)$$

Therefore the cross-section is:

$$\sigma(J/\psi) = \frac{\sigma(J/\psi \rightarrow e^+e^-)}{0.0594} \quad (5.17)$$

Thus the final cross-section of the  $J/\psi$  for  $|y| < 0.9, P_t > 0$  is:

$$\sigma(J/\psi) = [9.8 \pm 2.6(stat.) \pm 1.8(sys.)_{+2.0}^{-1.5}(syst.pol.)] \mu b \quad (5.18)$$

$$\sigma(J/\psi), (|y| < 0.9, P_t > 0) \quad (5.19)$$

Table (5.8) contains a summary of the systematic errors. The first column describes the source of systematic error, the second column is the estimated magnitude of the uncertainty. The third column refers to where the procedure of error estimation is described.

## 5.5 Comparison with other experiments

The  $J/\psi$  production in  $p + p$  collisions at  $\sqrt{s} = 200$  GeV has been measured by the PHENIX experiment at the BNL Relativistic Heavy Ion Collider (RHIC) [109], by

Table 5.8: Table of Systematic Errors

| Sources of systematic errors | Percentage (%) |                | Reference     |
|------------------------------|----------------|----------------|---------------|
| Signal Extraction            | 15             |                | Section 4.10  |
| PID cuts                     | 4              |                | Section 4.8   |
| Primary/Secondary $J/\psi$   | < 3            |                | Section 5.2.2 |
| $P_T$ and $y$ distribution   | 13.0           |                | Section 5.2.2 |
| Total systematic error       | 20             |                |               |
| Polarization                 | $\lambda = -1$ | $\lambda = +1$ | Section 5.2.2 |
| CS                           | +22.7          | -16.2          |               |
| HE                           | +18.9          | -12.3          |               |

CDF [110] in  $p\bar{p}$  collisions at  $\sqrt{s} = 1960 \text{ GeV}$  and by the ATLAS [111], CMS [104] and ALICE [105] and LHCb [112] experiments at  $7 \text{ TeV}$  at LHC.

The PHENIX experiment measures the  $J/\psi$  production for transverse momentum  $P_T > 0 \text{ GeV}/c$  in two rapidity windows:  $|y| < 0.35$  for dielectrons and  $|y| \in [1.2, 2.2]$  for dimuons. The total cross-section times the branching ratio  $B_{u\sigma}^{J/\psi} = 178 \pm 3(stat.) \pm 53(stat.) \pm 18(norm) \text{ nb}$  is obtained from a fit to the measured  $J/\psi$  rapidity distribution using a double Gaussian. The cross-section at central rapidity used for comparison in this section is read from figure 4 of paper [109] as  $BR(J/\psi \rightarrow e^+e^-) \times d\sigma/dy(y=0) = 43.0 \pm 2.5(stat) \pm 5.0(sys) \text{ nb}$ .

The CDF experiment measures the  $J/\psi$  production for transverse momentum  $P_T > 0 \text{ GeV}/c$  in rapidity window  $|y| < 0.6$  in the dimuon channel. The  $J/\psi$  cross-section of  $4.08 \pm 0.02(stat)_{0.33}^{+0.36}(syst) \mu b$  is measured in this window. The value at central rapidity is obtained dividing by 1.2 ( the width of the rapidity window).

The CMS experiment measures the  $J/\psi$  production for transverse momentum  $P_T > 6.5$  GeV/c and in a rapidity window  $|y| < 2.4$ , in the dimuon channel. The  $J/\psi$  cross-section times the dimuon decay branching fraction is  $70.9 \pm 2.1(stat.) \pm 3.0(sys) \pm 7.8(luminosity)$  nb for the prompt  $J/\psi$  meson, and  $26.0 \pm 1.4(stat.) \pm 1.6(syst.) \pm 2.9(luminosity)$  nb for the  $J/\psi$  mesons from b-hadron decays.

The ATLAS experiment measures the  $J/\psi$  production for transverse momentum  $P_T > 7$  GeV/c and in a rapidity window  $|y| < 2.4$ , in the dimuon channel. The  $J/\psi$  cross-section times the dimuon decay branching fraction is  $59 \pm 1(stat.) \pm 8.0(sys) \pm 2(luminosity)$  nb for the prompt  $J/\psi$  meson, and  $23.0 \pm 0.6(stat.) \pm 2.8(syst.) \pm 0.8(luminosity)$  nb for the  $J/\psi$  mesons from b-hadron decays.

The LHCb experiment measures the  $J/\psi$  production for transverse momentum  $P_T \in [0, 14]$  GeV/c and in a rapidity window  $|y| \in [2.0; 4.5]$  in the dimuon channel. The measured  $J/\psi$  cross-sections are  $10.5 \pm 0.04(stat.) \pm 1.40(sys)$  nb for the prompt  $J/\psi$  meson, and  $1.14 \pm 0.01(stat.) \pm 0.16(syst.)$   $\mu b$  for the  $J/\psi$  mesons from b-hadron decays.

The cross-sections at  $y = 0$  for PHENIX, CDF, and ALICE experiments as a function of centre of mass energies of colliding beams are shown in figure 5.11. The ATLAS, CMS and LHCb points cannot be added due to the transverse momentum cut (ATLAS, CMS) and rapidity (LHCb) cuts. For the ALICE experiment two points are presented. The red one corresponds to results published in [105] ( $10.7 \pm 1.2(stat.) \pm 1.7(syst.)_{-2.3}^{+1.6}$ )  $\mu b$  and was produced by an analysis of full ALICE data set done independently from that presented in this thesis. The blue one is the result of analysis presented in this thesis.

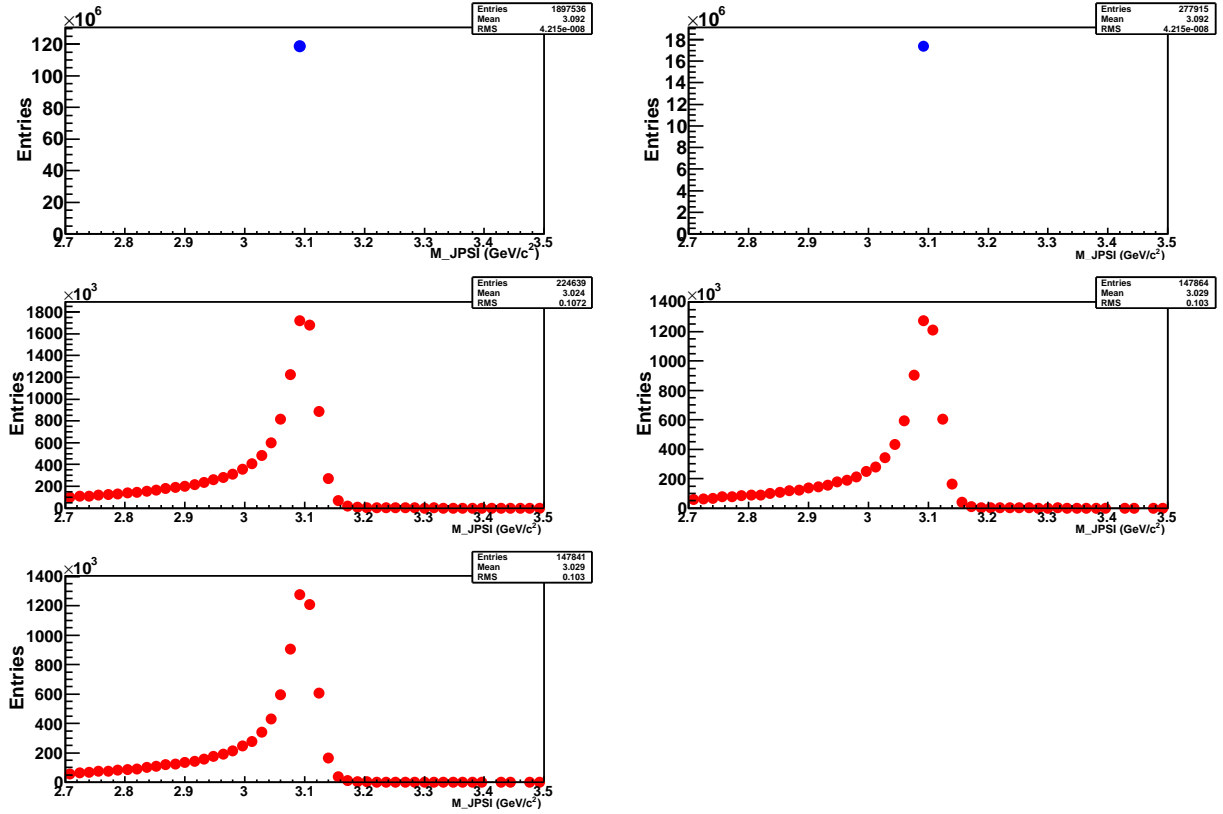


Figure 5.2: Top left: Invariant mass of primary  $J/\psi$  at the generated level; Top right: Invariant mass of  $J/\psi$  at the generated level including the acceptance cuts; Middle left: Invariant mass of  $J/\psi$  at reconstructed level including the vertex and refit cuts; Middle right: Invariant mass of  $J/\psi$  including above cuts, acceptance and ITSCluster cuts; Bottom left: Invariant mass of  $J/\psi$  including all above selection criteria and selection cuts mentioned in chapter 4. Mass is measured in GeV (natural units for  $c=1$ )

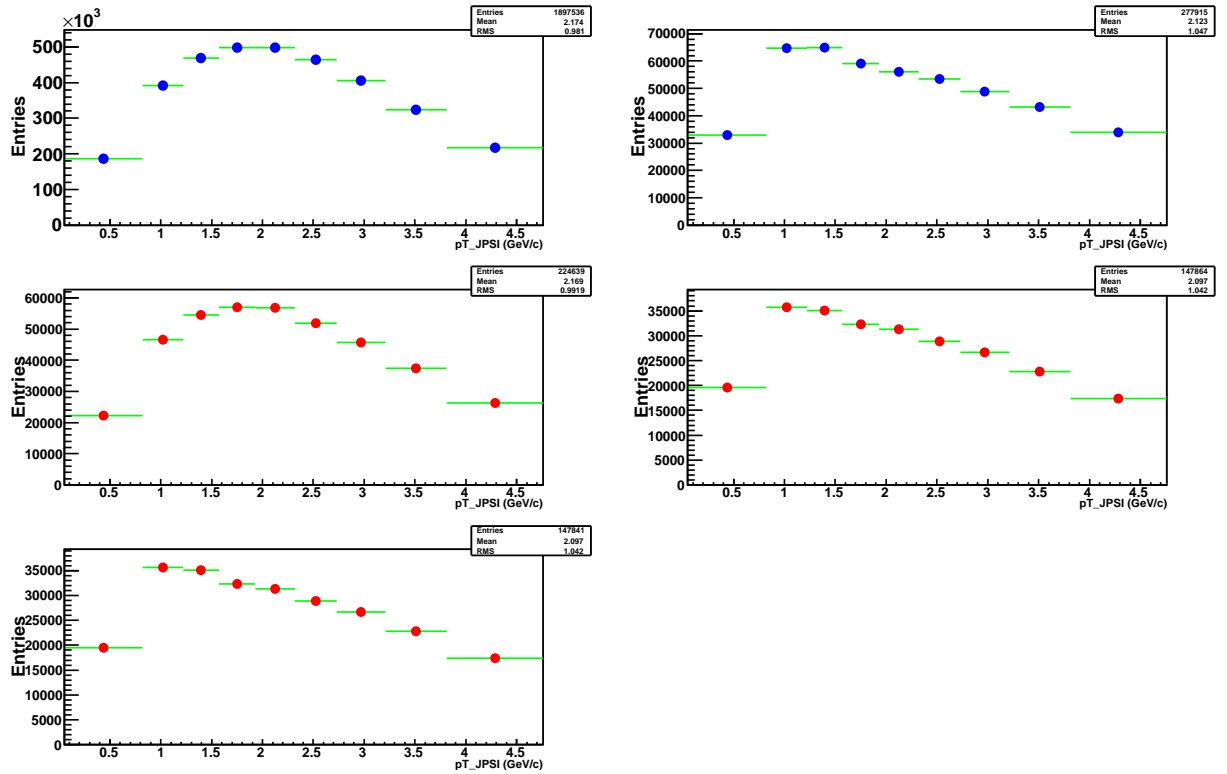


Figure 5.3: Top left:  $P_T$  of  $J/\psi$  at the generated level, Top right:  $P_T$  of  $J/\psi$  at the generated level including the acceptance cuts, Middle left:  $P_T$  of  $J/\psi$  at reconstructed level including the vertex and refit cuts, Middle right:  $P_T$  of  $J/\psi$  including above cuts, acceptance and ITSCluster cuts, Bottom left:  $P_T$  of  $J/\psi$  including above and selection cuts.

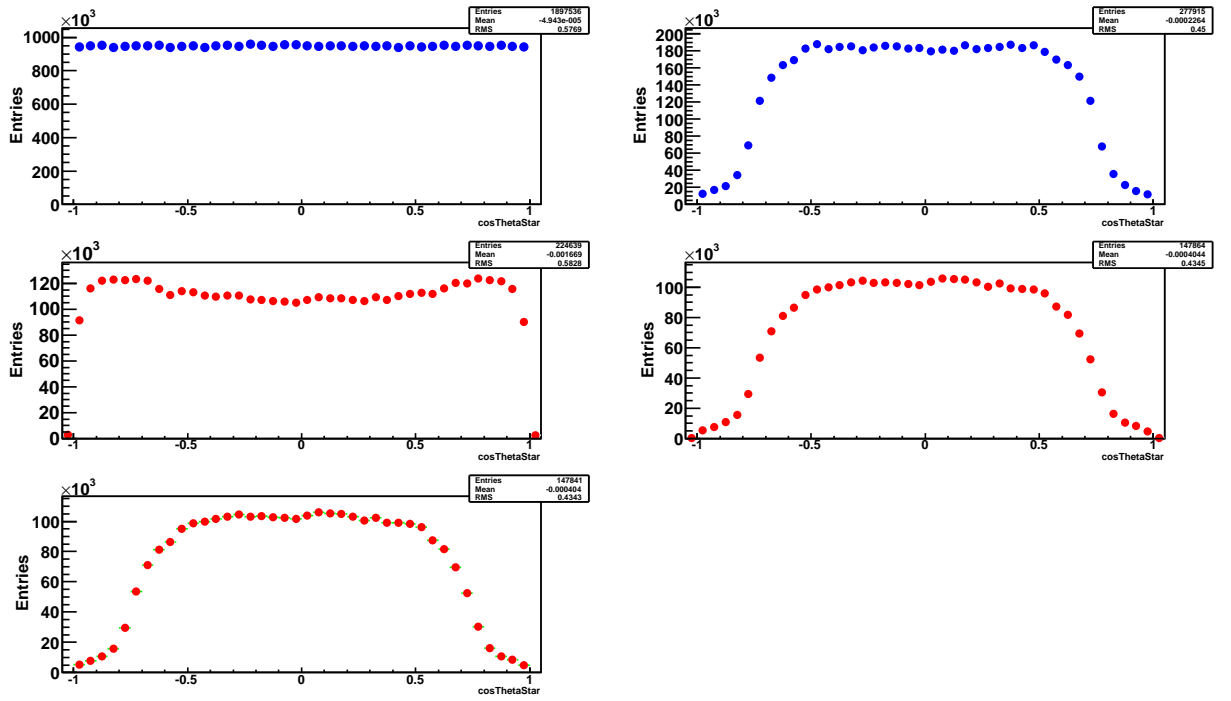


Figure 5.4: Top left: Rapidity of  $J/\psi$  at the generated level, Top right: Rapidity of  $J/\psi$  at the generated level including the acceptance cuts, Middle left: Rapidity of  $J/\psi$  at reconstructed level including the vertex and refit cuts, Middle right: Rapidity of  $J/\psi$  including above cuts, acceptance and ITSCluster cuts, Bottom left: Rapidity of  $J/\psi$  including above and selection cuts.

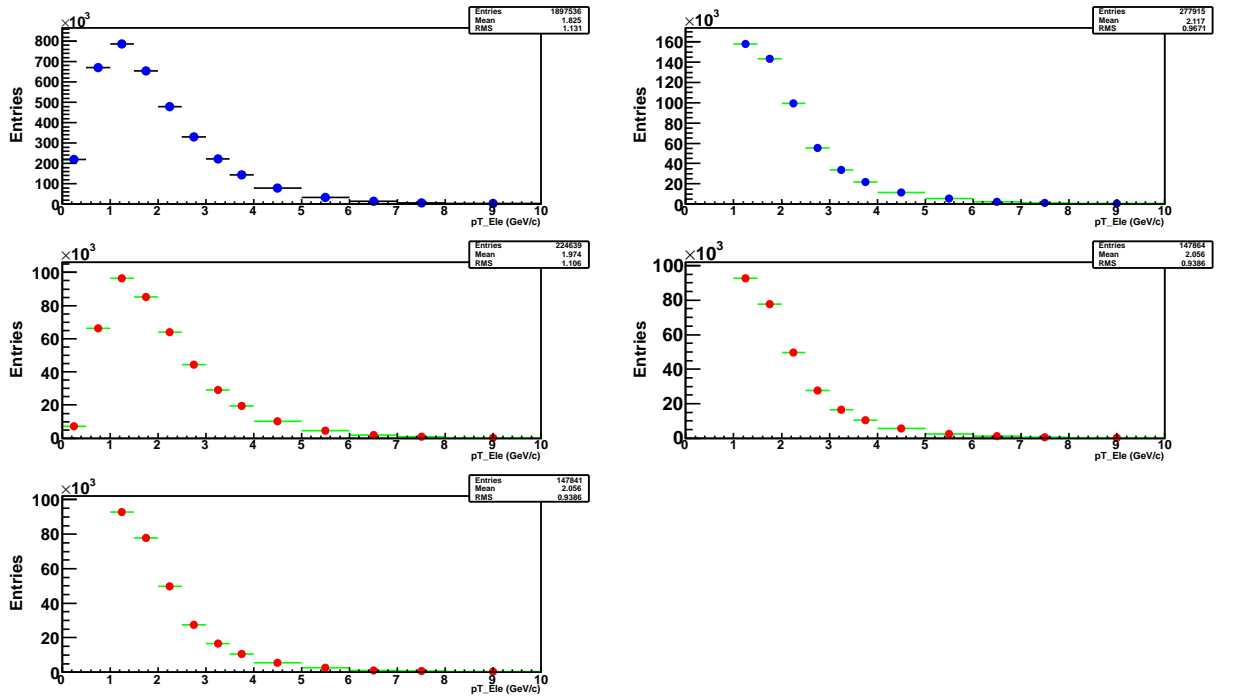


Figure 5.5: Top left:  $P_T$  of electrons at the generated level, Top right:  $P_T$  of electrons at the generated level including the acceptance cuts, Middle left:  $P_T$  of electrons at reconstructed level including the vertex and refit cuts, Middle right:  $P_T$  of electrons including above cuts, acceptance and ITSCluster cuts, Bottom left:  $P_T$  of electron or positrons including above and selection cuts.

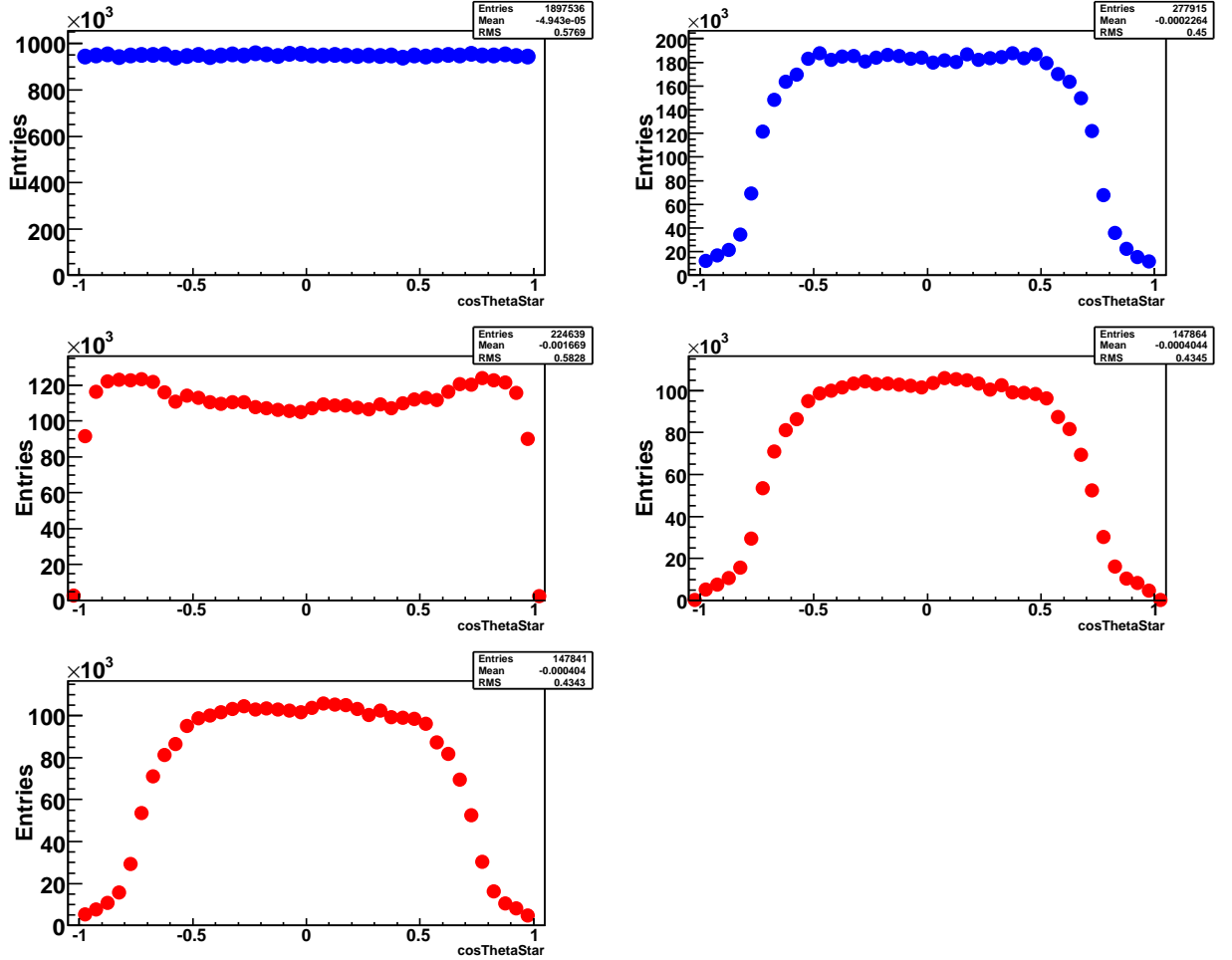


Figure 5.6: Top left:  $\cos\theta^*$  distribution at the generated level, Top right:  $\cos\theta^*$  distribution at the generated level including the acceptance cuts, Middle left:  $\cos\theta^*$  distribution at reconstructed level including the vertex and refit cuts, Middle right:  $\cos\theta^*$  distribution including above cuts, acceptance and ITSCluster cuts, Bottom left:  $\cos\theta^*$  distribution including above and selection cuts.

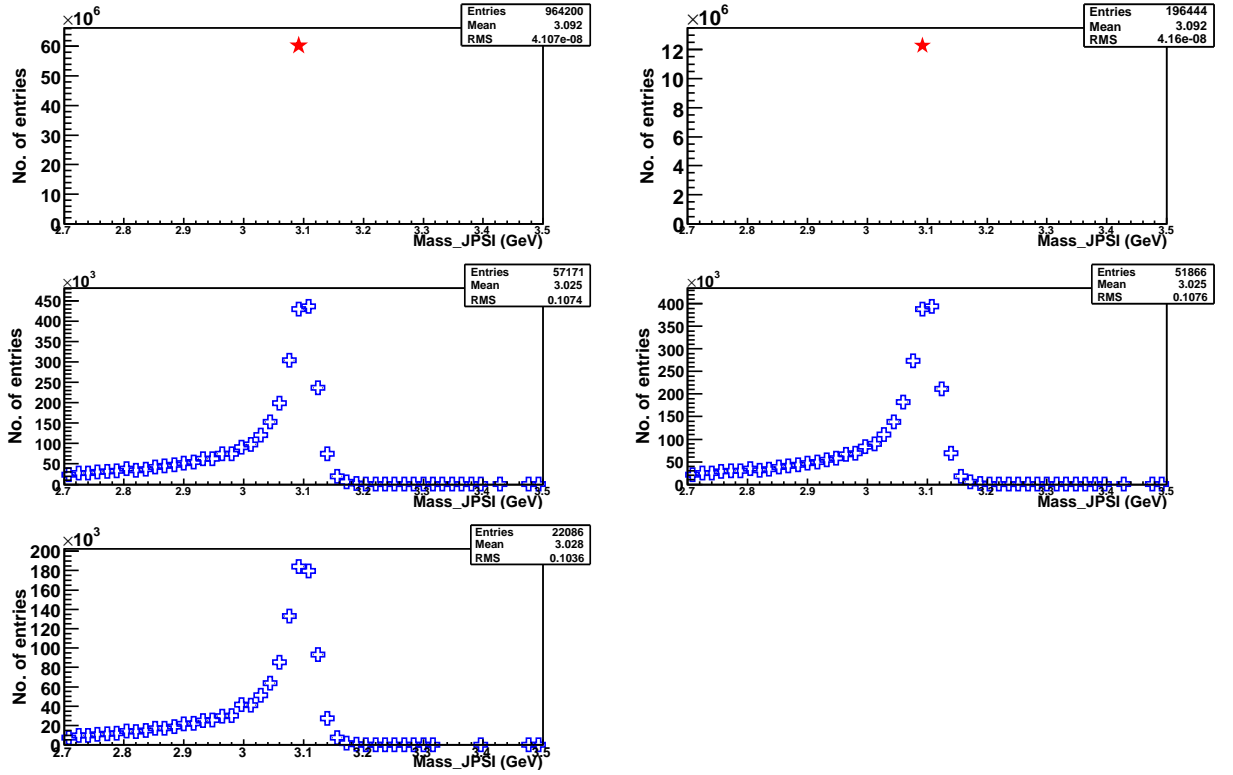


Figure 5.7: Top left: Invariant mass of primary  $J/\psi$  at the generated level; Top right: Invariant mass of  $J/\psi$  at the generated level including the acceptance cuts; Middle left: Invariant mass of  $J/\psi$  at reconstructed level including the vertex and refit cuts; Middle right: Invariant mass of  $J/\psi$  including above cuts, acceptance and ITSCluster cuts; Bottom left: Invariant mass of  $J/\psi$  including above and selection Cuts. Mass is measured in GeV (natural units for  $c=1$ )

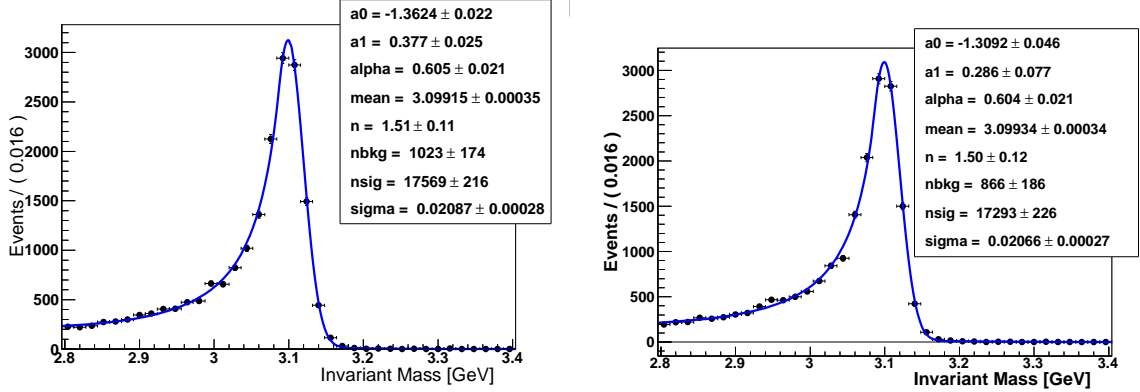


Figure 5.8: Left: Invariant mass distribution of primary  $J/\psi$  after step 5 when fitted with Crystal-Ball function for sample 1; Right: Invariant mass distribution of primary  $J/\psi$  after step 5 when fitted with Crystal-Ball for sample 2. Mass is measured in GeV (natural units for  $c=1$ ). The bin size has been automatically chosen by root.

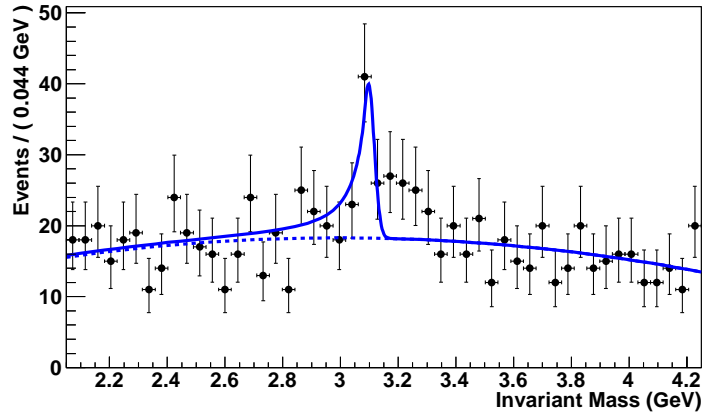


Figure 5.9:  $J/\psi$  invariant mass distribution for real data, for 78 million events passing all the selection cuts mentioned in section (5.2.1), when fitted with Crystal-Ball function.

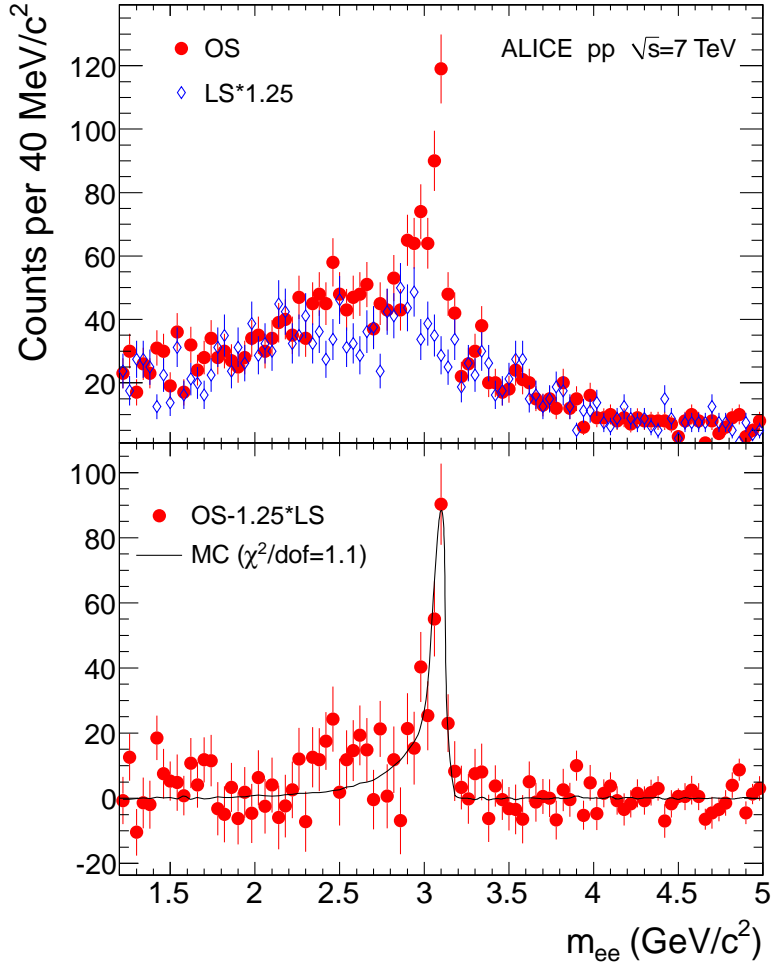


Figure 5.10:  $J/\psi$  invariant mass distribution for real data as cited in [105]. Top: invariant mass distribution for like-sign (LS) and opposite-sign (OS) electron pairs. Bottom: the difference of the two distributions with the fit to the Monte-Carlo (MC) signal superimposed. The luminosity used for this analysis is  $L = 3.9 \text{ nb}^{-1}$ . In the bottom plot a correction factor for like sign 1.25 has been applied to correct for residual background with the opposite sign sample in the side bands.

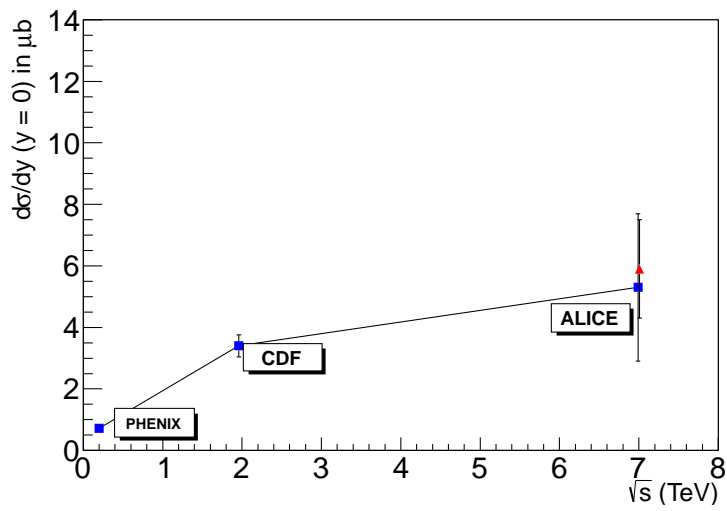


Figure 5.11:  $J/\psi$  production cross-section as a function of collision energy for various experiments. ALICE points show only the statistical error. The red one corresponds to results published in [105]. The blue one is the result of analysis presented in this thesis given by formula 5.18. The systematic error corresponding to these two points is 1.7 and 1.8 respectively.

## Chapter 6

# Determination of the fraction of $J/\psi$ from B hadron decays

B mesons decay into  $J/\psi$  mesons with a branching ratio of about 1%. Since B mesons are produced by a factor of 5 [79] more abundantly than the direct  $J/\psi$  mesons, and since direct  $J/\psi$  production in ion-ion collisions might be further suppressed by QGP effects, secondary  $J/\psi$  mesons contribute to a large fraction of the observable  $J/\psi$  signal. The fraction of  $J/\psi$  originating from B rises from about 10% at Tevatron [110] to about 35% at LHC 7 TeV energy [104].

The interest for developing a procedure to measure the production of secondary  $J/\psi$  is two-fold. Firstly they provide a sensitive measurement of the B meson production cross-section. Secondly, the identification and reconstruction of the secondary  $J/\psi$  meson is essential to investigate medium effects on primary charmonia. The  $p_t$

distribution of the  $J/\psi$  is particularly interesting since  $J/\psi$  from B meson decays exhibit a much harder transverse momentum spectrum than the primary ones and at large transverse momentum the ratio of the secondary to primary  $J/\psi$  may grow as large as 1:1.

The lifetime for the B meson is about  $1.530 \times 10^{-12}$  seconds [113]. The  $J/\psi$  lifetime is very small ( $7.2 \times 10^{-21}$  seconds), so when a  $J/\psi$  comes from a B decay its vertex is likely to be displaced with respect to the primary vertex. The distance  $L$  the  $J/\psi$  meson appears to travel in the detector is:

$$\vec{L} = \frac{\vec{p}}{M_B} \tau \quad (6.1)$$

where  $p$  is the magnitude of the B meson momentum.  $M_B$  and  $\tau$  are the mass and mean lifetime of B meson respectively. The length  $L$  can be measured as the distance between the primary event vertex and the secondary vertex corresponding to the  $J/\psi$  decay. The vertex resolution in the direction parallel to the beam (axis  $z$  in ALICE coordinate system) is of the order of millimetres and so any information about the  $z$  component of the distance  $L$  is smeared out. In order to separate  $J/\psi$  originating from B hadrons from those directly produced, it is useful to introduce the component of  $L$  perpendicular to the beam. The variable  $L_{xy}$  is defined as the projection of the  $J/\psi$  flight distance on its transverse momentum:

$$L_{xy} = \vec{L} \cdot \frac{\vec{p}_t(J/\psi)}{|\vec{p}_t(J/\psi)|} \quad (6.2)$$

as is shown in figure 6.1.  $\vec{p}_t(J/\psi)$  is the  $J/\psi$  transverse momentum vector and  $\vec{L}$  is the vector from the primary vertex where B hadrons are produced to the  $J/\psi$

decay vertex.

This method works well for a  $J/\psi$  with high  $p_t$  where the flight direction is aligned with that of the B-hadrons, while for low  $p_t$ , the contribution of a  $J/\psi$  with a large opening angle between its flight direction and that of the B-hadron will affect the separation ability.

The quantity  $L_{xy}$  depends on the B meson momentum. In order to reduce this dependence the so called proper decay length variable is defined as:

$$x = L_{xy} \cdot \frac{M_{J/\psi}}{|\vec{p}_t(J/\psi)|} \quad (6.3)$$

where the  $M_{J/\psi}$  is the mass of the  $J/\psi$  candidate. This works best if the  $J/\psi$  takes most of the momentum of the decaying B meson. In order to calculate the percentage of  $J/\psi$  that comes from the B hadrons, a method based on a simultaneous fit of the invariant mass and proper decay length distributions has been developed, using a maximum likelihood fitting technique. Our method is a modification of the method used by the CDF [110], CMS [104] and ATLAS [111] collaborations. A simultaneous invariant mass and proper length fit is performed using a log-likelihood function  $L$  given by equation:

$$\ln L = \sum_{i=1}^N \ln F(x, M_{e^+e^-}) \quad (6.4)$$

where  $N$  is the total number of events and  $F$  is the probability density function.

The invariant mass and proper decay length distribution is given by the equation:

$$F(x, M_{e^+e^-}) = f_{Sig} \times F_{Sig}(x, M_{ee}) + (1 - f_{Sig}) \times F_{Bkg}(x, M_{ee}) \quad (6.5)$$

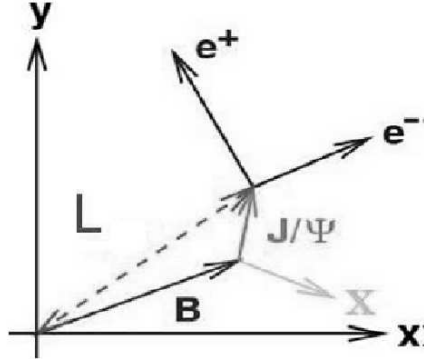


Figure 6.1: Definition of the vector  $L$  from the primary vertex where  $B$  hadrons are produced to the  $J/\psi$  decay vertex.

where  $f_{sig}$  is the fraction of signal  $J/\psi$  events (primary and secondary),  $F_{sig}(x, M_{ee})$  and  $F_{bkg}(x, M_{ee})$  are two dimensional functions describing simultaneously proper-decay length and invariant mass distributions of the signal and background events respectively. The signal function convolutes physics distributions of primary and secondary  $J/\psi$  with detector responses using MC simulation. The background function is extracted from like-sign pairs including the detector response. Despite the short coming of like-sign events described in the previous chapter, it is suitable to use like-sign for this purpose.

## 6.1 Signal and Background Functions

The function for the  $J/\psi$  proper decay length and invariant mass signal distributions consist of two terms, prompt  $J/\psi$  decay and the  $B \rightarrow J/\psi + X$  decay functions

labelled  $F_P(x, M_{ee})$  and  $F_B(x, M_{ee})$  respectively:

$$F_{Sig}(x, M_{ee}) = f_P \times F_P(x, M_{ee}) + (1 - f_P) \times F_B(x, M_{ee}) \quad (6.6)$$

where  $f_P$  is the fraction of  $J/\psi$  mesons originating from prompt  $J/\psi$  decays. Substituting the value of  $F_{Sig}(x, M_{ee})$  in equation (6.5) we get:

$$F(x, M_{e^+e^-}) = f_{Sig} \times f_P \times F_P(x, M_{ee}) + f_{Sig} \times (1 - f_P) \times F_B(x, M_{ee}) + (1 - f_{Sig}) \times F_{Bkg}(x, M_{ee}) \quad (6.7)$$

The projections of the 2-dimensional invariant mass and proper length distributions for the primary (prompt)  $J/\psi$  sample is shown in figure 6.2. For the prompt  $J/\psi$  the true proper decay length  $x$  is zero and the distribution seen in figure 6.2 reflects the resolution of the ALICE detector. The green curve represents the probability density function  $F_P(x, M_{ee})$  obtained from 2 dimensional histogram by a linear interpolation leading to piece-wise linear function.

The projections of the 2-dimensional invariant mass and proper length distributions for the secondary  $J/\psi$  ( $B \rightarrow J/\psi X$ ) sample are shown in figure 6.3. The expected exponential decay of B hadrons in the proper decay length region  $x > 0$  is evident. The red curve represents the probability density function  $F_B(x, M_{ee})$  obtained from a 2 dimensional histogram by a linear interpolation.

The projections of 2-dimensional invariant mass and proper decay length distributions for real data like-sign candidates ( same cuts as opposite sign candidates) is shown in figure 6.4. There is no mass peak observed as expected.

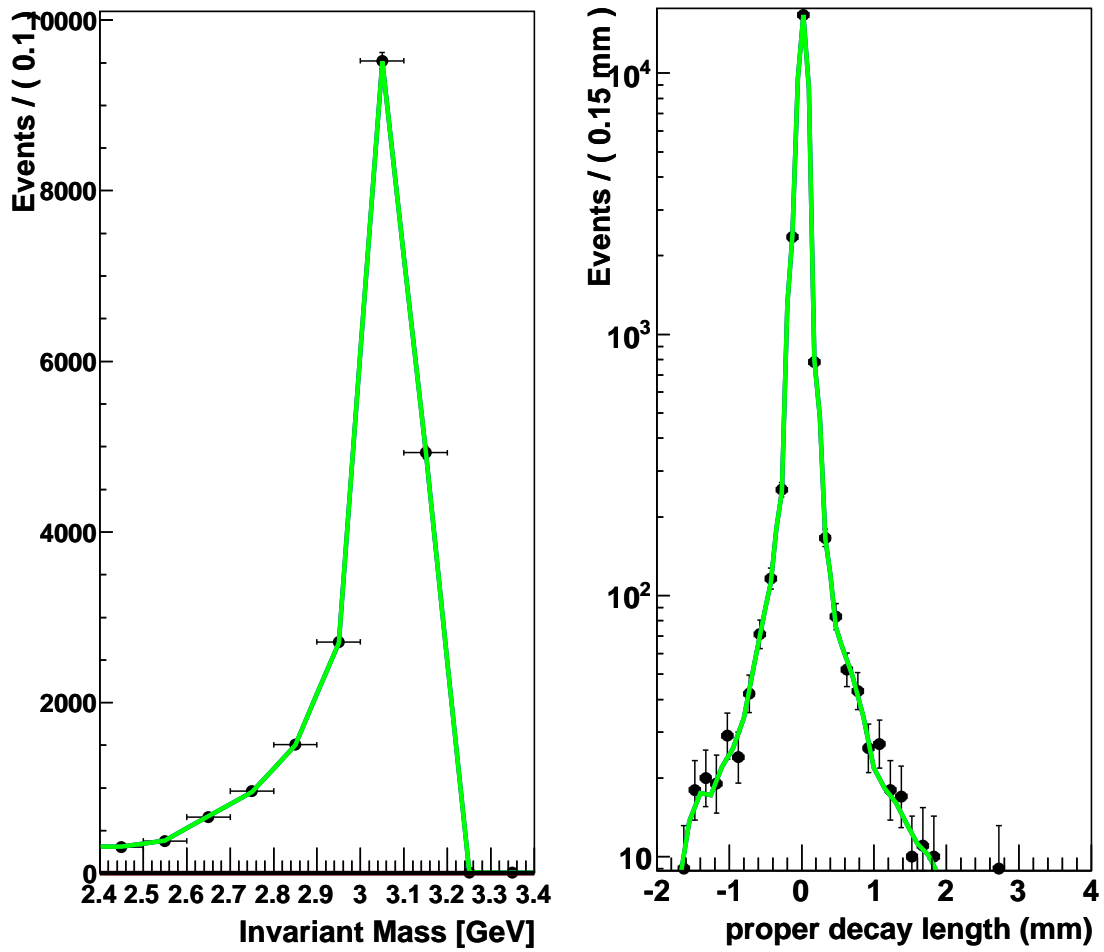


Figure 6.2: Primary  $J/\psi$  Monte-Carlo sample: Left side: The invariant mass  $M_{ee}$  distribution ( measured in GeV in natural units with  $c=1$ ); Right side: proper decay length  $x$  distribution. The curves correspond to linear interpolation and give the function  $F_P$ .

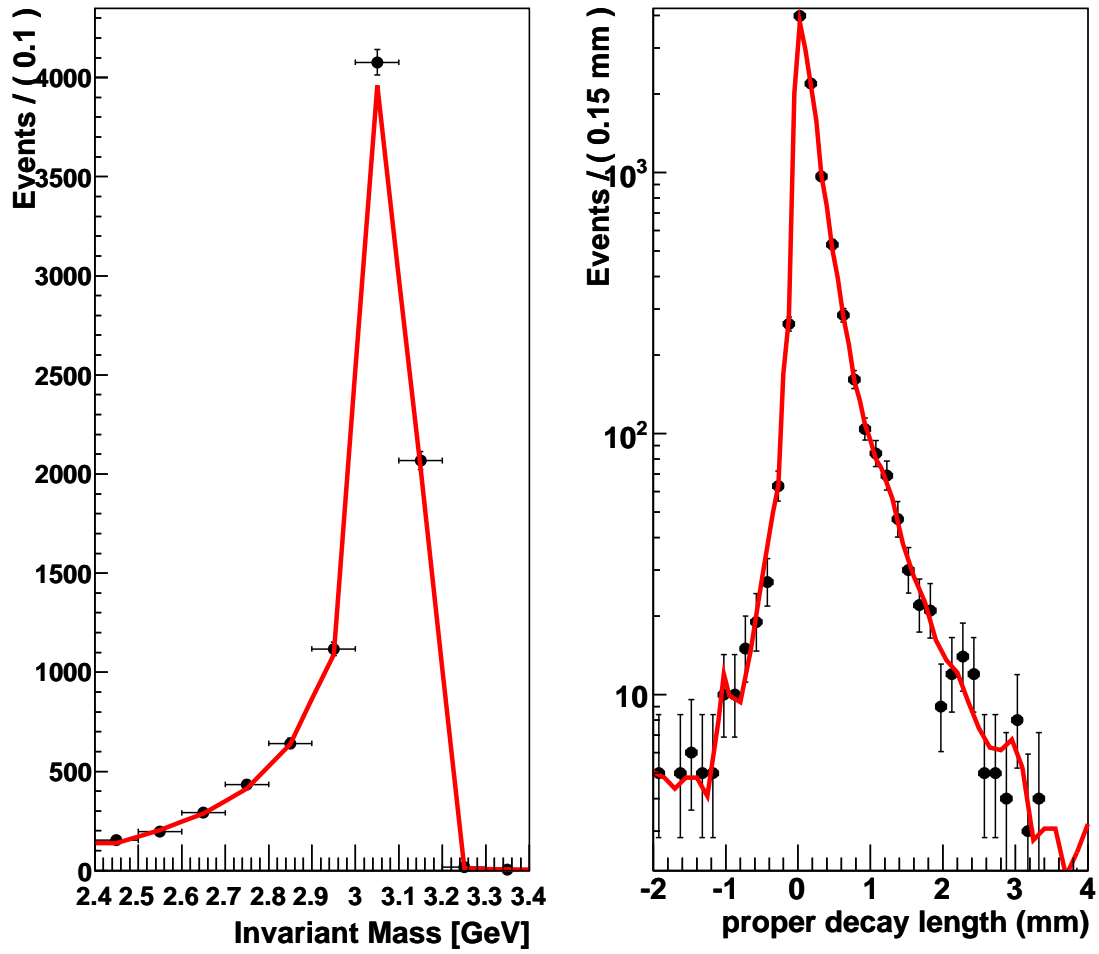


Figure 6.3: Secondary  $J/\psi$  Monte-Carlo sample: Left side: The invariant mass  $M_{ee}$  distribution ( measured in GeV in natural units with  $c=1$ ); Right side: proper decay length  $x$  distribution. The curves correspond to linear interpolation and give the function  $F_B$ .

The black curve represents the probability density function  $F_{Bkg}(x, M_{ee})$  obtained from 2 dimensional histogram by linear interpolation. These parameterisations already take into account the physical distributions and detector resolutions.

## 6.2 Implementation and validation

The procedure as described in the previous section is implemented using the fitting package in the ROOT framework known as RooFit [114]. The Monte-Carlo samples of primary and secondary  $J/\psi$ s described in chapter 4 are used to obtain a parametrisation of primary and secondary probability density functions, while for background it is taken from real data like-sign (see figures 6.4, 6.2 and 6.3).

In order to validate the procedure a mixture of primary, secondary and background samples is created with  $f_P^{TRUE} = 0.70$  and  $f_{sig}^{TRUE} = 0.50$  and fractions  $f_{sig}$  and  $f_P$  are extracted. In this section the mixtures are called **fake data**. The results are shown in table 6.1. The different lines in the table correspond to different PDFs used in the fit. The results in the first line are obtained using PDFs identical to **fake data** histogram (i.e. piecewise constant histogram). The results are indeed exactly equal to the fractions chosen as input in **fake data**. There are no errors because of 100% correlation as the data samples are the same. This control calculation excludes trivial errors in the procedure. The results in the second line are obtained using PDFs extracted from the **fake data** histogram by linear interpolation (i.e. piecewise linear function). In this case the fractions differ by 7 - 8% from the input values. The samples are again 100% correlated and the deviation can be

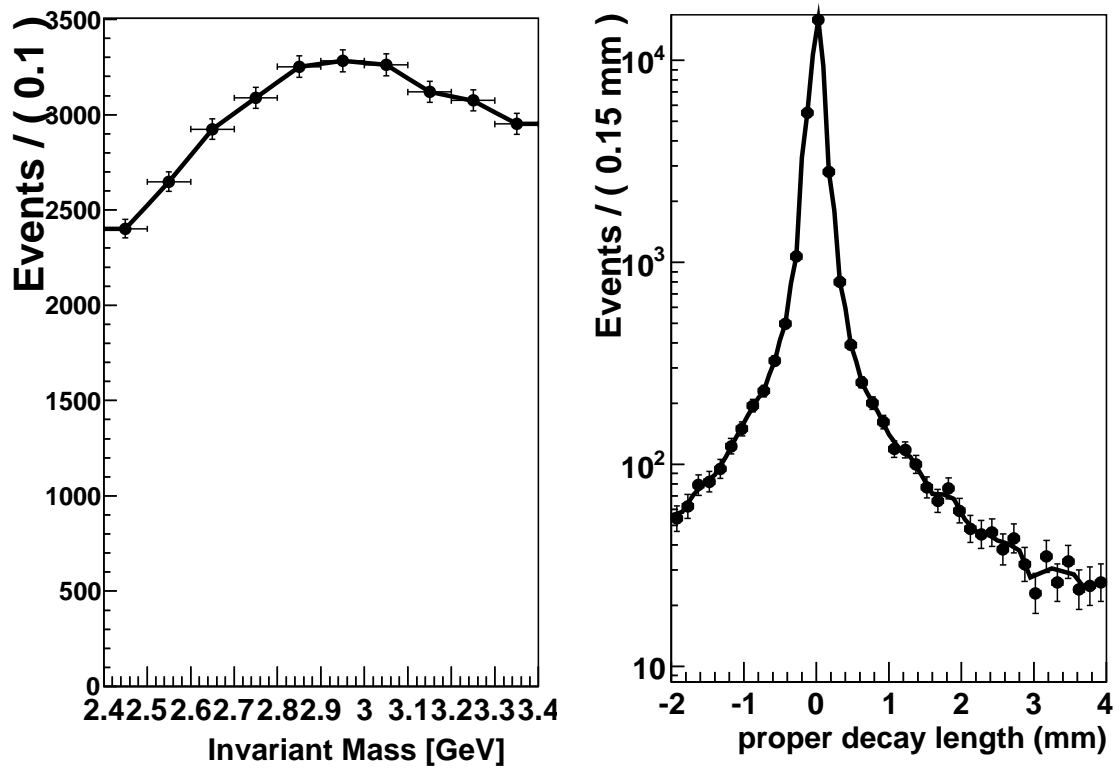


Figure 6.4: Data like-sign: Left side: The invariant mass  $M_{ee}$  distribution (measured in GeV in natural units with  $c=1$ ); Right side: proper decay length  $x$  distribution. The curves correspond to linear interpolation and gives the function  $F_{Bkg}$ .

taken as an estimate of the systematic uncertainty of the method due to the finite bin size and the limited statistics used for the PDFs extraction. The results in the last line are obtained using the PDFs extracted from a Monte-Carlo sample which is independent of the **fake data** sample and as such is the closest to the situation we encounter with real data. The projections of invariant mass and proper length together with fitted functions for this case are shown in figure 6.5.

Table 6.1: Validation of fitting procedure

| Samples     | PDFs | Primary fraction $f_P$ | Signal fraction $f_{sig}$ |
|-------------|------|------------------------|---------------------------|
| Identical   | 0    | 0.70                   | 0.50                      |
| Identical   | 1    | 0.82                   | 0.57                      |
| Independent | 1    | $0.811 \pm 0.005$      | $0.571 \pm 0.004$         |

### 6.3 Comparison with data and summary

An attempt has been made to use the method with the real data sample. The projection of invariant mass and proper decay length for data sample with  $PTCUT_T > 1.3$  GeV/c are shown in figure 6.6. The estimated fraction of inclusive  $J/\psi$  in sample is  $0.15 \pm 0.07$ . The fraction of primary  $J/\psi$  with respect to inclusive is  $0.6 \pm 0.3$ . The result is limited by the statistics available and the sensitivity of the method requires further investigation.

In future, with the implementation of the electron TRD trigger [1], the sample size will increase and this method is then expected to work better than in the present scenario. An ALICE measurement of the fractions of primary and secondary  $J/\psi$  in

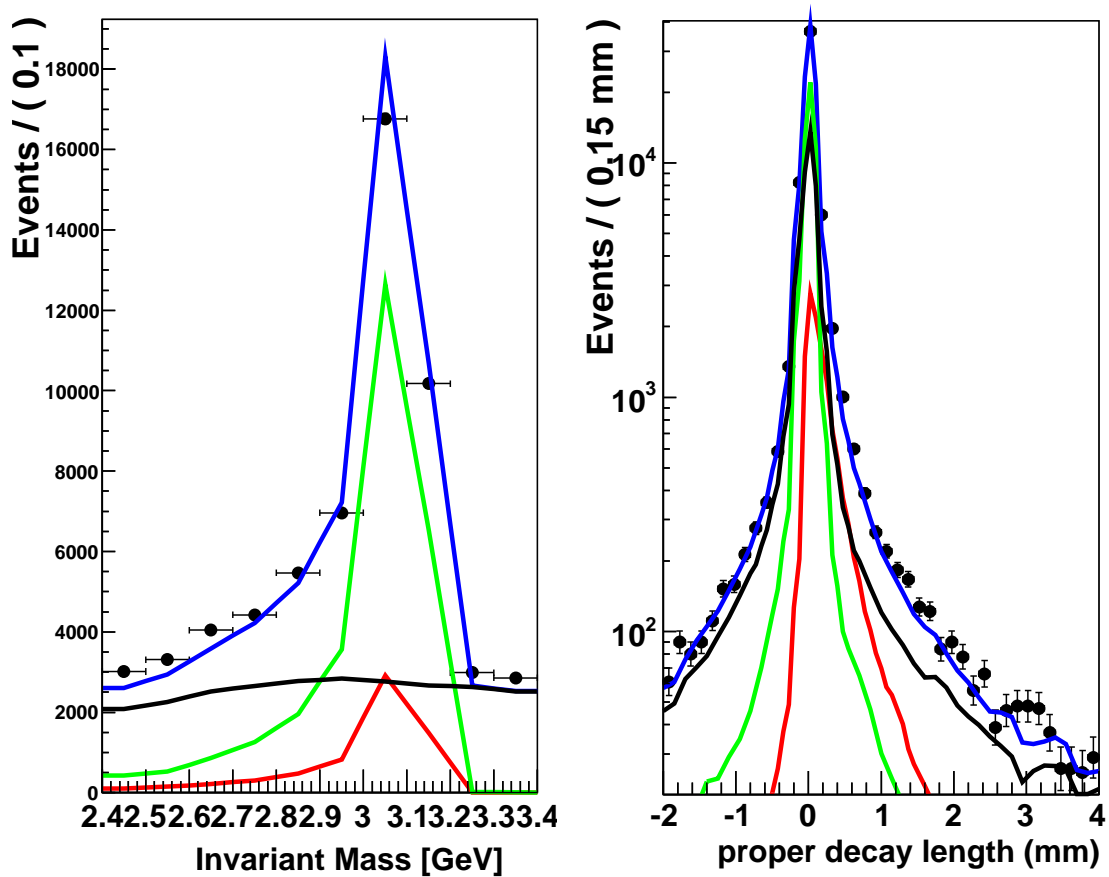


Figure 6.5: The Invariant mass (measured in GeV in natural units  $c=1$ ); and proper decay length distributions from a **fake data** mixture (data points). The green, red, black curves correspond to primary, secondary and background samples. The fit values for  $f_P$  and  $f_{sig}$  correspond to the last line in the table 6.1

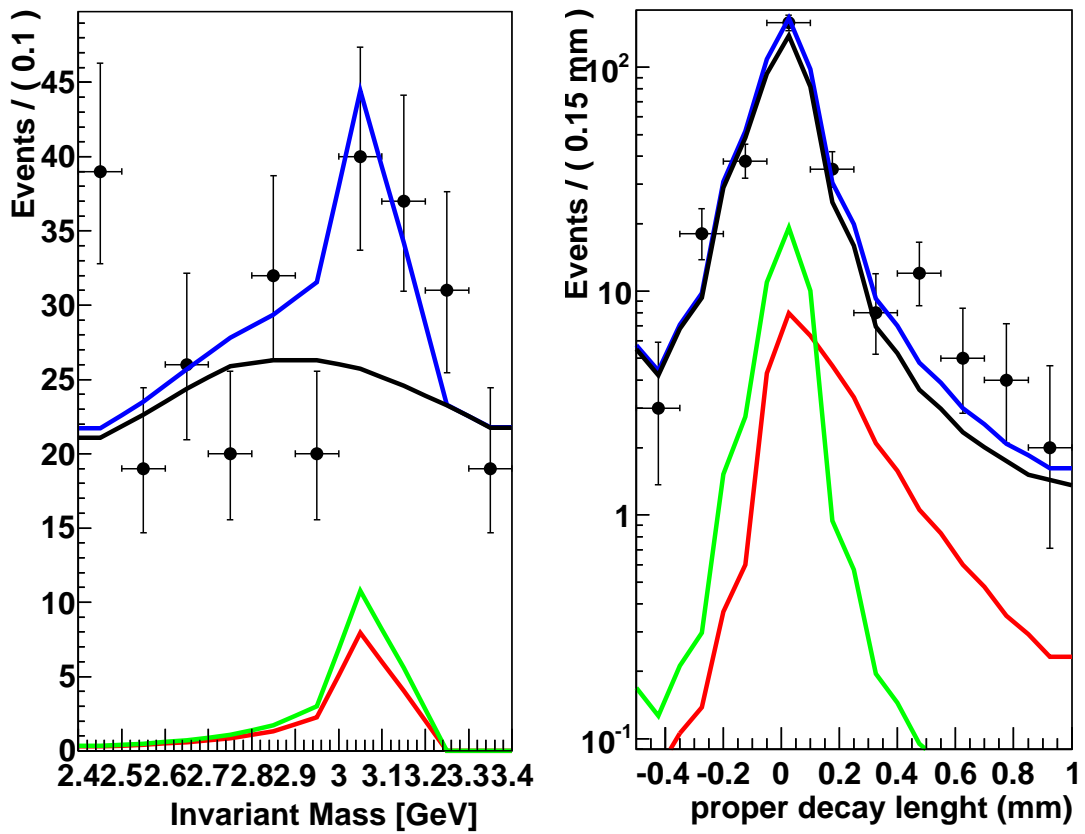


Figure 6.6: The Invariant mass (measured in GeV in natural units  $c=1$ ) and proper decay length distributions for real data (dots with error bars). The green, red, black curves correspond to primary, secondary and background samples.

the dimuon channel is in preparation.

With the increased statistics it will be possible to perform the differential analysis in terms of  $P_t$  bins as done previously by CDF [110]. In addition a complete study of the lepton pair like-sign distribution both in MC and data would be possible. This will imply that a better understanding of the background would be necessary, similar to what has been done by CDF [110], CMS [104] and ATLAS [111].

# Chapter 7

## Summary and outlook

The ALICE experiment at CERN has been designed to study QCD processes with heavy-ion collisions. However it allows studies of proton-proton physics to be performed as well, and the majority of data accumulated so far has been recorded with  $pp$  collisions.

This thesis presents the study of  $J/\psi$  production in  $pp$  collisions at ALICE. In particular, a measurement of  $J/\psi$  cross-section at  $\sqrt{s} = 7$  TeV energy has been performed, together with a study of a possible algorithm to separate primary  $J/\psi$  from those coming from decays of  $B$  hadrons. The  $J/\psi$  particles have been searched exclusively in the decay channel  $J/\psi \rightarrow e^+e^-$  without the TRD trigger, which is designed especially for the identification of the electrons but was not available at the time. The study focused on what would be achievable in a period of early running, with integrated luminosity of  $L = 1.25 \text{ nb}^{-1}$ , at a proton-proton centre of mass

collision energy of  $\sqrt{s} = 7$  TeV.

First, a number of physics and quality cuts have been optimised to improve the signal to background ratio, using Monte-Carlo samples and real data taken during early 2010. The result highlights that the most efficient criterion to reject the background and select a sufficiently pure sample of electrons is a selection on the ITS clusters and TPC energy deposit. Still, the TPC detector was not used at its full capacity during the 2010 runs; therefore the cut studied were optimised with respect to the detector capabilities available at that time.

Second, acceptances and efficiencies have been calculated using an adaptation of the ALICE correction framework for various  $P_t$  of the electrons. Performing a fit to the  $J/\psi$  mass distribution as a function of electron transverse momentum, gives the value  $P_t > 1.3$  GeV/c, as the cut giving the most favourable signal-to-background ratio. In addition, a dedicated procedure has been implemented to evaluate efficiency and correction due to the electron identification algorithm, based on the TPC detector response.

Third, the  $J/\psi$  cross-section has been calculated, taking into account acceptances and efficiencies, and systematic uncertainties have been evaluated. The measurement is dominated by statistical uncertainty. The biggest systematic uncertainty comes from signal extraction. The result presented in this thesis is consistent with the value recently published by the ALICE collaboration. The cross-section presented here is intended as measurement on an early sample of data, with an alternative method which proves to be comparably good with respect to the ALICE published paper [105]. The statistics used here has not been increased due to time

constraints and to the fact that including later periods of data would involve studying different cuts and applying different corrections.

Finally, in a similar manner to that adopted by the CDF and CMS collaborations, to calculate the fractions of primary and secondary  $J/\psi$  (i.e. those coming from  $B$  hadrons) an algorithm has been developed. The validity of this algorithm in ALICE has been demonstrated using Monte-Carlo samples. However, due to low statistics, at the moment such a method is not applicable to real data. In future, with the use of the TRD detector and implementation of a special TRD trigger with increased statistics, this algorithm is foreseen to work for real data and will allow the extraction of primary  $J/\psi$  and the  $J/\psi$  from  $B$  directly from data as well.

# Appendix A

## Maximum Likelihood method

A common problem in particle physics is to estimate parameters from data. In this appendix the common methods of **Least Squares and Maximum Likelihood** are described.

The method of least squares looks for parameters, in such a manner that  $\chi^2$  is minimum. The  $\chi^2$  can be written as:

$$\chi^2(\alpha_1, \alpha_2, \dots, \alpha_s) = \sum_{i=1}^r \left( \frac{(v_i - np_i(\alpha_1, \alpha_2, \dots, \alpha_s))^2}{v_i} \right) \quad (\text{A.1})$$

where each bin have  $v_i$  events with a total number of  $n$  events in the sample and  $r$  is the total number of bins.  $p_i$  is the probability that the individual event falls into the  $i$ -th bin being a function of  $s$  parameters,  $\alpha_j$ , whose value we want to estimate. The values of  $\alpha_j$  for which the  $\chi^2$  is minimum are the best estimators of the true  $\alpha_j$  values.

The  $\chi^2$  method works in case of binned data and also it requires a sufficient sample size in order for the  $\chi^2$  method to be valid.

On the other hand maximum likelihood method is used when the density of events over the physical region is low and when there would not be sufficient events per bin to make alternative methods usable. In this thesis maximum likelihood method is used to determine the values of the parameters from the data.

Suppose we have a probability density function,  $f(\vec{x}; \alpha_1, \alpha_2, \dots, \alpha_s)$ , where  $\vec{x}$  is the vector of the measured variable and  $\alpha_1, \alpha_2, \dots, \alpha_s$  are  $s$  parameters.

$n$  independent measurements are performed, obtaining  $\vec{x}_1, \vec{x}_2, \dots, \vec{x}_n$ . Then

$$L = f(\vec{x}_1)f(\vec{x}_2)\dots f(\vec{x}_n) \tag{A.2}$$

is the density function for obtaining a set of events if  $\vec{\alpha}$  is fixed.  $L$  is called the likelihood of the experimental results.

The maximum likelihood method consist in finding an estimate of the parameter  $\vec{\alpha}^*$ , which maximises  $L$ . As the maximum of  $L$  is also the maximum of  $\log L$ , we tend to use the latter function. The  $\log L$  carries more directly the information of the uncertainty for the estimated parameters  $\vec{\alpha}$ . Thus the set of likelihood equations is:

$$w = \log L = \sum_{i=1}^n \log f(\vec{x}_i; \alpha_1, \alpha_2, \dots, \alpha_s) \quad (\text{A.3})$$

$$\frac{\partial w}{\partial \alpha_j} = \sum_{i=1}^n \frac{1}{f(\vec{x}_i)} \frac{\partial f(\vec{x}_i)}{\partial \alpha_j} = 0 \quad (\text{A.4})$$

To demonstrate how this method works, a simple example of lifetime measurement is presented below. The probability density function is

$$f(t; \tau) = \frac{1}{\tau} e^{-\frac{t}{\tau}} \quad (\text{A.5})$$

where  $t$  is the measured lifetime in a given event and  $\tau$  is the mean life time, i.e. the parameter to be estimated. The Likelihood function is:

$$L = f(t_1; \tau) f(t_2; \tau) \dots f(t_n; \tau) \quad (\text{A.6})$$

and substituting equation (A.5) for  $f$  gives:

$$L = -n \ln \tau - \frac{1}{\tau} \sum_{i=1}^n t_i \quad (\text{A.7})$$

The estimate of the mean lifetime  $\tau$  which maximises the likelihood function  $L$  is, in this case, the arithmetic average on measured lifetimes  $t_i$ :

$$\tau = \frac{\sum_{i=1}^n t_i}{n} \quad (\text{A.8})$$

The ratio of log L functions gives an estimate of how two different models compare with each other. For example, a fit with full parameters can be compared with

a fit with a reduced number of parameters. For a sufficiently large enough number of events, the ratio is distributed as  $\chi^2$  with degrees of freedom equal to the number of fixed parameters. From the  $\chi^2$  distribution and the value of the ratio, a confidence level can be established [115].

# Appendix B

## $J/\psi$ polarisation frame

The angular distribution of  $J/\psi$  decay leptons carries information about the  $J/\psi$  polarisation. The angular distribution integrated over the azimuthal angle is given by [106]:

$$\frac{d\sigma}{d\cos\theta^*} = A(1 + \lambda \cos^2\theta^*) \quad (\text{B.1})$$

where  $A$  is a normalisation factor,  $\theta^*$  is the angle between the momentum vector of one lepton in the polarisation quarkonia rest frame and the longitudinal direction ( $\hat{z}$ ) of a selected polarisation vector (frame). The polarisation parameter  $\lambda$  is related to the magnitude of the polarisation, where  $\lambda = 0$  means no polarisation,  $\lambda = 1$  means maximum transverse polarisation and  $\lambda = -1$  means maximum longitudinal polarisation.

Different definitions of the polarisation axis are used to define the average spin

alignment of quarkonia, depending on the particular choice of reference frame:

**The Helicity frame:** The frame in which  $\hat{z}$  is the direction of quarkonium momentum in the  $J/\psi$  rest frame. Our lab frame is defined so that  $z$  axis is in the same direction. The transformation from lab frame to helicity frame corresponds to the Lorentz boost along the momentum of  $J/\psi$ .

**The Collins-Soper frame :** The frame which defines  $\hat{z}$  as the bisector between the directions of the first colliding proton  $p_1$  and of the opposite of the second colliding proton  $p_2$  in the dilepton rest frame. The vectors  $\vec{p}_1, \vec{p}_2, \vec{p}_{J/\psi}$  lie in the same plane.

All the frames differ only by a rotation around the axis perpendicular to the reaction plane, giving different numerical values for the parameters of the decay leptons full angular distribution. The figure B.1 shows the charmonium polarisation axis defined both in the helicity and Collins-Soper frame, in case when the  $J/\psi$  is relativistic. In chapter 5 both of above frames are used to calculate the systematic uncertainty from the  $J/\psi$  polarisation.

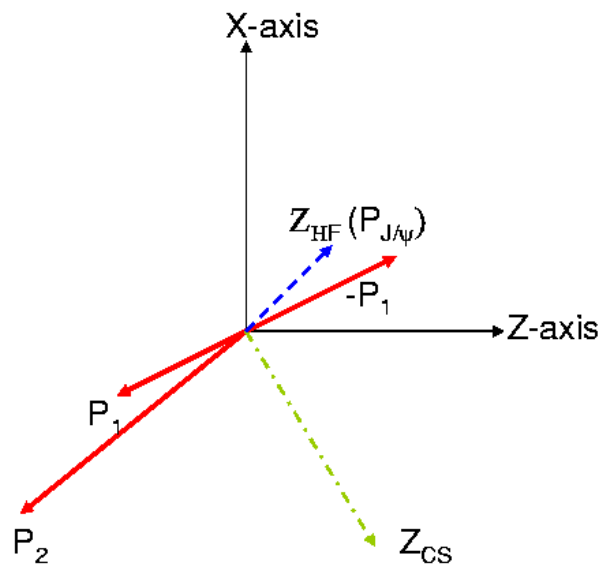


Figure B.1: The charmonium polarisation axes defining both the helicity and Collins-Soper frame.

# Bibliography

- [1] The ALICE experiment at the CERN LHC J. Instr. 3 (2008) S08002  
<http://dx.doi.org/10.1088/1748-0221/3/08/S08002>.
- [2] QCD and Collider Physics by R. Keith Ellis, W. James Stirling and Bryan R. Webber, Cambridge University Press (2003).
- [3] B. I. Abelev et al. [STAR Collaboration], [arXiv:0907.4458v2] ” $J/\psi$  production in Au+Au and Cu+Cu collisions at  $\sqrt{s_{NN}} = 200$  GeV at STAR”.
- [4] H. Satz, Quarkonium binding and dissociation: The spectral analysis of the QGP, Nucl. Phys. A 783, 249 (2007) [arXiv: hep-ph/0609197].
- [5] ALICE: Physics Performance Report, Volume I, ALICE Collaboration et al 2004 J. Phys. G: Nucl. Part. Phys. 30 1517.
- [6] S. Margetis et al., Ann. Rev. Nucl. Part. Sci 50, 299-342 (2000).
- [7] J. Rafelski and B. Muller, Phys. Rev. Lett. 48, 1066 (1982).
- [8] J. Rafelski and J. Letessier, J. Phys. Conf. Ser. 50, 176-191 (2006).

- [9] T. Matsui and H. Satz, *J/psi* Suppression by Quark-Gluon Plasma Formation, Phys. Lett. B 178 (1986) 416.
- [10] R. Vogt, Phys. Rept. 310, 197-260 (1999).
- [11] <http://www.bnl.gov/rhic/>.
- [12] C. Adler et al., Phys. Rev. Lett. 89, 202301 (2002).
- [13] S. S Adler et al., Phys. Rev. C69, 034910 (2004).
- [14] B. B. Back et al., Phys. Rev. B578, 297-303 (2004).
- [15] I. Arsene et al., Phys. Rev. Lett. 91, 072305 (2003).
- [16] D. A. Appel, Phys. Rev. D33, 717 (1986).
- [17] J. J. Aubert et al. [E598 Collaboration], Experimental Observation Of A Heavy Particle, Phys.Rev.Lett.33 (1974) 1406.
- [18] J. E. Augustin et al. [SLAC-SP-017 Collaboration], Discovery Of A Narrow Resonance In  $e^+e^-$  Annihilation, Phys. Rev. Lett. 33 (1974) 1406.
- [19] S. L. Glashow, J. Iliopoulos and L. Maiani, Weak Interactions with Lepton-Hadron Symmetry, Phys. Rev. D 2 (1970) 1285.
- [20] S. W. Herb et al., Observation of a dimuon resonance at 9.5 GeV in 400 GeV proton-nucleus collisions, Phys. Rev. Lett. 39, 252 (1977).
- [21] F.Abe et al. [CDF Collaboration], Identification of top quarks at CDF using kinematic variables, Phys. Rev. D 52, 2605 (1995).

- [22] E. Eichten, K. Gottfried, T. Kinoshita, K. D. Lane and T. M. Yan, Charmonium: The Model, Phys. Rev. D 17, 3090 (1978) [Erratum-ibid. D 21, 313 (1980)].
- [23] E. Eichten, Recent Theoretical Developments For Heavy Quark - Anti-Quark Systems. (Talk), Harvard Univ. Cambridge - HUTP-80-A084 (80,REC.JUN. 81) 14p.
- [24] B. Gong, X. Q. Li, J.-X. Wang, QCD corrections to  $J/\psi$  production via color octet states at Tevatron and LHC arXiv:0805.4751
- [25] J. Baines et al., Heavy quarks(Working Group-3): Summary report, arXiv: hep-ph/0601164.
- [26] R. Vogt, Open and hidden charm production at RHIC and LHC, J. Phys. G 31 (2005) S773 [arXiv: hep-ph/0412303].
- [27] R. Vogt [Hard Probe Collaboration], The A dependence of open charm and bottom production, Int. J. Mod. Phys. E 12 (2003) 211 [arXiv: hep-ph/0111271].
- [28] L. Berger and D. L. Jones, Inelastic Photoproduction Of  $J/\Psi$  And Upsilon By Gluons, Phys. Rev. D 23 (1981) 1521.
- [29] M. Cacciari and M. Kramer, Color-Octet Contributions to  $J/\Psi$  Photoproduction, Phys. Rev. Lett. 76 (1996) 4128 [arXiv: hep-ph/9601276].
- [30] E. Braaten and S. Fleming, Color octet fragmentation and the psi-prime surplus at the Tevatron, Phys. Rev. Lett. 74 (1995) 3327 [arXiv: hep-ph/9411365].

- [31] P. L. Cho and A. K. Leibovich, Color octet quarkonia production, Phys. Rev. D 53 (1996) 150 [arXiv: hep-ph/9505329].
- [32] P. L. Cho and A. K. Leibovich, Color-octet quarkonia production II, Phys. Rev. D 53 (1996) 6203 [arXiv: hep-ph/9511315].
- [33] H. Fritzsche, Producing Heavy Quark Flavors In Hadronic Collisions: A Test Of Quantum Chromodynamics, Phys. Lett. B 67 (1977) 217.
- [34] J. F. Amundson, O. J. P. Eboli, E. M. Gregores and F. Halzen, Colorless States in Perturbative QCD: Charmonium and Rapidity Gaps, Phys. Lett. B 372 (1996) 127 [arXiv: hep-ph/9512248].
- [35] J. F. Amundson, O. J. P. Eboli, E. M. Gregores and F. Halzen, Quantitative tests of color evaporation: Charmonium production, Phys. Lett. B 390 (1997) 323 [arXiv: hep-ph/9605295].
- [36] Heavy Quarkonia Production in p+p Collision from the PHENIX Experiment, Abigail Bickley, University of Colorado, November 18, 2006.
- [37] A. Sansoni et al. (CDF Collaboration), FERMILAB-CONF-95/263-E, to appear in the Proceedings of the sixth International Symposium on Heavy Flavour Physics.
- [38] A. A. Affolder et al. [CDF Collaboration], Measurement of  $J/\psi$  and  $\psi(2S)$  polarisation in  $p\bar{p}$  collisions at  $\sqrt{s} = 1.8$  TeV, Phys. Rev. Lett. 85 (2000) 2886 [arXiv:hep-ex/0004027].
- [39] B. Gong, X. Q. Li, J.-X. Wang, QCD correction of  $J\psi$  production via color octet states at Tevatron and LHC arXiv:0805.4751.

- [40] B. Alessandro et al. [ALICE Collaboration], ALICE: Physics performance report, volume II, J. Phys. G 32 (2006) 1295.
- [41] D. Kharzeev, C. Lourenco, M. Nardi and H. Satz, A quantitative analysis of charmonium suppression in nuclear collisions, Z. Phys. C 74 (1997) 307 [arXiv:hep-ph/9612217].
- [42] C. Baglin et al. [NA38 Collaboration], The production of  $J/\psi$  in 200 GeV/NUCLEON Oxygen, Uranium Interactions. Phys. Lett. B 220 (1989) 471.
- [43] M.C. Abreu et al. (NA50 Collaboration), Phys. Lett. B 410 (1997) 327.
- [44] A. Baldit et al., Study of prompt dimuon and charm production with proton and heavy ion beams at the CERN SPS, CERN-SPSC-P-316.
- [45] A. Adare, et al.,  $J/\psi$  production vs centrality, transverse momentum, and rapidity in Au+Au collision at  $\sqrt{s_{NN}}=200$  GeV, Phys. Rev. Lett. 98 (2007) 232301.
- [46] Anderson L. et al., Nucl. Inst. Meth. 223 (1984) 26.
- [47] C. Castanier, Ph.D Thesis, Universite Blaise Pascal, Aubiere, France, 2003.
- [48] A new measurement of  $J/\psi$  suppression in Pb-Pb collisions at 158 GeV per nucleon. arXiv:hep-ex/0412036v1.
- [49]  $J/\psi$  and  $\psi'$  suppression by comovers in Pb+Pb collisions. arXiv:nucl-th/9609064v1.
- [50] C. Gerschel and J. Huefner, Phys. Lett. B207 (1988) 194.
- [51] Nuclear Physics A 830 (2009) 239c-242c  $J/\psi$  production in p-A collisions at 158 and 400 GeV: recent results from the NA60 experiment.

- [52] S. J. Brodsky, A.S. Goldhaber, B. Z. Kopeliovich, and I. Schmidt., Nuclear Physics B 807 (2009) 334.
- [53] T . Gunji [PHENIX Collaboration], J. Phys, G 34 (2007) S749 [arXiv:nucl-ex/0703004v1]. "Centrality Dependence of  $J/\psi$  Production in Au+Au and Cu+Cu Collisions by the PHENIX Experiment at RHIC".
- [54] L. Susskind, Lattice Models Of Quark Confinement At High Temperature, Phys. Rev. D 20 (1979) 2610.
- [55] J. Kuti, J. Polonyi and K. Szlachanyi, Monte Carlo Study Of SU(2) Gauge Theory At Finite Temperature, Phys. Lett. B 98 (1981) 199.
- [56] J. Engels, F. Karsch, H. Satz and I. Montvay, High Temperature SU(2) Gluon Matter On The Lattice, Phys. Lett. B 101 (1981) 89.
- [57] F. R. Brown et al., On the existence of a phase transition for QCD with three light quarks, Phys. Rev. Lett. 65 (1990) 2491.
- [58] F. Karsch, The Phase transition to the quark gluon plasma: Recent results from lattice calculations, Nucl. Phys. A 590 (1995) 367C [arXiv:hep-lat/9503010].
- [59] F. Karsch, D. Kharzeev and H. Satz, Sequential charmonium dissociation, Phys. Lett. B 637 (2006) 75 [arXiv:hep-ph/0512239].
- [60] R. Rapp, Quark coalescence and charm(onium) in QGP, Eur. Phys. J. C 43 (2005) 91 [arXiv:hep-ph/0502208].
- [61] L. Yan, P. Zhuang and N. Xu, Competition between  $J/\psi$  suppression and regeneration in quark-gluon plasma, Phys. Rev. Lett. 97 (2006) 232301 [arXiv:nucl-th/0608010].

- [62] R. L. Thews and M. L. Mangano, Momentum spectra of charmonium produced in a quark-gluon plasma, *Phys. Rev. C* 73 (2006) 014904 [arXiv:nucl-th/0505055].
- [63] A. Andronic, P. Braun-Munzinger, K. Redlich and J. Stachel, Statistical hadronization of heavy quarks in ultra-relativistic nucleus nucleus collisions, *Nucl. Phys. A* 789 (2007) 334 [arXiv:nucl-th/0611023].
- [64] W. Cassing, E. L. Bratkovskaya and S. Juchem, Excitation functions of hadronic observables from SIS to RHIC energies, *Nucl. Phys. A* 674 (2000) 249 [arXiv:nucl-th/0001024].
- [65] A. Andronic, P. Braun-Munzinger, K. Redlich and J. Stachel, Statistical hadronization of charm in heavy-ion collisions at SPS, RHIC and LHC, *Phys. Lett. B* 571 (2003) 36 [arXiv:nucl-th/0303036].
- [66] L. Evans, P. Bryant, LHC Machine, (2008). JINST 3 S08001
- [67] ALICE Collaboration, ALICE Physics Performance Report, Volume 1. *J. Phys. G: Nucl. Part. Phys.* 30 (2004) 1517-1763.
- [68] ATLAS Collaboration, The ATLAS Experiment at the CERN LHC, (2008). JINST 3 S08003.
- [69] CMS Collaboration, The CMS Experiment at the CERN LHC, (2008). JINST 3 S08004.
- [70] LHCb Collaboration, The LHCb Detector at the LHC, (2008). Jinst 3 S08005.
- [71] S. Karlheinz, Project to prepare the PS Complex to be a Pre-injector for the LHC, (1998). Available: <http://ps-div.web.cern.ch/ps-div/LHC-PS/LHC-PS.html>.

- [72] V. Angelov [ALICE TRD Collaboration], Design and performance of the ALICE TRD front-end electronics, Nucl. Instrum. Meth. A 563 (2006) 317.
- [73] V. Ginzburg, I. Frank, "Radiation of a uniformly moving electron due to its transition from one medium into another", Journ. Phys. USSR, v.9, 353, (1945).
- [74] P. Goldsmith, J. V. Jelley, Phil. Mag. 4, 836, 1959.
- [75] V. L. Ginzburg and V. N. Tsytovich, On The Derivation Of The Transition Radiation Intensity, Phys. Lett. A 79 (1980) 16.
- [76] V. L. Ginzburg and V. N. Tsytovich, Several Problems Of The Theory Of Transition Radiation And Transition Scattering," Phys. Rept. 49 (1979) 1.
- [77] B. Dolgoshein, Transition radiation detectors, Nucl. Instrum. Meth. A 326 (1993) 434.
- [78] ALICE collaboration, ALICE transition-radiation detector: Technical Design Report, CERN-LHCC-2000-012, <http://cdsweb.cern.ch/record/430132>; ALICE Time-of Flight system (TOF): addendum to the technical design report, CERN-LHCC-2002-016, <http://cdsweb.cern.ch/records/545834>.
- [79] B. Alessandro et al., ALICE: physics performance report, volume II, J. Phys. G 32 (2006) 1295.
- [80] ALICE CTP website: <http://www.ep.ph.bham.ac.uk/user/pedja/alice/>.
- [81] <http://root.cern.ch/drupal>.
- [82] <http://aliceinfo.cern.ch/Offline/AliRoot/Manual.html>.
- [83] S Bagnasco et al 2008 J. Phys.: Conf. Ser. 119 062012.

- [84] <http://www.thep.lu.se/torbjorn/Pythia.html>.
- [85] A. Capella, A. Kaidalov, and J. Tran Thanh Van, *Heavy Ion Phys.* 9 (1999) 169.
- [86] M. Gyulassy and X. N. Wang, *Comput. Phys. Commun.* 83 (1994) 307 [arXiv:nucl-th/9502021].
- [87] A. Capella, U. Sukhatme, C-I Tan and J. Tran Thanh Van: Dual Parton Model. *Phys. Rept.* 236 (1994) 225.
- [88] H. J. Moring, J. Ranft, *Phys. Rev. D* 47, 41424145 (1993) String fusion in the dual parton model and the production of antihyperons in heavy-ion collisions.
- [89] R. Brun et al., GEANT 3, CERN report DD/EE/84-1 (1989); Geant4 Collaboration, S. Agostinelli et al., *NIM A*506 (2003) 25.
- [90] A. Ferrari, P. R. Sala, A. Fasso and J. Ranft, FLUKA: A multi-particle transport code (Program version 2005).
- [91] S. Agostinelli et al. [GEANT4 Collaboration], GEANT4: A simulation toolkit, *Nucl. Instrum. Meth. A* 506 (2003) 250.
- [92] <http://www.physi.uni-heidelberg.de/~minjung/alicegirl/alice.../primer.pdf>.
- [93] ALICE Collaboration, ALICE technical design report of the computing”, CERN-LHCC-2005-018 <http://aliceinfo.cern.ch/Collaboration/Documents/TDR/Computing.html>.
- [94] <http://arxiv.org/abs/0810.2241>.
- [95] W. R. Leo, *Techniques for Nuclear and Particle Physics Experiments*”, Springer-Verlag, 1994.

- [96] ALICE Collaboration, Physics Performance Report Vol. 2, 2006.
- [97] ALICE collaboration, ALICE forward detectors: FMD, T0 and V0: Technical Design Report, CERN-LHCC-2004-025, <http://cdsweb.cern.ch/record/781854>.
- [98] <http://pdg.lbl.gov/>.
- [99] H. Bichsel, Nucl. Instrum. Math. A562, 154 (2006).
- [100] J. D. Jackson, "Classical Electrodynamics", John Wiley Sons, Inc., 1999.
- [101] M. Aguilar-Benitez et al., Z. Phys. C 50, 405 (1991).
- [102] T. Skwarnicki, "A Study of the Radiative Cascade Transition Between the Upsilon-Prime and Upsilon Resonance," DESY F31-86-02 (1986).
- [103] <http://aliceinfor.cern.ch/static/aliroot-new/html/roothtml/ClassIndex.html>.
- [104] The CMS collaboration: CERN-PH-EP/2010-046, submitted to the EPJC.
- [105] ALICE collaboration, <http://arxiv.org/abs/1105.0380v1> [hep-ex] 2 May 2011. "Rapidity and transverse momentum dependence of inclusive  $J/\psi$  production in  $pp$  collisions at  $\sqrt{s} = 7$  TeV".
- [106] PHENIX collaboration, Phys. Rev. D 82, 012001 (2010) Transverse momentum dependence of  $J/\psi$  polarisation in p + p collisions at  $\sqrt{s} = 200$  GeV.
- [107] K. Oyama et al. (ALICE Collaboration), proc. of the Workshop "LHC Lumi Days", to be published.
- [108] S. van der Meer, ISR-PO/68-31, KEK 68-64.

- [109] PHENIX collaboration, "  $J/\psi$  production versus Transverse Momentum and Rapidity in p-p collisions at  $\sqrt{s}=200$  GeV, Phys. Rev. Letter 98, 232002 (2007).
- [110] CDF collaboration, arXiv:hep-ex/0412071v1 27 Dec 2004. "Measurement of the  $J/\psi$  Meson and b-Hadron Production Cross Sections in  $p\bar{p}$  Collisions at  $\sqrt{s} = 1960$  GeV ".
- [111] ATLAS collaboration, arXiv:1104.3038v1 14th April 2011. "Measurement of the differential cross-sections of inclusive, prompt and non-prompt  $J/\psi$  production in proton-proton collisions at  $\sqrt{s} = 7$  TeV"
- [112] Measurement of  $J/\psi$  production in pp collisions at sqrt(s)=7 TeV. By LHCb Collaboration (R. Aaij et al.). CERN-PH-EP-2011-018, Mar 2011. 24pp. Temporary entry Published in Eur.Phys.J.C71:1645,2011. e-Print: arXiv:1103.0423 [hep-ex]
- [113] <http://pdg.lbl.gov/>
- [114] <http://root.cern.ch/drupal/content/roofit>.
- [115] Statistical methods in Experimental physics, W.T.Eadie, D.Drijard, F.E. James, M.Roos, B.Sadoulet, North-Hollonad Publishing Company (1998)